

4-22-93
E-17745

NASA Contractor Report 191121

Deformation Mechanisms of NiAl Cyclicly Deformed Near the Brittle-to-Ductile Transition Temperature

Cheryl L. Cullers and Stephen D. Antolovich
Georgia Institute of Technology
Atlanta, Georgia

April 1993

Prepared for
Lewis Research Center
Under Cooperative Agreement NCC3-295

NASA
National Aeronautics and
Space Administration

TABLE OF CONTENTS

| | |
|--|------|
| LIST OF TABLES | iv |
| LIST OF FIGURES | v |
| ABSTRACT | viii |
| INTRODUCTION | 1 |
| BACKGROUND | 4 |
| Properties of NiAl | 4 |
| Physical Metallurgy | 4 |
| Mechanical Metallurgy | 6 |
| Fatigue Properties | 9 |
| Fatigue of Metals | 9 |
| Fatigue Research of NiAl | 11 |
| MATERIAL AND EXPERIMENTAL PROCEDURES | 15 |
| Material and Metallographic Examination | 15 |
| Tensile Testing | 16 |
| Low Cycle Fatigue Testing | 17 |
| Microscopy | 19 |
| RESULTS AND DISCUSSION | 21 |
| Tensile Testing | 21 |
| Low Cycle Fatigue Testing | 22 |
| Fatigue Response | 23 |
| Fracture Surface Observations | 24 |
| Surface Deformation Observations | 25 |
| Internal Deformation Observations | 27 |
| Analysis of Low Cycle Fatigue Properties | 29 |
| Analysis of Internal Deformation | 32 |
| CONCLUSIONS | 37 |
| SUGGESTIONS FOR FUTURE RESEARCH | 40 |
| REFERENCES | 42 |

| | |
|--|----|
| TABLES | 46 |
| FIGURES | 48 |
| APPENDIX A | 75 |
| TENSILE DISPLACEMENT ADJUSTMENT | 75 |
| APPENDIX B | 77 |
| LOW CYCLE FATIGUE DATA | 77 |
| APPENDIX C | 88 |
| ANALYSIS OF DISLOCATION VEIN ORIENTATION | 88 |

LIST OF TABLES

- Table 3.1 - Composition (atomic percent)
- Table 4.1 - Comparison of properties from both specimen geometries tested in monotonic tension.
- Table 4.2 - Tensile test data used for simplistic predictions of fatigue response.

LIST OF FIGURES

- Figure 2.1 - Phase diagram for nickel and aluminum [5].
- Figure 2.2 - Schematic of B2 crystal structure.
- Figure 3.1 - Recrystallized, equiaxed structure of NiAl in transverse and longitudinal directions. Average linear intercept grain size is 39 μm .
- Figure 3.2 - Specifications for tensile specimen drawn to scale. Diameter of gage is 3 mm.
- Figure 3.3 - Specifications for low cycle fatigue specimen. The units in the drawing are millimeters and the diameter of the gage is 4 mm.
- Figure 3.4 - Schematic of blade extensions which attached to a standard 12.7 mm MTS extensometer.
- Figure 3.5 - Photograph of low cycle fatigue test set-up with high temperature extensometer in place.
- Figure 3.6 - Schematic of induction coil design, not drawn to scale.
- Figure 4.1 - True stress versus true strain for monotonic tensile tests conducted at $\dot{\epsilon} = 10^{-4} \text{ s}^{-1}$. Curves shifted right for clarity. Test at 700 K continued to 18.2%.
- Figure 4.2 - Tensile fracture surfaces at 700 K showing 28% intergranular fracture. Initiation sites were not identified but occurred within the gage section.
- Figure 4.3 - True strain to failure as a function of temperature for tensile specimens from this study and reported by Noebe, et al. at $\dot{\epsilon} = 10^{-4}$.
- Figure 4.4 - Stress amplitude versus cumulative plastic strain for all three temperatures at $\dot{\epsilon} = 10^{-4} \text{ s}^{-1}$ (a) $\Delta\epsilon_p = 0.5\%$ and (b) $\Delta\epsilon_p = 1.0\%$.
- Figure 4.5 - Digitized points from hysteresis loops taken during a test at 700 K, $\Delta\epsilon_p = 0.5\%$.

- Figure 4.6 - Lines represent estimated fatigue lives using the universal slopes equation. Data points are total strain range at time of failure from this study.
- Figure 4.7 - Stress amplitude versus cumulative plastic strain for sample tested at 700 K, $\Delta\epsilon_p = 0.5\%$. Regions I-IV indicate areas of rapid cyclic hardening, a stress plateau, additional hardening, and returning to relative stability.
- Figure 4.8 - (a) Duplicate LCF tests conducted at 600 K, $\Delta\epsilon_p = 0.5\%$. (b) Interrupted tests conducted at 675 K, $\Delta\epsilon_p = 1.0\%$.
- Figure 4.9 - Tensile and compressive stress amplitude versus cumulative plastic strain for $\Delta\epsilon_p = 1.0\%$, $\dot{\epsilon} = 10^{-4} \text{ s}^{-1}$, (a) 600 K and (b) 700 K.
- Figure 4.10 - Fracture surface of sample tested at 700 K, $\Delta\epsilon_p = 1.0\%$ (a) low magnification with inclusion at upper left (b) inclusion.
- Figure 4.11 - Portion of the fracture surfaces at (a) 600 K (b) 675 K and (c) 700 K showing, respectively, 47%, 32%, and 33% intergranular fracture.
- Figure 4.12 - Gage surface of sample tested to failure (region IV) at 700 K, $\Delta\epsilon_p = 0.5\%$ showing (a) extensive slip traces and (b) distinct extrusions and fine slip lines.
- Figure 4.13 - Gage surface of sample tested to failure at 600 K, $\Delta\epsilon_p = 1.0\%$ showing regions of slip traces (a) near the fracture surface and (b) near the radius.
- Figure 4.14 - Specimens deformed at 600 K and $\Delta\epsilon_p = 0.5\%$ (a) interrupted in region I, i.e. while cyclicly hardening, (b) interrupted in the beginning of region II, i.e. at the onset of stability, (c) failed in region III.
- Figure 4.15 - Specimens deformed at 600 K and $\Delta\epsilon_p = 1.0\%$ both failed at the beginning of region II as the result of internal inclusions (a) $N_f = 8$ and (b) $N_f = 10$.
- Figure 4.16 - Specimens deformed $\Delta\epsilon_p = 0.5\%$ and interrupted at the beginning of region II, 700 K. Compare to Figure 14(b).
- Figure 4.17 - Specimen deformed at 700 K and $\Delta\epsilon_p = 1.0\%$ compare to Figure 4.15(a,b) above.
- Figure 4.18 - Specimens deformed $\Delta\epsilon_p = 1.0\%$ (a) 675 K and (b) 700 K. Both failed in region III as the result of inclusions. The intrusions/extrusions were more developed in (a) as the result of the lower test temperature even though specimen (a) failed 100 cycles before specimen (b).

- Figure 4.19 - Cellular dislocation structure beginning to form after one fully reversed cycle at 600 K and $\Delta\epsilon_p = 0.5\%$.
- Figure 4.20 - Well developed cells with thick walls of dislocations after 5 cycles at 600 K and $\Delta\epsilon_p = 0.5\%$ with (a) equiaxed and (b) slightly elongated configurations.
- Figure 4.21 - Cyclic hardening curve of sample tested to failure at 600 K and $\Delta\epsilon_p = 0.5\%$ with micrographs of the dislocation structure after (a) 5 cycles, (b) 15 cycles, and (c) failure at 781 cycles.
- Figure 4.22 - Cyclic hardening curve of sample tested to failure at 700 K and $\Delta\epsilon_p = 1.0\%$ with micrographs of the dislocation structure after (a) 6 cycles, (b) failure at 491 cycles, and (c) failure at 1911 cycles.
- Figure 4.23 - Dislocation structures of samples tested to failure at $\Delta\epsilon_p = 0.5\%$ and (a,b) 600 K, region III and (c,d) 700 K, region IV.
- Figure 4.24 - Log saturation (region II) stress and monotonic ductility versus $1/T$ for tests conducted at $\dot{\epsilon} = 10^{-4} \text{ s}^{-1}$ and $\Delta\epsilon_p = 0.5\%$.
- Figure 4.25 - Regions of well aligned loops probably created by superjogs on moving dislocations.
- Figure 4.26 - Interior of specimen held at 600 K for time equivalent to testing to failure showing no evidence of dislocation loops.

ABSTRACT

The intermetallic compound NiAl is one of many advanced materials which is being scrutinized for possible use in high temperature, structural applications. Stoichiometric NiAl has a high melting temperature, excellent oxidation resistance and good thermal conductivity. Past research has concentrated on improving monotonic properties. The encouraging results obtained on binary and microalloyed NiAl over the past ten years have led to the broadening of NiAl experimental programs. The purpose of this research project was to determine the low cycle fatigue properties and dislocation mechanisms of stoichiometric NiAl at temperatures near the monotonic brittle-to-ductile transition. The fatigue properties were found to change only slightly in the temperature range of 600 to 700 K; a temperature range over which monotonic ductility and fracture strength increase markedly. The shape of the cyclic hardening curves coincided with the changes observed in the dislocation structures. The evolution of dislocation structures did not appear to change with temperature.

CHAPTER 1

INTRODUCTION

One of the ongoing challenges of the aerospace industry is to develop more efficient turbine engines. Greater efficiency in a turbine engine can be achieved by reducing the over-all weight and increasing the combustion and exit gas temperatures. Weight reductions are achieved through using materials with higher specific strength. Larger operating temperatures yield a two fold advantage by increasing the thermodynamical efficiency of the engine and reducing the amount of gas flow which is used for cooling rather than combustion. Materials with not only higher melting temperatures but also higher thermal conductivities allow increased engine operating temperatures and reduce life-limiting hot spots. Continued development of nickel-based superalloys has provided steady increases in engine efficiency and the limits of superalloys have probably not been realized. However, other material systems are under consideration for possible use in high temperature engines. Ceramic, intermetallic, and various composite systems are being explored in an effort to exploit the much higher melting temperatures of these systems.

Intermetallic compounds, including NiAl, have been studied for high-temperature applications since the 1950's [1]. NiAl is considered a potential alternative to conventional superalloys due to its excellent oxidation resistance, low density, and high melting temperature [2,3]. The fact that NiAl is the most

common coating for current superalloy turbine blades is an indication of its superior oxidation resistance [2]. The density of NiAl is one-third lower and its thermal conductivity above room temperature is three to eight times higher than that of typical superalloys [2]. Despite these many advantages, binary NiAl requires more investigation before it is ready for use in engines because it has poor high-temperature strength and low-temperature ductility [2]. On-going research [4] in alloy design has led to improvements in the high-temperature strength of NiAl. Some factors controlling low temperature ductility have been identified in the last few years. Small, but reproducible amounts of ductility can now be achieved at room temperature through careful control of chemical purity and processing. Monotonic ductility and fracture toughness studies are researching the mechanisms of the transition from brittle behavior to ductile behavior. The ability to produce a small amount of ambient temperature ductility encourages the broadening of NiAl research efforts to include other areas such as cyclic behavior.

An understanding of the fatigue deformation of NiAl will be necessary before this material system can be used in practical applications. Crack initiation studies, fatigue crack propagation data, and details of creep and fatigue interactions will all need investigation if NiAl is to develop into a mature engineering material. Low cycle fatigue studies can provide information on the initiation of fatigue cracks and the accumulation of internal damage for relatively large imposed strains. The low cycle fatigue response of NiAl is likely to be poor at temperatures below the monotonic transition temperature where ductility is limited.

Low cycle fatigue properties have been reported on binary NiAl in the past year, yet those studies were limited to two temperature ranges; room temperature

and near 1000 K. Eventually, fatigue property data will be needed for a wide range of temperatures and compositions. The intermediate temperature range near the monotonic brittle-to-ductile transition was chosen for this study to ascertain whether the sharp change occurring in monotonic behavior also occurs under cyclic conditions. The dislocation structures which evolved during fatigue testing were assessed as well as their role in the deformation and damage processes.

CHAPTER 2

BACKGROUND

Properties of NiAl

Physical Metallurgy

Binary, near stoichiometric, NiAl is an ordered intermetallic compound with a B2 crystal structure. This phase, designated β on the Ni/Al phase diagram shown in Figure 2.1 [5], is chemically stable between 45 to 60 atomic percent Ni at moderate temperatures. The B2 crystal structure is equivalent to two interpenetrating simple cubic structures with Ni atoms on one lattice and Al atoms on the other, Figure 2.2. An excellent review of β NiAl has recently been written by Noebe, et al. [6]. Material properties relevant to this study will be presented here.

The B2 structure, with its long range order, persists up to NiAl's melting temperature. Neumann et al. [7] have developed a relation determining the disorder parameter, α , from activities data for intermetallic B2 compounds such as NiAl. The disorder parameter for NiAl was found to be approximately 2×10^{-3} at 1273 K which agrees well with values determined by other authors [8]. The temperature dependence of the disorder parameter was found to vary as given in equation 2.1 for intermetallic compounds [7] (α less than 0.1).

$$T \times \ln(2^{\frac{2}{3}} \times \alpha_T) = \text{constant} \quad (2.1)$$

Besides its high degree of order, some of the properties which stirred interest in NiAl as a high-temperature structural material include its high melting temperature, low density, and high thermal conductivity. The melting temperature for stoichiometric NiAl is 1911 K. The density of stoichiometric NiAl is approximately 5.90 g/cm³ [9], with density increasing for additional Ni content and decreasing with additional Al content. For single crystal, stoichiometric NiAl the thermal conductivity is between 70 and 80 W/m-K [2]. Many of NiAl's properties are very sensitive to chemistry, especially near the equiatomic composition. Early x-ray diffraction studies found that in Ni-rich alloys Ni atoms substituted on the Al sublattice but that vacancies filled the Ni sites in Al-rich alloys [9]. Thus for Al-rich alloys the density is reduced both by the increasing percentage of the lighter of the two elements and increasing volume due to constitutional vacancies.

Operative slip-system predictions, based on the ordering energies of atomic bonds, suggested that $\langle 111 \rangle$ superdislocations would dominate slip in CsCl structures, such as NiAl [10]. However, early transmission electron microscopy (TEM) observations of NiAl [11] suggested the dominance of $\langle 100 \rangle$ dislocations on $\{110\}$ planes. Ball and Smallman [11] used the elastic energies of unit dislocations and dislocation dissociations to explain the predominance of $\langle 100 \rangle$ dislocations. In polycrystalline NiAl and in most single crystal orientations, $\langle 100 \rangle$ $\{110\}$ slip has been identified virtually exclusively. Single crystals oriented in $\langle 100 \rangle$ directions are referred to as "hard" orientations since the resolved shear stress on

dislocations oriented along $\langle 100 \rangle$ directions is zero. At low temperatures (i.e. room temperature and below), slip of $\langle 111 \rangle$ dislocations has been observed [12] in compression of $\langle 100 \rangle$ NiAl crystals. (When the strain rate is sufficiently high kinking is frequently observed and the geometrical reorientation leads to deformation along $\langle 100 \rangle$.) Field, Lahrman, and Darolia [13] have presented evidence that $\langle 110 \rangle$ dislocation gliding on $\{110\}$ planes dominate the deformation of $\langle 100 \rangle$ oriented crystals at intermediate temperatures.

Mechanical Metallurgy

Mechanical property data on NiAl proved to be conflicting and widely misunderstood until fairly recently. The sensitivity of this system to compositional variations, vacancy concentrations, and impurity content was probably the reason for much of the confusion. The following summary of properties for near stoichiometric NiAl was condensed from Noebe et al. [6]. The yield strength decreases continuously with increasing temperature. This decrease is sharp from 77 K to 300 K, very gradual from 300 K to the brittle-to-ductile transition temperature (BDTT), and slightly faster from the BDTT to near its melting temperature. The fracture strength and toughness vary little below the BDTT but increases rapidly above the BDTT. The brittle-to-ductile transformation temperature is frequently defined as the temperature for which 5% plasticity can be achieved. This definition not only corresponds well with the above changes in properties, but for polycrystalline NiAl also corresponds to the elimination of grain boundary cracks within specimens tested in compression [14], a decrease in the percentage of intergranular fracture [15] and the increased mobility of grain boundary dislocations [16].

Single and polycrystalline NiAl deform in a brittle fashion at ambient temperature and have a sharp transition to ductile behavior at intermediate temperatures. The brittle behavior of polycrystalline NiAl was first attributed to its limited number of active slip systems [11]. In 1928, von Mises [17] theoretically determined that five independent slip systems were necessary to accommodate shape change along grain boundaries in polycrystalline face centered cubic (FCC) materials. Groves and Kelly [18] generalized the procedure for determining the number of independent slip systems to other crystal structures including the CsCl structure with which NiAl is identified. Ball and Smallman have shown [11], using the Groves and Kelly technique [18], that glide and cross-glide of $\langle 100 \rangle$ dislocations on $\{110\}$ planes provides only three independent slip systems. Although macroscopic non-elastic behavior can be achieved in NiAl tested at ambient temperature in compression and, to a limited extent in tension, this deformation is accomplished congruently with the opening of grain boundary cracks. Fracture surfaces from tests conducted below the BDTT show significant intergranular cracking. Actual plasticity is not achieved in polycrystalline NiAl until the brittle-to-ductile transition temperature (BDTT) of 500-600 K is reached.

Because it was clear that NiAl had an insufficient number of independent slip systems and no new slip had been identified above the BDTT [16], several studies including [11,14-16,19-21] have suggested that thermally assisted deformation, such as dislocation climb was activated. Groves and Kelly demonstrated that a combination of glide and climb of $\langle 100 \rangle$ dislocations provides five independent deformation mechanisms [22] which could accommodate grain-boundary strain. An *in situ*, TEM annealing study confirmed the activation of diffusive mechanisms on

dislocations near grain boundaries at temperature corresponding to the BDTT of the material studied [16].

This explanation does not, however, present the complete picture since there is also a sharp brittle-to-ductile transition in NiAl single crystals. The BDTT is near 500 K for soft orientation single crystals and around 650 K for $\langle 100 \rangle$ oriented crystals [2]. There has speculation that the problem is one of dislocation generation and this has been recently discussed by Hack, et al. [23].

The changes in mechanisms leading to the sharp transition in ductility have not been clearly isolated. The BDTT in NiAl, like that in most BCC metals, has been shown to be affected by, e.g., grain size, composition, impurity content, vacancy concentration, and deformation rate. Off-stoichiometric compositions and the high cooling rates associated with certain processing technique are major factors in determining the BDTT. Constitutional defects and quenched-in vacancies increase the yield strength and subsequently the BDTT.

Khadkidar, et al, [24] determined that extruded NiAl had a crystallographic texture with a preferred $\langle 111 \rangle$ orientation corresponding to the extrusion direction. Annealing of the extruded NiAl made the preferred $\langle 111 \rangle$ orientation even more pronounced. Other studies have reported the same preferred orientation [16]. The preferred orientation for the $\langle 100 \rangle$ direction was 45° from the extrusion axis [24]. A majority of the mechanical property data for polycrystalline NiAl has been generated for extruded material [6] and little information is known about the effects of this preferred orientation.

In addition to identifying the active slip system in NiAl, some comments have been made about the dislocation structures that result from monotonic deformation.

Cellular arrays of dislocations have been identified in near-stoichiometric polycrystalline NiAl deformed at room temperature and interrupted after 1% strain in compression [16], and 2% in tension [25]. Nagpal and Baker [25] suggest this cell structure is the result of cross-slip which is fairly easy for stoichiometric NiAl and more difficult further from the stoichiometric composition.

Fatigue Properties

Fatigue of Metals

Fatigue is frequently the critical failure mode in structures subjected to thermal or mechanical loading. In general, structures exposed to cyclical loading experience stress-controlled fatigue while parts subjected to thermal loading or the local areas around cracks and notches experience strain-controlled fatigue. The advancement of fracture mechanics has extended the lives of many structures. Structures can be retired when cracks develop and approach a critical size rather than taking parts out of service based solely on number of cycles. That means using a part which contains cracks, but knowing how long the cracks will remain sub-critical and not fail catastrophically. Crack initiation and fatigue crack propagation behavior must be well characterized for a high performance material. Low cycle fatigue studies provide information on the response of the metal to relatively high cyclic strains.

Early fatigue work emphasized empirical relations and estimates for predicting life. Many of these estimates are indeed useful rules-of-thumb and can be used for comparing individual material responses to what is considered as the norm. When the unidirectional strain hardening exponent, n , is greater than 0.15 [26] (or greater

than 0.2 [27]) cyclic hardening is expected. Fatigue life, i.e. cycles to failure, can be estimated using monotonic strain to failure, ϵ_f , to approximate the fatigue ductility coefficient, ϵ_f' , in the Coffin/Manson power law function,

$$\frac{\Delta \epsilon_p}{2} = \epsilon_f' (2N_f)^c \quad (2.2)$$

where N_f is the number of cycles to failure and c is the fatigue ductility exponent. Life estimates can also be made using the Manson universal slopes equation, which is designed to include both ductility limiting low cycle fatigue and the strength limiting high cycle fatigue regimes. The universal slope equation, 2.3, uses empirical constants and exponents which are nearly the same for most metals, the ultimate tensile strength, S_u , and the Young's modulus, E .

$$\Delta \epsilon = 3.5 \frac{S_u}{E} (N)^{-0.12} + \epsilon_f^{0.6} (N)^{-0.6} \quad (2.3)$$

Research delving into the internal deformation mechanisms of fatigue revealed many similarities with monotonic deformation. Slip planes and directions for a given material system are the same in unidirectional and cyclic testing [28]. Authors disagree on the extent to which deformation structures are parallel between the two test modes, but certain similarities have been established for FCC materials [29], both between stage I unidirectional hardening and high cycle fatigue and between stage II hardening and low cycle fatigue. Fatigue damage in single phase FCC materials is often concentrated in regions referred to as persistent slip bands (PSB). Persistent slip bands which intersect the specimen surface can be differentiated from

other slip traces by careful polishing experiments. PSB development coincides with the advent of saturation in the cyclic stress-strain curve and the density of PSB increases with subsequent cycling. The dislocation structures associated with PSB are better understood for materials which deform by wavy slip than for those deforming by planar slip [30]. When PSB occur, dislocation movement is not homogenous but is concentrated in the regions identified as ladder structures. The ladder structures (themselves occasionally referred to as persistent slip bands) consist of regions of dislocations which, when viewed in profile, resemble rungs of a ladder. The strain imposed during the fatigue test is accommodated by dislocation movement between these rungs and the matrix or bulk material experiences comparatively little dislocation activity. (Materials with second phases often show similar fatigue behavior, but will not be discussed in the context of this thesis.) PSB only develop within certain applied stress/strain amplitudes limits [31] and there are complicating issues associated with the initial state of the material [31]. The surface PSB phenomenon has been observed to an extent in fatigue of some BCC materials [32,33], but effects have also been reported that do not occur in FCC fatigue [34,35].

Fatigue Research of NiAl

Studies of NiAl's low cycle fatigue behavior have been recently reported. These reports have concentrated on the lives, cyclic strength and general response to cyclic deformation at room temperature and elevated temperatures near 1000 K. Initial research emphasized obtaining base-line data and comparing the cyclic behavior of NiAl to superalloys and other B2 compounds.

Room temperature and 1033 K fatigue tests were conducted by Bain et al. [36] on $\langle 100 \rangle$ single crystal NiAl-0.1% Mo. Tests were conducted in total strain control. Test scatter was minimal at the elevated temperature, but most initiation sites for room temperature tests were associated with pre-existing porosity in the crystals [37] leading to increased scatter in data. Secondary cracks, which coalesced and caused fast fracture, were observed parallel to the loading axis. The 1033 K cyclic lives compared favorably to the superalloy René N4 at higher total strain ranges due to the larger ductility of NiAl. However at lower total strain ranges, the NiAl crystals had shorter lives since the low yield strength of NiAl led to plastic deformation at strain ranges where René N4 remained elastic.

Room temperature cyclic tests have been conducted by Hartfield-Wünsch [38,39] on the B2 compound $\text{Ni}_{49}\text{Al}_{31}\text{Fe}_{20}$ (which, like NiAl, deforms along $\langle 100 \rangle$ slip directions) at plastic strain ranges between 0.0004 and 0.01 and total strain rates between 3.4×10^{-5} and 10^{-4} sec^{-1} . The polycrystalline $\text{Ni}_{49}\text{Al}_{31}\text{Fe}_{20}$ fractured in a predominantly transgranular manner, experienced cyclic softening followed by hardening, and displayed little or no asymmetry between tensile and compressive portions of the load cycle.

Lerch and Noebe have performed room temperature [40] and 1000 K [41] fatigue tests on polycrystalline NiAl at plastic strain ranges between 0.0006 and 0.002 at a total strain rate of 10^{-3} sec^{-1} . At room temperature the polycrystalline NiAl tested in fatigue was more sensitive to pre-existing flaws than identical material tested in tension. Unlike the single crystal material studied by Bain et al., which failed below its monotonic fracture stress, the polycrystalline specimens work hardened continuously at room temperature and failed at stresses averaging 60% higher than

the monotonic fracture stresses. There was measurable asymmetry between the absolute value of the stresses achieved in tension and compression in these tests. The authors contributed the higher compressive stress levels to cracking within the specimens. The room temperature polycrystalline study found that in strain controlled fatigue NiAl had longer lives than other ordered B2 compounds. At 1000 K, polycrystalline NiAl experienced cyclic softening similar to the single crystal behavior. However, at the higher temperature polycrystalline NiAl reportedly suffered from grain boundary oxidation and creep cavitation.

Preliminary results have been published by Smith et al. on fatigue of $\langle 121 \rangle$ oriented, stoichiometric NiAl [42]. They report seeing evidence of persistent slip bands intersecting the specimen surface and dislocation structures similar to those developed during monotonic loading. No mention was made of the method used to confirm that the surface slip bands were indeed continuously active, i.e. persistent.

General trends in low cycle fatigue behavior can be surmised from reported fatigue data. At low temperatures (room temperature is well below the BDTT for the materials discussed), NiAl cyclicly hardened and had little or no stable fatigue crack growth. Two of the groups [36,40] reported that fatigue fractures were initiated more frequently at pre-existing flaws than were the corresponding tensile fractures. At high temperatures, cyclic softening dominated the fatigue behavior of both single and polycrystalline NiAl. For polycrystalline NiAl, there was a two order of magnitude increase in fatigue lives from room temperature to 1000 K when tested at a plastic strain range of 0.002 [40,41]. Unfortunately, the dislocation structures developed during these previous studies have not been reported in detail. The

properties reported at these two temperature extremes (one well below and one well above the BDTT) were quite different.

CHAPTER 3

MATERIAL AND EXPERIMENTAL PROCEDURES

Material and Metallographic Examination

A near stoichiometric NiAl billet was prepared by hot extrusion of vacuum atomized powders produced by Homogeneous Metals, Inc. Prealloyed -20/+325 mesh powders were extruded at 1365 K with approximately a 3:1 reduction in diameter which gives slightly less than an 8:1 reduction in cross-sectional area. The composition is given in Table 3.1. The Al and Ni levels were determined from the extruded product by wet chemical analysis conducted at the NASA Lewis Research Center. The interstitial levels were measured by Homogenous Metals and determined by chemical analysis of the powder.

Transverse and longitudinal metallographic sections were taken from the extrusion. Sections were mounted in Bakelite, hand ground on 180 through 600 grit wheels, and polished with 1 and 3 μm alumina slurries on cloth wheels. Since NiAl is a hard material which is difficult to polish, a special final polish was also used. A solution of 150 ml H_2O , 150 ml colloidal silica, 10 ml H_2O_2 (30%), 1 ml HF (48%), and 1 ml HNO_3 (70%) in conjunction with a clean cloth wheel was used to achieve a smoother surface. Specimens were etched for 1 to 3 minutes with a solution of 100 grams molybdic acid (85%), 150 ml water, 50 ml hydrofluoric acid (48%) to expose

the grain boundaries. Figure 3.1 shows micrographs of both the transverse and longitudinal grain structure. The extruded material had a recrystallized, equiaxed grain structure with an average linear intercept grain size of 39 μm .

Tensile Testing

Uniaxial tensile tests were conducted to determine the monotonic BDTT for this heat of material. Blanks for cylindrical, button-head, tension specimens were electro-discharge machined from the extrusion and ground parallel to the extrusion axis. The tensile specimens had approximately 30 mm long and 3 mm diameter gage sections as shown in Figure 3.2. The gage sections were electropolished in a methanol-10% perchloric acid solution at 205 K and 1.0 Amps prior to testing to eliminate surface flaws that could result in premature failure.

Tensile specimens were tested in a screw-driven Instron test frame at a constant cross-head speed of 0.254 mm/min which corresponded to nominal strain rate of 10^{-4} sec^{-1} . Tests were conducted in air at room temperature (approximately 300 K), 600, 650, and 700 K. Elevated temperatures were achieved using a resistance furnace. Two to three K-type thermocouples were beaded and tied to each tensile gage section using Ni wire. Thermal gradients along the gage section were assumed to be minimal since NiAl has high thermal conductivity ($\sim 40 \text{ W/m K}$ from 600 to 700 K). Measured differences in thermocouple temperatures were less than 4 K.

Load versus time data for the tensile tests were recorded on a strip chart and converted to true stress, (σ), and true strain, (ϵ), values by assuming constant volume during plastic deformation.

$$\sigma = S(1+e) \quad (3.4)$$

$$\epsilon = \ln(1+e) \quad (3.5)$$

The engineering stress, S , was calculated from the instantaneous load in kg and the original cross-sectional. True strain at failure was also measured using reduction in cross-sectional area and the two strain calculations agreed well since there was little necking at the temperatures tested. The true stress-strain curves were digitized for convenient representation. The displacement due to the test frame stiffness was subtracted from the nominal strain following the procedure outlined in Appendix A.

Low Cycle Fatigue Testing

Specimen blanks were electro-discharge machined parallel to the extrusion axis and ground to the final dimensions shown in Figure 3.3. The gage section was approximately 15 mm long with a 4 mm diameter. The long shanks, shown in the figure, were necessary to separate the induction-heated gage section from the water-cooled grip ends. The gage sections were electro-polished using the same procedure as outlined for the tensile specimens, except the current was approximately 0.8 Amps. Tests were conducted on a computer controlled, servo-hydraulic SATEC test frame. Specimens were subjected to fatigue loading between plastic strain limits at a constant total strain rate. LCF tests were run at plastic strain ranges of 0.5% and 1.0% at a total strain rate of 10^{-4} sec^{-1} . The button-head fatigue specimens were held in water-cooled, collar grips. Careful alignment of grips was achieved by measuring lateral and circumferential deviations with dial gages.

Strain measurements were made using a standard MTS 12.7 mm strain-gage extensometer that had been adapted for use at high temperatures. Alumina rods with long flat tips were used to extend the strain-gage knife blades, as shown in Figure 3.4. Spring tension between the alumina blades and the test frame itself was used to hold the blades in place. The adapted extensometer mounted to a specimen is shown in Figure 3.5. The geometry of the set-up leads to a reversed polarity of the displacements measured. The initial spacing between the alumina tips was measured with a travelling microscope. Calibration of the lengthened extensometer was achieved by dictating a known displacement using a dial micrometer, calculating the actual strain based on the initial blade spacing, and adjusting the control unit potentiometer such that the strain calculated was associated with the corresponding analog voltage.

All analog voltages measured by the transducers for this test frame (load, displacement, and strain) were calibrated in English units. The frame controller converted these analog inputs to digital values which could be represented in up to three types of units. Conversion constants were entered into the central processing unit such that load was monitored as stress (instantaneous load divided by the specimen's original cross-sectional area and adjusted by the appropriate unit conversion constants), displacement was monitored in millimeters, and total strain was monitored as millistrain (strain multiplied by 10^3). The control unit was also responsible for continuous calculation of plastic strain, ϵ_p . This was accomplished by subtracting the calculated elastic strain, ϵ_e , ($\epsilon_e = \sigma/E$ where σ is the real-time, instantaneous stress and E is the slope measured from the linear elastic response of the specimen) from the real-time, instantaneous total strain, ϵ_t . For each cycle of a

fatigue test, the displacement rate was being dictated by the measured total strain and the end points for the cycle were dictated by the calculated plastic strain. During fatigue testing, data collection consisted of recording stress verses time on a strip chart, stress verses total strain on a x-y recorder, and stress verses total strain on a computer data acquisition system (SATEC's Gentest).

The LCF test temperatures of 600, 675, and 700 K were chosen based on the monotonic test results and achieved using a 2 KW induction furnace. The induction coil was designed by trial and error to achieve uniform heating. The final coil was made of 6.35 mm, copper tubing. Three wraps were made, pancake style, to coincide with each shoulder and were connected by a straight segment parallel to the specimen gage, Figure 3.6. K-type thermocouples were beaded and then melted onto the specimen surface using a spot welding technique and very low current. Repeated heating of several different specimens with as many as seven thermocouples melted to the gage and shoulders determined that a maximum temperature gradient of 10 K could be achieved in the gage section when the coil was properly centered. When using thermocouples attached only at the top and bottom shoulders to control the furnace, the average gage temperature could be maintained within ± 5 K of the desired temperature.

Microscopy

Fracture surfaces and gage section surfaces were examined in a Hitachi S-800 scanning electron microscope (SEM) with a field emission tip and a Cambridge with a tungsten filament. Transmission electron microscopy (TEM) was conducted on a JOEL 100 CX at accelerating voltages of 100 and 150 KeV. Foils were prepared

from as-extruded material to confirm that the preparation process was not introducing deformation. Burger's vector analysis was conducted using the $\mathbf{g \cdot b}$ invisibility criterion. The 180° ambiguity frequently encountered in TEM analysis was avoided by generation of a stereographic projection (for the beam direction normal to the foil) for each grain analyzed.

Discs for TEM foils were sliced from gage sections using a low speed saw and silicon carbide blades. Foils prepared directly from gage slices had a 4 mm diameter and would only fit in a single tilt, TEM holder. A small number of discs, with larger initial thickness were mechanically ground to diameters near 3 mm for use in a double tilt, TEM holder. Discs were then mechanically ground to thicknesses of 0.18 to 0.25 mm using 400 and 600 grit paper. TEM foils were prepared by thinning discs in a solution of 70% ethanol, 13.7% water, 10% butyl cellosolve, and 6.3% perchloric acid. A Tenupol twin jet polisher was used with polishing conditions of approximately 268 K and 0.2 amps. The foils initially ground to the smaller diameter were closely compared to other foils from the same specimen to ensure that the dislocation structure was not altered.

CHAPTER 4

RESULTS AND DISCUSSION

Tensile Testing

The true stress versus true strain data for tensile tests conducted at $\dot{\epsilon} = 10^{-4} \text{ s}^{-1}$ are shown in Figure 4.1 (initial strain off-set from zero for clarity). The room temperature (300 K) test failed elastically. Previous work in NiAl has shown that when a yield stress could be measured for a given test condition (same strain rate and test temperature) in both tension and compression the yield values were very similar [16]. The fracture stress for tensile specimens which failed prior to yielding was found to be essentially equal to the compressive yield stress [16]. Thus the fracture strength for the tensile specimen tested at room temperature in the present study was assumed to also be the yield strength for that test condition based on these prior results. For this heat of material tested at 10^{-4} s^{-1} , the yield stress dropped from 155 MPa at 300 K to 141 MPa at 700 K and the fracture stress increased from 155 to 374 MPa in the same temperature range. The percentage of intergranular fracture, relative to transgranular cleavage, in the fracture surfaces decreased with increasing temperature from $39 \pm 4\%$ intergranular at 600 K to $28 \pm 2\%$ at 700 K, Figure 4.2. This change in fracture morphology results from two inter-related phenomena. Dislocation nucleation and mobility increases at higher temperatures

such that cleavage rather than crystallographic fracture is promoted within an individual grain. Also, dislocation climb is activated near the grain boundaries allowing shape-change accommodation at temperatures above the BDTT.

Figure 4.3 demonstrates that tensile elongation showed a rapid increase with temperature and closely resembled previously published curves [15]. Plastic strain was calculated both from the load-time chart by assuming constant volume and by calculating the reduction in area from the diameter of the gage after failure. Good agreement was obtained from these two methods. A BDTT of 650 K was determined from the data in Figure 4.3 by drawing a smoother curve through the data points and identifying the temperature which corresponded to a plastic elongation of 5%. This BDTT is slightly high compared to average transition temperatures for extruded NiAl [14,16]. Of the factors identified in reference 16, the vacancy content resulting from the cooling rate from the extrusion is the most likely reason for the high BDTT of this heat. The composition and interstitial content of this alloy is comparable to those studied previously [16].

Low Cycle Fatigue Testing

Fatigue tests were conducted on a different equipment set-up than the monotonic tests. A single fatigue-geometry specimen was tested unidirectionally on the SATEC frame to confirm that uniform data were achieved on the two different testing set-ups. Table 4.1 shows the scatter in data between the two samples tested on different frames was no greater than one might expect for repeat test using the same equipment. Fatigue specimens were then tested with $\dot{\epsilon} = 10^{-4} \text{ s}^{-1}$, at one temperature below the BDTT and two above, and at plastic strain ranges of 1.0%

and 0.5%. Fatigue tests were conducted at 600, 675, and 700 K; temperatures which corresponded to monotonic tensile ductilities of approximately 2, 7, and 18%.

Fatigue Response

The change in fatigue response with temperature for both plastic strain ranges is shown in Figure 4.4. Cumulative plastic strain used as the horizontal axis in these figures is the number of cycles multiplied by the imposed plastic strain range. Cyclic hardening curves for all valid tests are given in Appendix B along with a summary of test conditions. Figure 4.5 shows an example of the hysteresis loops which were recorded intermittently on an x-y plotter. These hysteresis loops confirmed the accuracy of the test control and provided stress amplitude data as a function of number of cycles. In all test conditions, rapid hardening occurred for the first few cycles. No cyclic softening or load drop was observed under any conditions. Figure 4.6 shows the estimated fatigue life curves for 600 and 700 K using the universal slopes equation which is a common method to estimate fatigue behavior. Since there was no necking at these temperatures, the monotonic fracture strength was substituted for ultimate strength in equation 2.3 to predict these curves. Also shown in Figure 4.6 are the results of this study plotted as total strain range at the end of life versus cycles. These data points are not statistically significant because scatter is usually large in fatigue results. It is notable, however, that in some respects the fatigue response of this intermetallic follows the trends established from the behavior of normal metals.

The shape of the cyclic hardening curves (Figure 4.4 and Appendix B) did not change significantly for different test conditions within this test matrix. Many of the

tests which had extensive lives (greater than 100% cumulative strain) showed increased hardening toward the end of their lives. For ease of discussion, the cyclic hardening curves were divided into four regions, Figure 4.7. These regions were characterized by an initial hardening region, a stress plateau, additional hardening, and a return to relative stability. Duplicate tests or interrupted tests always yielded the same cyclic hardening curves, an example of which is given in Figure 4.8 (a,b). A slight asymmetry was seen between tensile and compressive stress amplitudes under the most severe test condition, 600 K and 0.1% plastic strain range, Figure 4.9 (a). As illustrated in Figure 4.9 (b) however, most test conditions did not result in noticeable differences between the magnitude of tensile and compressive stresses measured in a given load cycle.

Fracture Surface Observations

The fracture surfaces of the fatigue tests looked surprisingly similar to those of the tensile tests, Figure 4.10 (a,b). Figure 4.10 (b) shows the internal inclusion that initiated the fracture. X-ray dispersive analysis indicated high levels of Si in the inclusions. These inclusions were non-metallic and quite likely silica which is a common crucible material used in metal powder production. At 600 K all fatigue fractures initiated at internal inclusions, like the one shown in Figure 4.10 (b). Above the BDTT, some failures initiated at inclusions but repeat test had longer lives and failures were initiated at the surface. Therefore at 675 and 700 K, flaw sensitivity appeared to be diminishing.

There were no clear demarcations between areas of cyclic crack growth and fast fracture for any of the specimens. Studying the fracture surfaces would suggest

that the critical flaw size was quite small and that fast fracture dominated much of the surface. The regions directly adjacent to the fracture initiation sites were one hundred percent transgranular cleavage, but that is also the case for tensile fracture which initiate at a macroscopic flaw. The percentage of intergranular fracture in the bulk fracture surfaces of fatigue specimens tested at $\Delta\epsilon = 0.5\%$, Figure 4.11, decreased with increasing test temperature from $47 \pm 6\%$ at 600 K to $33 \pm 4\%$ intergranular fracture at 700 K following the same trends seen in the monotonic failures. If the bulk of the fatigue fracture surface did indeed result from tensile overload, then the monotonic and cyclic fracture morphologies should be the same at a give temperature. Note that the percentage of intergranular fracture for the fatigue test at 675 K and $\Delta\epsilon = 0.005$ was unexpectedly low, 32%, but this specimen failed at a very short life from an unusually large inclusion.

Surface Deformation Observations

The gage surfaces of fatigue samples showed evidence of deformation. Slip traces and secondary cracking were common on specimens cycled to failure. Surface slip traces occurred at all temperatures and both strain ranges on specimens which reached initial saturation. Figure 4.12 (a,b) shows an example of slip bands which developed into distinct extrusions on the surface of a specimen which failed in region IV. The samples which had lives longer than 1500 cycles showed not only the macroscopic slip bands seen in many samples, but also contained very fine lines, Figure 4.12 (b). These fine slip bands were quite linear and uniformly spaced, and were only observed in specimens which were deformed into region IV. The concentration of slip traces was slightly higher near the fracture surface, but they

were not limited to the center of the gage section. Even surfaces which had fairly sparse bands of intrusions/extrusions had bands extending to the shoulder radius, Figure 4.13 (a,b). Transgranular cracks were seen forming at some deep slip bands. In addition, intergranular cracks were seen opening between grains which contained slip traces.

Surface deformation was found to increase with the amount of imposed deformation and with decreasing test temperature. Figure 4.14 tracks the increasing deformation density for samples tested at 600 K and $\Delta\epsilon_p = 0.5\%$. The two specimens tested at 600 K and $\Delta\epsilon_p = 1.0\%$, Figure 4.15 (a,b), failed at the beginning of region II and revealed the most striking evidence of increasing deformation density. Both failures were initiated at internal inclusions; one of the specimens failed after 8 cycles and the other after 10. The surface deformation on the sample with 10 cycles 4.15(b) was noticeably more extensive than the deformation on the sample with 8 cycles 4.15(a). Three examples are included which demonstrate the effect of increasing temperature on the extent of surface deformation. Figures 4.16 and 4.17 show surfaces from samples deformed at 700 K to the onset of stability (beginning of region II) at $\Delta\epsilon_p = 0.5\%$ and 1.0% , respectively. The sample tested at 600 K, Figure 4.14 (b), had sparse but noticeable bands of intrusions and extrusions while the surface shown in 4.16 tested at 700 K more closely resembles a tensile test or undeformed sample. The sample shown in Figure 4.17 can be compared to Figure 4.15(a,b) above. Although there was evidence of embryonic slip bands forming at the beginning of stability at 700 K, Figure 4.17, these bands were noticeably less developed than either of the samples shown in 4.15 which were tested at 600 K. Figure 4.18(a,b) were both tested above the BDTT and interrupted in

stage III. Although the sample tested at 675 K had 100 cycles less than that tested at 700 K, the surface deformation was more developed as a result of the lower test temperature.

Internal Deformation Observations

While the as-extruded material used in this study was virtually free of dislocations, TEM analysis showed that the dislocation density was high in the interior of the fatigued specimens. Burgers vector analysis was conducted on specimens which were interrupted early in life for strain amplitudes of 0.5% tested at 600 and 675 K. All the dislocations identified had $\langle 100 \rangle$ Burgers vectors. Dislocation morphologies observed after cyclic deformation were regions of uniformly distributed tangles, equiaxed cells, elongated cells, and dislocation veins all with walls of varying thickness. The dislocation veins crossed the width of a grain virtually unobstructed. Elongated cells, on the other hand, had lengths less than the grain width and were usually not as well aligned as veins. The interiors of the cells and the regions between veins frequently contained dislocation loops. The morphology of the dislocation structures changed with increasing deformation but did not change as a function of temperature. The dislocation density did, however, appear to decrease with increasing test temperature.

Observations of the dislocation structures implied that the changing morphologies corresponded to the changing shape of the cyclic hardening curves. Test specimens interrupted during the initial hardening stage of fatigue, region I, had dislocation structures which resembled those reported for interrupted monotonic deformation [16,25]. After as little as one fully reversed cycle of $\Delta\epsilon_p = 0.5\%$,

Figure 4.19 shows that a cellular structure was beginning to form. After five cycles under the same test conditions, cells with thick walls of dislocations could be readily identified. Cellular morphologies dominated through region II of the fatigue curve with some cells being elongated and some being equiaxed in shape, Figure 4.20(a,b). Samples which were deformed into regions III and IV had dislocation morphologies which were predominantly filled with veins of dislocation tangles. The transitions were not precise, but detailed observations suggest that the predominant structure changed with cumulative deformation. Figure 4.21 shows a typical cyclic hardening curve for a specimen deformed to failure at 600 K, $\Delta\epsilon_p = 0.5\%$ and the characteristic dislocation structures from interrupted samples tested under those conditions. A similar figure is shown in Figure 4.22 for samples tested at 700 K, $\Delta\epsilon_p = 1.0\%$. It is interesting to note that grains, or large areas of grains, devoid of a well defined structure and containing uniformly distributed dislocation tangles were infrequent in tests interrupted in regions I or II but fairly common in tests to failure in regions III and IV.

The same geometry of dislocation arrangements seemed to be present at all three temperatures. At 700 K as well as 600 K samples interrupted early in the fatigue life contained mostly cellular arrays. Samples fatigued into regions III and IV (on cyclic hardening curves) had large areas of well aligned veins and areas that had been filled with tangles. Figure 4.23 illustrates the two types of microstructures seen at the end of fatigue life for both 600 and 700 K. Also seen in Figure 4.23 is an apparent decrease in dislocation density and increase in the spacing of the veins with increasing test temperature. Foil thicknesses were not measured, so precise dislocation densities can not be assessed. However, the foil preparation procedures

were consistent and enough foils were observed at the different temperatures to comment on trends in dislocation densities. A decrease in dislocation density with increasing temperature was consistent with the reduced accumulation of surface damage at the higher temperatures. Dislocation mobility should increase with increasing temperature suggesting that the dislocation density needed to produce a given amount of strain would be less at the higher temperatures.

Analysis of Low Cycle Fatigue Properties

The fatigue properties of polycrystalline NiAl tested between 600 and 700 K were evaluated to determine behavior trends. Comparisons were made within the test matrix, between these tests and those previously reported, and comparisons were made between these tests and predictions based on monotonic behavior. The cyclic hardening curves shown in Figure 4.4 (and in Appendix B) suggested that the deformation mechanisms were not changing within this temperature range because the shape of these curves was not altered. Yet, the accumulation of damage, determined by sample hardening, was changing with changes in strain or temperature. The development of the surface deformation, higher density with increasing strain at a constant temperature and lower density with increasing temperature at a constant level of strain, concurred with the trends suggested by the cyclic hardening curves. Low cycle fatigue properties did not change abruptly within the 100 K temperature range. The change in the saturation stress, shown in Figure 4.24, associated with Region II on the cyclic hardening curves indicated a possible transition associated with the monotonic BDTT.

When compared to the previously cited fatigue studies, the fatigue properties of NiAl between 600 and 700 K more closely resembled the behavior at room temperature. NiAl cyclicly hardened under all the test conditions between 600 and 700 K in agreement with low temperature results and in contrast to those at 1000 K. The similarity was however not exact; the cyclic hardening curves at room temperature hardened continuously without the stress plateau seen in tests conducted near the BDTT. Also analogous to the low temperature behavior, the fracture surfaces in the temperature range of this study showed little if any cyclic crack growth. The initiation sites were surrounded by transgranular cleavage, but these regions could not be precisely identified as ones of cyclic growth. These cleavage facets did not show typical fatigue damage and looked similar to cleavage facets found on tensile surfaces. It was interesting to note that both of the previous room temperature studies which have been reported in some depth [36,40] commented on the sensitivity of the fatigue tests to pre-existing flaws. Based on the number of fractures initiated at inclusions, the fatigue tests conducted between 600 to 700 K were more sensitive to pre-existing flaws than the monotonic tests from the same material. Data from this study were however insufficient to draw firm conclusions on the flaw sensitivity since the tensile and fatigue specimens were not taken randomly from the extrusion.

Fatigue behavior estimates were made from the monotonic properties to ascertain the extent to which NiAl follows these conventional rules-of-thumb. Table 4.2 lists the monotonic failure strength and ductility at the two temperature extremes used for fatigue conditions as well as the strain hardening exponent calculated from these tensile tests. The strain hardening exponent for this heat of

NiAl was greater than both the empirical values mentioned previously and thus would predict the cyclic hardening seen under these test conditions.

Cycles-to-failure predictions were made using the Coffin/Manson power law function, equation 2.2, with the appropriate strain ranges and the monotonic strain to failure listed in Table 4.2. Brittle materials generally have lower values of c , so the value of -0.5 was chosen for these calculations. The Coffin/Manson relation predicted a two order-of-magnitude jump in cycles to failure (25 to 2650 cycles) between 600 and 700 K for samples tested at $\Delta\epsilon_p = 0.5\%$. The fatigue life increased by slightly more than two times within this temperature range for plastic strain ranges of 0.5%, but that increase was modest compared to the prediction. The change in fatigue life was much greater for the tests conducted at $\Delta\epsilon = 1.0\%$, where the increase in life was two orders of magnitude and actual lives (10 cycles at 600 K) were more similar to predictions (7 cycles at 600 K). Conventional wisdom suggests that large increases in ductility greatly affects the fatigue life of a material in the low cycle fatigue regime. These rule-of-thumb life estimates suggested that fatigue behavior more closely followed conventional trends at the higher but not at the lower plastic strain range. The strengths achieved at 600 K for both strain ranges, however, suggested non-conventional behavior. At both strain ranges, the stress amplitude cyclicly hardened to approximately 300 MPa at 600 K compared to tensile fracture strength of approximately 250 MPa. These figures indicate that the cyclic fracture stress exceeded the monotonic fracture stress by approximately 20%. Much less than the 60% increase measured in room temperature fatigue, but a meaningful trend nonetheless suggesting that a significant change in deformation mode is taking place from monotonic to cyclic loading.

Analysis of Internal Deformation

The dislocation structures developed in other NiAl low cycle fatigue studies have not been thoroughly documented so comparisons are not possible. Interesting correlations can, however, be drawn between the mechanical properties observed and the deformation developed in fatigue for NiAl in this temperature range. As noted in the Chapter 2, slip systems are normally the same for material deformed monotonically and cyclicly. Since $\langle 100 \rangle$ dislocations have dominated polycrystalline tensile and compressive deformation in all previous studies, a large presence of other dislocation types would be unexpected.

The elongated cells and vein structures were initially thought to result from planar dislocation glide. Tilting a foil along an axis coinciding to the length of a vein proved to be inconclusive. If vein structure had been a slice through a plane of dislocations, then a sufficient angle of tilt would lead to a change in the apparent thickness of the vein. There was not a significant change in thickness of the veins. The lack of change could mean that the structure was not planar or just that the applied tilt was insufficient to see a change in thickness. Stereo-imaging of cell structures developed early in fatigue showed that these initial structures were definitely three dimensional, not planar. Stereo-images of veins and elongated cells could not determine the dimensional nature of these structures because the high density within the tangles made resolution of individual dislocations difficult. Making the 3 mm diameter foils necessary for stereo-pair micrographs took considerably longer than the 4 mm foils so an attempt was made to gain as much information as possible from the single tilt, TEM holder.

If the slip was indeed planar, the veins seen on TEM micrographs would represent one cross-section of a plane of dislocations. The apparent line direction, which can be measured on a micrograph relative to its \mathbf{g} vector, would then be one of many line directions within the plane of dislocations. Any plane is designated by its direction-normal, but the angular relationship between the apparent line direction and the actual direction normal to the plane of dislocation could not be identified from a single micrograph. The plane perpendicular to the apparent line direction would contain the direction-normal of interest. The direction-normal could be identified as the line of intersection between all of the planes perpendicular to the apparent line directions from micrographs taken with different \mathbf{g} vectors. More details on this approach as well as an example can be found in Appendix C. Analysis of six vein or elongated cell regions from different test conditions indicated no good agreement on a possible characteristic plane. In fact, most of these analyses did not clearly indicate any low index plane.

Calculations were also conducted assuming the observed structures were not planar. If the veins seen in TEM pictures were in fact three-dimensional bundles, they would not be contained in a single crystallographic plane. Each vein would have a characteristic line direction; although the line direction need not be a low index direction. To determine the possible line direction for a given vein, again, required multiple TEM micrographs. Each micrograph gave one angle between a particular \mathbf{g} and the apparent line direction. The actual vein direction would be contained in a plane defined by the beam direction and the apparent line direction. Different vein-containing planes were determined using various diffraction conditions. The

intersection of these planes was considered the characteristic line direction of the vein of interest. An example of this approach can also be found in Appendix C. Four regions from different test conditions were analyzed using this approach. Three of the four gave a possible line direction near a $\langle 100 \rangle$ pole and one was near a $\langle 110 \rangle$ pole. The results of this second approach combined with the successful stereo-imaging of the cells developed early in fatigue life suggested that the veins were not planes of dislocations. To be completely certain, a larger number of veins and elongated cells should be analyzed to determine if the characteristic directions do indeed correspond to $\langle 100 \rangle$ and $\langle 110 \rangle$ directions.

A well defined, organized dislocation structure was seen after as little as five fully reversed cycles. The similarity between this structure and those seen in interrupted monotonic tests indicated the initial deformation mechanisms were the same. Either cross slipping dislocations or tangling of dislocations on intersecting glide planes could have led to this structure. This cellular dislocation morphology was seen throughout the initial hardening portion, region I, of the cyclic hardening curve.

Areas of elongated cells were noticed early in the plateau region of the cyclic hardening curve. When the lives were interrupted later in the curve, more areas of elongated cells were observed as well as regions containing distinctive veins. Within region II, the change in stress was minimal as the cells transformed to the vein structure. Dislocations could move with less resistance between the long veins than between the cells. The dominance of the vein structure was quite evident within the samples deformed into regions III and IV. At the end of the fatigue lives, there were also more numerous and larger regions of the uniformly distributed tangles. The hardening after the plateau could indicate a significant breakdown in veins. The

slightly increasing stress during the plateau region would lead to slightly decreasing vein spacing. Eventually the movement of the dislocations between the veins would no longer accommodate the imposed strain. Rather than simply moving between veins, dislocations tangled and filled-in between the veins.

The previous explanation of developing dislocation structures correlates the shape of the cyclic hardening curves with the changing dislocation morphology as a function of longer lives. The apparent change in dislocation density is more easily understood. The initial flow stress, in both monotonic and cyclic deformation, was lower at higher test temperatures which would result in a lower number of initial dislocations. This lower initial density meant a larger mean free path for subsequent deformation and, for given imposed strain, a smaller dislocation density generated per cycle. The general mobility of the dislocation was also larger at the higher temperatures leading to easier cross slip and annihilation.

Small dislocation loops were evident in all the deformed TEM specimens, an example of which is seen in Figure 4.25. The density of these loops increased noticeably with the duration of the tests. A change in the number of these loops was not assessed for different test temperatures. Dislocation loops can occur as the result of several sources such as accommodating stresses around precipitates and vacancy clusters or as debris from moving dislocation jogs.

The growth of small precipitates is often heralded by dislocations accommodating the mismatch around them. The growth of precipitates in this material is unlikely due to the good chemical stability of NiAl and the low impurity content of this particular alloy (see Table 3.1 from Experimental Procedures). Dislocation loops also form as a result of stresses due to small voids or clusters of

vacancies. NiAl has been shown to retain a large number of quenched-in vacancies [43] and these vacancies can affect material properties [16,44]. However, these loops were not created by the heat treatment associated with testing alone as shown by TEM analysis of a specimen which was held at 600 K for the time equivalent to 1000 cycles without noticeable development of loops, Figure 4.26.

The loops could be the result of the motion of dislocations containing superjogs. This type of loop formation was used to explain debris seen in $\langle 100 \rangle$ single crystals [13]. Johnston and Gilman [45] and Tetelman [46] have described dislocation movement which would result in the generation of dislocation loops from superjogs either by a cross-slip mechanisms or partial annihilation of dislocations on parallel planes. Either type of loop production would explain the extreme regular spacing of loops in some areas, Figure 4.25 and correlates with the presence of long, bowing dislocations and the presence of elongated loops.

CHAPTER 5

CONCLUSIONS

Low cycle fatigue tests were successfully performed on near stoichiometric NiAl at intermediate temperatures near the monotonic brittle-to-ductile transition. Changes were observed in the low cycle fatigue properties in the same temperature range as the monotonic BDTT, but the transition in fatigue properties was not abrupt as predicted by the changes in monotonic ductility. The NiAl fatigue deformation behavior at the intermediate temperature ranges tested in this research program more closely resembled that of previous room temperature fatigue tests than 1000 K tests. From 600 to 700 K, fatigue specimens exhibited hardening reminiscent of previously reported low temperature behavior. NiAl tested to failure had fatigue fracture surfaces dominated by fast fracture and characteristic of materials with low fracture toughness even under test conditions that resulted in 18% tensile elongation. There was however decreased fatigue strength with increasing temperature which suggested a gradual transition to the previously reported high temperature softening.

The dislocation morphologies found in this study, in conjunction with the shape of the cyclic hardening curve, suggest an evolution of fatigue deformation substructures. The cyclic hardening curves could be divided into four regions of deformation. During the period of initial hardening, a uniform cell structure developed. Throughout the stress plateau, the equiaxed cells morphology

transformed to an elongated cell morphology. Near the end of fatigue life a well defined structure of parallel veins had formed. As the spacing between the veins became smaller, dislocation movement between veins was insufficient to accommodate deformation and the space between the veins began filling with dislocation tangles. Thus the increased hardening towards the end of fatigue life could be associated with the breakdown of the vein structure created during the initial stress plateau. The second plateau, or fourth region of the cyclic hardening curves, suggested the development of another stable dislocation structure. The apparent lower density of dislocations in specimens tested at higher temperatures was consistent with the lower stress levels measured, the lower rate of surface deformation accumulation and the increased dislocation mobility expected above the monotonic BDTT.

There were strong indications that the predominate deformation mechanisms in NiAl were changing from monotonic to cyclic testing at temperatures below the brittle-to-ductile transition. The significant increase in fatigue fracture stress over monotonic fracture stress at 600 K demonstrated that higher levels of damage were accumulated in fatigue. This increased fatigue strength relative to monotonic strength was even larger in previously reported room temperature tests. The cellular dislocation structures which develop during monotonic deformation also developed in the initial hardening portion of the fatigue tests. The transformation of the dislocation structure from equiaxed cells to elongated cells must be effectual in producing the higher stresses because the samples cyclicly tested at 600 K exceeded their monotonic strength during the initial hardening portion of the cyclic curve. The NiAl low cycle fatigue lives could be reasonable well predicted by conventional

methods at temperatures above the monotonic BDTT. However, the unexpectedly high fatigue strengths at temperatures below the monotonic BDTT led to longer than expected lives and the unexpectedly gradual transition in fatigue behavior with increasing temperature.

CHAPTER 6

SUGGESTIONS FOR FUTURE RESEARCH

Much has been learned about the fatigue properties of NiAl in the past two years. Initial comparisons between the fatigue properties of NiAl and other B2 intermetallics [30] and superalloys [26] have been encouraging. Moreover, intermediate temperature properties follow conventional trends. The extremely small region of cyclic crack growth (essentially non-existent at the temperatures between 600 and 700 K) is, however, cause for concern. Further research is necessary to obtain a complete representation of fatigue deformation for NiAl.

Subsequent studies at intermediate temperature such as those probed in this project should include further TEM work. Since it is now known that the properties do not change radically in this temperature range, one test condition could be used for an in depth study of the fatigue mechanisms. Interrupted tests need to be taken at several points during region II and the transition between regions II, III and IV need further probing. Larger quantities of TEM foils could be examined for these interrupted tests to obtain exact percentages of dislocation structures at different interrupted lives.

Significantly more information is needed on internal deformation structures from LCF at all temperatures. Comparisons between dislocation activity in near surface and interior regions would be informative. Such comparisons are important

since macroscopic fatigue damage lead to crack initiation on the surface. These types of experiments are, however, far from trivial to perform, as expounded upon by Keller, et al. [24].

Additional testing as a function of temperature should be conducted to look for the transition from nominally stable behavior to the extensive softening which occurs at 1000 K. Of course the issues of creep/fatigue interaction and the effects of oxidation become important at the higher temperatures. The need for materials with ever increasing use temperatures will always exist. The NiAl system, monolithic or composite, continues to show promise but there are many exciting issues remaining to be explored.

REFERENCES

1. E.M. Grala, "Investigations of NiAl and Ni₃Al," in *Mechanical Properties of Intermetallic Compounds*, edited by J.H. Westbrook (John Wiley & Sons, New York, 1960) 358-402.
2. R. Darolia, "NiAl Alloys for High-Temperature Structural Applications," *JOM*, **43**(3), 44-49, 1991.
3. R.R. Bowman and R.D. Noebe, "Development of NiAl and NiAl-based Composites for Structural Applications: A Status Report," in *Superalloys 1992*, edited by S.D. Antolovich, et al. (TMS, Warrendale, PA, 1992) 341-350.
4. J.D. Whittenberger, R. Reviere, R.D. Noebe and B.F. Oliver, "Compressive Strength of Directionally Solidified NiAl-NiAlNb Intermetallics at 1200 and 1300 K," *Scripta Metall. Mater.*, **26** 987-992, 1992.
5. M.F. Singleton, J.L. Murray and P. Nash, "Aluminum Nickel," in *Binary Alloy Phase Diagrams*, edited by T.B. Massalski (ASM, Metals Park, OH, 1986) 140-143.
6. R.D. Noebe, R.R. Bowman and M.V. Nathal, "Review of the Physical and Mechanical Properties and Potential Applications of the B2 Compound NiAl," accepted for publication in *Inter. Mater. Review*, 1993 (also available as NASA TM-105598, 1992).
7. J.P. Neumann, Y.A. Chang and C.M. Lee, "Thermodynamics of Intermetallic Phases with the Triple-Defect B2 Structure," *Acta Metall.*, **24**, 593-604, 1976.
8. G.G. Libowitz, "Point Defects and Thermodynamic Properties in CsCl-Type Intermetallic Compounds," *Met. Trans.*, **2**, 85-93, 1971.
9. A.J. Bradley and A. Taylor, "An X-Ray Analysis of the Nickel-Aluminium System," *Proc. R. Soc.*, **A159**, 56-72, 1937.
10. W.A. Rachinger and A.H. Cottrell, "Slip in Crystals of the Caesium Chloride Type," *Acta Metall.*, **4**, 109-113, 1956.
11. A. Ball and R.E. Smallman, "The Operative Slip System and General Plasticity of NiAl," *Acta Metall.*, **14**, 1517-1526, 1966.
12. M.H. Loretto and R.J. Wasilewski, "Slip Systems in NiAl Single Crystals at 300°K and 77°K," *Phil. Mag.*, **8s.23**, 1311-1328, 1971.

13. R.D. Field, D.F. Lahrman and R. Darolia, "Slip Systems in $\langle 001 \rangle$ Oriented NiAl Single Crystals," *Acta Metall. Mater.*, **39**, 2951-2959, 1991.
14. R.D. Noebe, R.R. Bowman, C.L. Cullers and S.V. Raj, "Flow and Fracture Behavior of NiAl in Relation to the Brittle-To-Ductile Transition Temperature," in *High Temperature Ordered Intermetallic Alloys IV*, edited by L. Johnson, D.P. Pope and J.O. Stiegler (*Mater. Res. Soc. Proc.* **213**, Pittsburgh, PA, 1991), 589-596.
15. R.D. Noebe, C.L. Cullers and R.R. Bowman, "The Effect of Strain Rate and Temperature on the Tensile Properties of NiAl," *J. Mater. Res.*, **7**(3), 605-612, 1992.
16. R.R. Bowman, R.D. Noebe, S.V. Raj and I.E. Locci, "Correlation of Deformation Mechanisms with the Tensile and Compressive Behavior of NiAl and NiAl(Zr) Intermetallic Alloys," *Met. Trans.*, **23A**, 1493-1508, 1992.
17. R. v. Mises, "Mechanik der plastischen Formänderung von Kristallen (Mechanics of Plastic Form Change of Crystals)," *Z. Angew. Math. Mech.*, **8**(3), 161-185, 1928.
18. G.W. Groves and A. Kelly, "Independent Slip Systems in Crystals," *Phil. Mag.*, **8s.8**, 877-887, 1963.
19. A. Ball and R.E. Smallman, "The Deformation Properties and Electron Microscopy Studies of the Intermetallic Compound NiAl," *Acta Metall.*, **14**, 1349-1355, 1966.
20. H.L. Fraser, M.H. Loretto and R.E. Smallman, "The Plastic Deformation of NiAl Single Crystals Between 300°K and 1050°K: II. The Mechanisms of Kinking and Uniform Deformation," *Phil. Mag.*, **8s.28**, 667-677, 1973.
21. R.D. Noebe, R.R. Bowman, C.L. Cullers and S.V. Raj, "Flow and Fracture Behavior of NiAl with Prospects for Future Alloy Development," *HITEMP Review-1990*, (NASA CP-10051, 1990) 20-1 to 20-19.
22. G.W. Groves and A. Kelly, "Change of Shape due to Dislocation Climb", *Phil. Mag.*, **8s.19**, 977-986, 1969.
23. J.E. Hack, J.M. Brzeski and R. Darolia, "Evidence of Inherent Ductility in Single Crystals of the Ordered Intermetallic Compound NiAl," *Scripta Metall. Mater.*, **27**, 1259-1263, 1992.
24. P.S. Khadkikar, G.M. Michal and K. Vedula, "Preferred Orientations in Extruded Nickel and Iron Aluminides," *Met. Trans.*, **21A**, 279-288, 1990.
25. P. Nagpal and I. Baker, "Dislocation Arrangements in Polycrystalline NiAl after Room-temperature Deformation," *J. Mater. Sci. Let.*, **11**, 1209-1210, 1992.

26. G.E. Dieter, *Mechanical Metallurgy*, Metric Edition (McGraw-Hill Inc., New York, 1976) p. 390.
27. J.A. Bannantine, J.J. Comer and J.L. Handrock, *Fundamentals of Metal Fatigue Analysis*, (Prentice Hall, Englewood Cliffs, NJ, 1990), p. 52.
28. G.E. Dieter, *Mechanical Metallurgy*, Metric Edition (McGraw-Hill, Inc., New York, 1976) p. 394.
29. C.E. Feltner and C. Laird, "Cyclic Stress-Strain Response of F.C.C. Metals and Alloys--II Dislocation Structures and Mechanisms," *Acta Metall.*, **15**, 1633-1653, 1967.
30. P. Lukáš, L. Kunz and J. Krejčí, "Effect of Slip Planarity on the Cyclic Stress-Strain Curve, Dislocation Structure and Surface Relief in F.C.C. Single Crystals," *Scripta Metall. Mater.*, **26**, 1511-1516, 1992.
31. C. Laird, "Recent Advances in Understanding the Cyclic Deformation of Metals and Solid Solutions," in *Work Hardening in Tension and Fatigue*, edited by A.W. Thompson (TMS, Warrendale, PA, 1976) 150-174.
32. H.J. Roven and E. Nes, "Cyclic Deformation of Ferritic Steel--I. Stress-Strain Response and Structure Evolution," *Acta Metall. Mater.*, **39**, 1719-1733, 1991.
33. R.R. Keller, W. Zielinski and W.W. Gerberich, "Fatigue-Induced Surface versus Bulk Dislocation Arrangements in Iron Alloys," *Scripta Metall. Mater.*, **26**, 1523-1528, 1992.
34. H. Mughrabi, "Introduction to the Viewpoint Set on: Surface Effects in Cyclic Deformation and Fatigue," *Scripta Metall. Mater.*, **26**, 1499-1504, 1992.
35. T.L. Lin, W. Jiansheng and C. Xianfeng, "Dislocation Behavior During Cyclic Deformation of Niobium Single Crystals," *Mater. Sci. Eng.*, **86**, 19-27, 1987.
36. K. R. Bain, R. D. Field and D. F. Lahrman, "Fatigue Behavior of NiAl Single Crystals," presented at the 1991 Fall TMS Meeting, Cincinnati, OH 1991 (unpublished).
37. K.R. Bain, private communication, October 1992.
38. S. E. Hartfield-Wünsch and R. Gibala, "Cyclic Deformation of B2 Aluminides," in *High Temperature Ordered Intermetallic Alloys IV*, edited by L. Johnson, D.P. Pope and J.O. Stiegler (*Mater. Res. Soc. Proc.* **213**, Pittsburgh, PA, 1991), 575-580.
39. S. E. Hartfield-Wünsch, "Monotonic and Cyclic Deformation Behavior of B2 Aluminides" Ph.D. thesis, Univ. of Michigan, 106-116, 1991.
40. R.D. Noebe and B.A. Lerch, "Room Temperature Cyclic Deformation Behavior of Cast and Extruded NiAl," *Scripta Metall. Mater.*, **27**, 1161-1166, 1992.

41. B.A. Lerch and R.D. Noebe, "Fatigue Behavior of Polycrystalline NiAl" in *HITEMP Review 1992*, (NASA CP-10104, 1992) 47-1 to 47-15.
42. T.R. Smith, C.G. Kallingal, K. Rajan and N.S. Stoloff, "Strain-controlled Fatigue of NiAl Crystals at Room Temperature," *Scripta Metall. Mater.*, **27**, 1389-1393, 1992.
43. H.L. Fraser, M.H. Loretto, R.E. Smallman and R.J. Wasilewski, "Annealing Point Defects in Quenched NiAl," *Phil. Mag.*, **8s.32**, 873-875, 1975.
44. N. Rusović and E.-Th. Henig, "Influence of Supersaturated Thermal Vacancies on the Elastic Constants of β_2 -NiAl," *Phys. Stat. Sol.*, **57A**, 529-540, 1980.
45. W.G. Johnston and J.J. Gilman, "Dislocation Multiplication in Lithium Fluoride Crystals," *J. Appl. Phys.*, **31**(4), 632-634, 1960.
46. A.S. Tetelman, "Dislocation Dipole Formation in Deformed Crystals," *Acta Metall.*, **10**, 813-820, 1962.
47. R.E. Tressler, J.R. Hellmann and H.T. Hahn, "Advanced High Temperature Composite Materials for Engine Applications," annual report for contract NAGW-1381, Center for Advanced Materials, The Pennsylvania State University, University Park, PA, 63-65, 1990.
48. N. Rusović and H. Warlimont, "The Elastic Behavior of β_2 -NiAl Alloys," *Phys. Stat. Sol.*, **44a**, 609-619, 1977.

TABLES

Table 3.1 - Composition (atomic percent)

| Ni* | Al* | C | O ₂ | S | N ₂ |
|-------|-------|-------|----------------|--------|----------------|
| 50.48 | 49.46 | 0.014 | 0.02 | <0.003 | <0.001 |

*determined by wet chemical analysis, ± 0.2 atomic percent within a 95% confidence interval

Table 4.1 - Comparison of properties from both specimen geometries tested in monotonic tension at 600 K and $\dot{\epsilon} = 10^{-4} \text{ s}^{-1}$.

| specimen geometry | yield strength (MPa) | fracture strength (MPa) | plastic strain to failure |
|-------------------|----------------------|-------------------------|---------------------------|
| tensile | 148 | 246 | 0.018 |
| fatigue | 145 | 250 | 0.019 |

Table 4.2 - Tensile test data used for simplistic predictions of fatigue response. Since necking did not occur at these temperatures, the fracture strength was taken to be the ultimate strength. Monotonic strain hardening exponent, n , was the slope of $\log \sigma$ versus $\log \epsilon_p$.

| test temperature | σ_f (MPa) | ϵ_f | n |
|------------------|------------------|--------------|------|
| 600 K | 246.2 | 0.018 | 0.23 |
| 700 K | 373.3 | 0.182 | 0.22 |

FIGURES

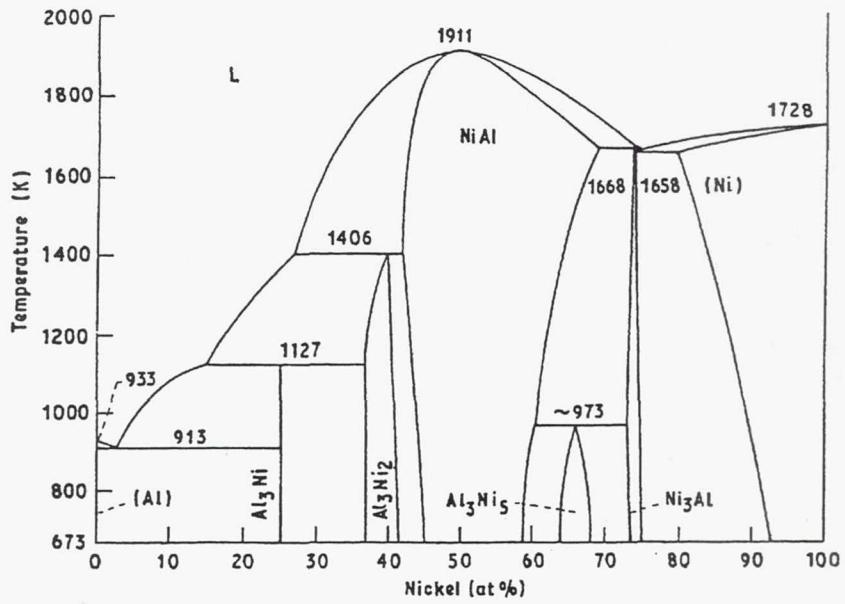


Figure 2.1 - Phase diagram for nickel and aluminum [5].

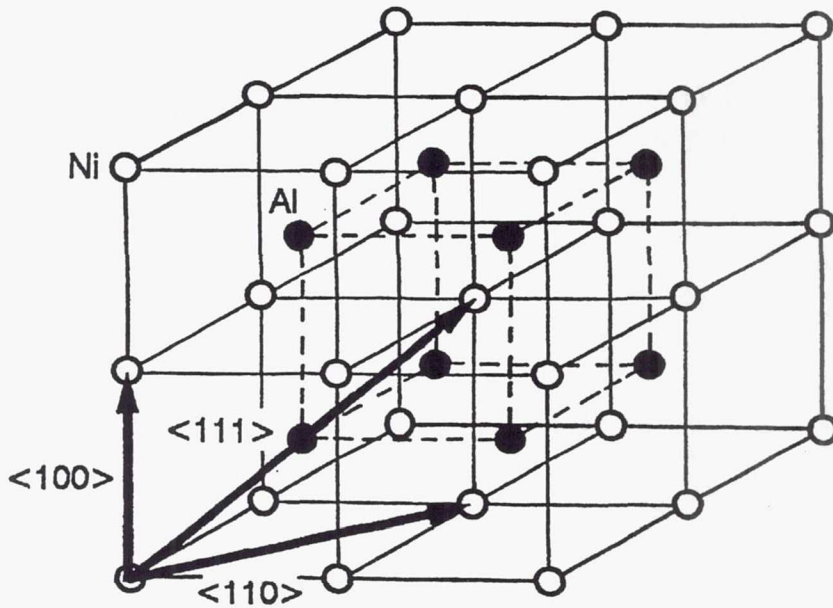
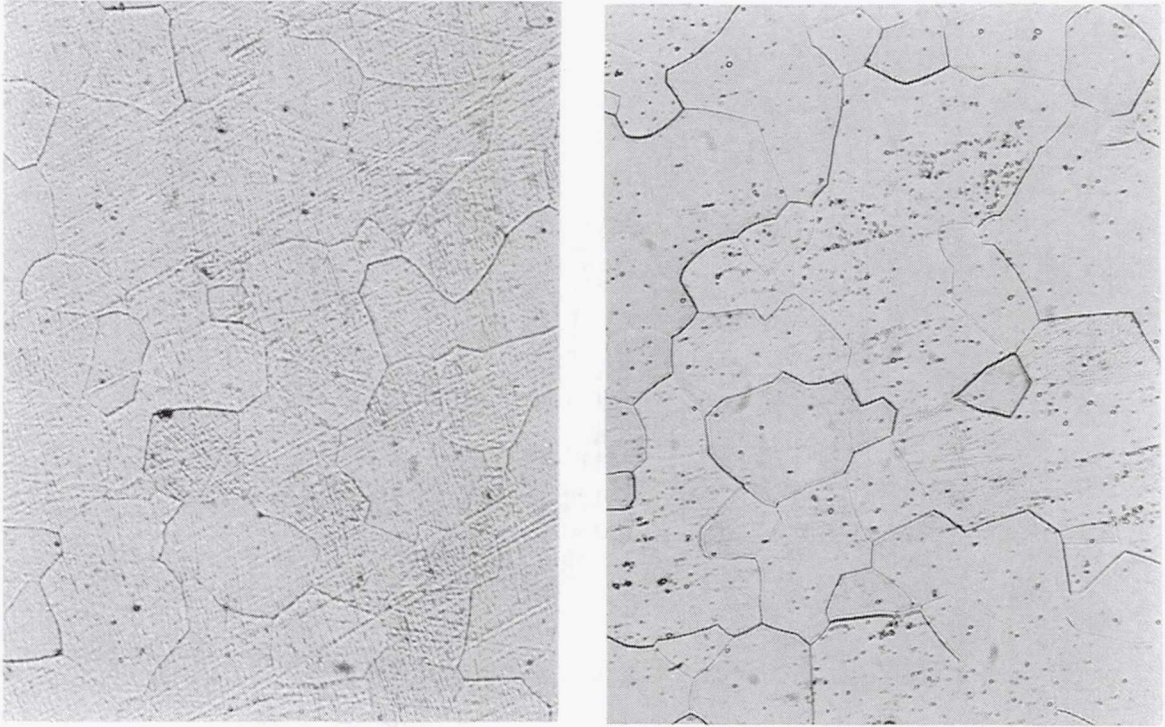


Figure 2.2 - Schematic of B2 crystal structure.



(a) 0.1 mm _____ (b)

Figure 3.1 - Recrystallized, equiaxed structure of NiAl in (a) transverse and (b) longitudinal directions. Average linear intercept grain size is $39 \mu\text{m}$.

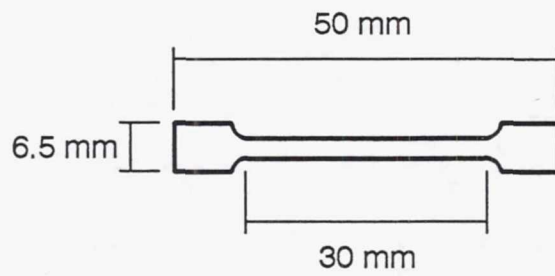


Figure 3.2 - Specifications for tensile specimen drawn to scale. Diameter of gage is 3 mm.

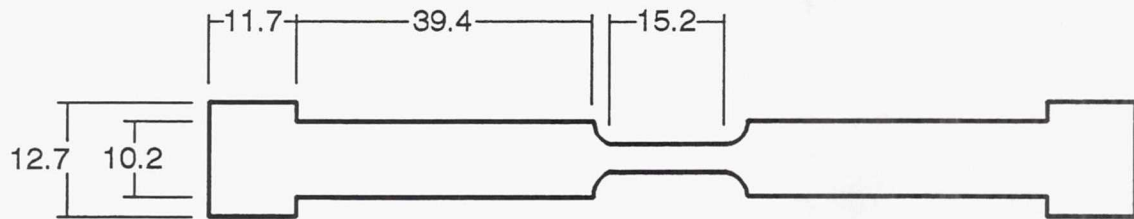


Figure 3.3 - Specifications for low cycle fatigue specimen. The units in the drawing are millimeters and the diameter of the gage is 4 mm.

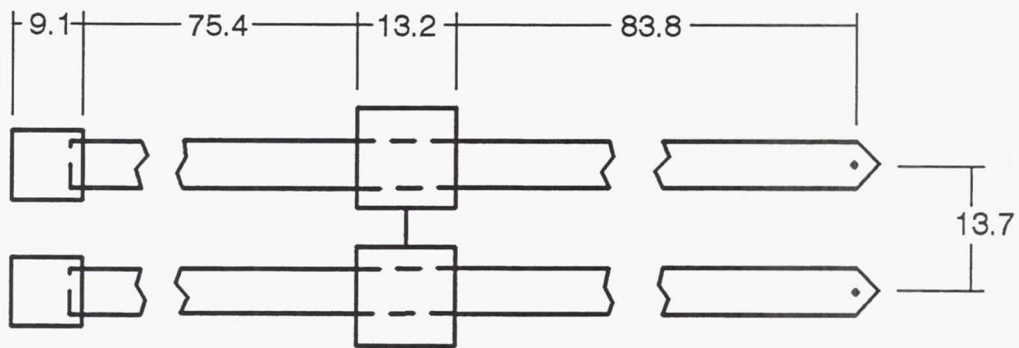


Figure 3.4 - Schematic of blade extensions which attached to a standard 12.7 mm MTS extensometer. Units are millimeters. Alumina rods, 6.35 mm diameter, are spaced by aluminum blocks connected by a semi-flexible piece of shim-stock. The aluminum blocks, left side of schematic, are held to the MTS extensometer blades with small springs.

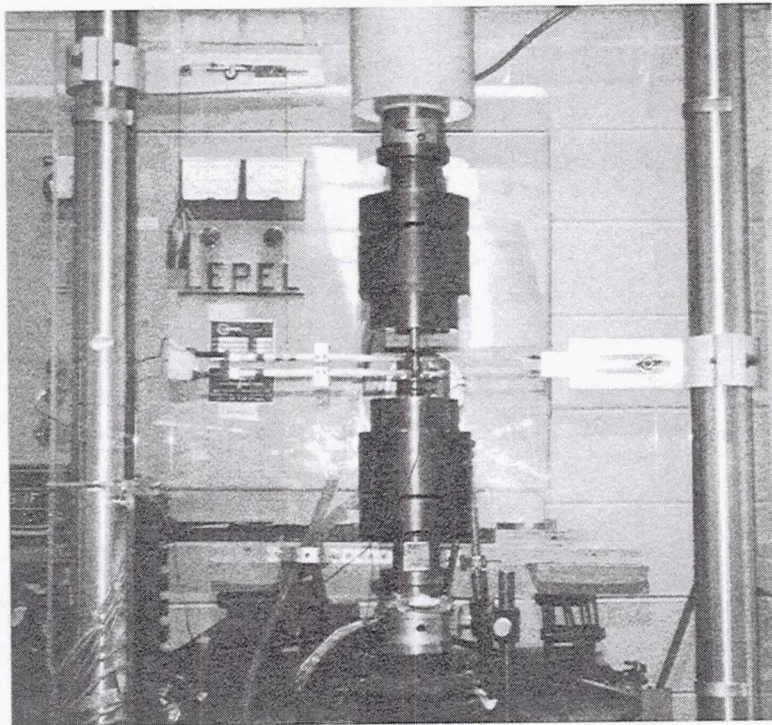


Figure 3.5 - Photograph of low cycle fatigue test set-up with high temperature extensometer in place. Spring tension holds the alumina blades to the sample and the weight of the expanded extensometer is counter-balanced from the top.

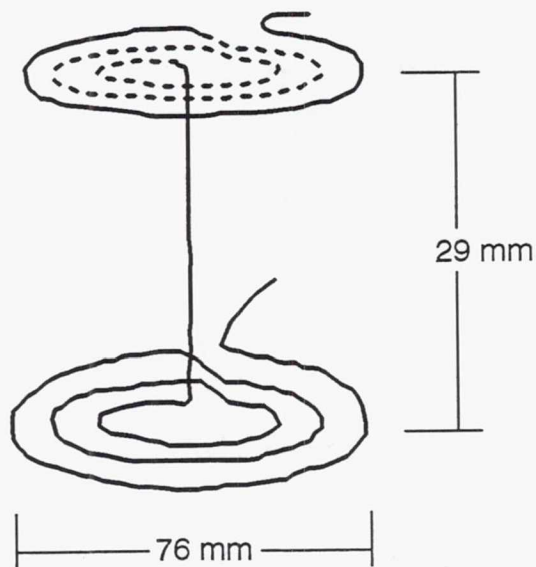


Figure 3.6 - Schematic of induction coil design not drawn to scale.

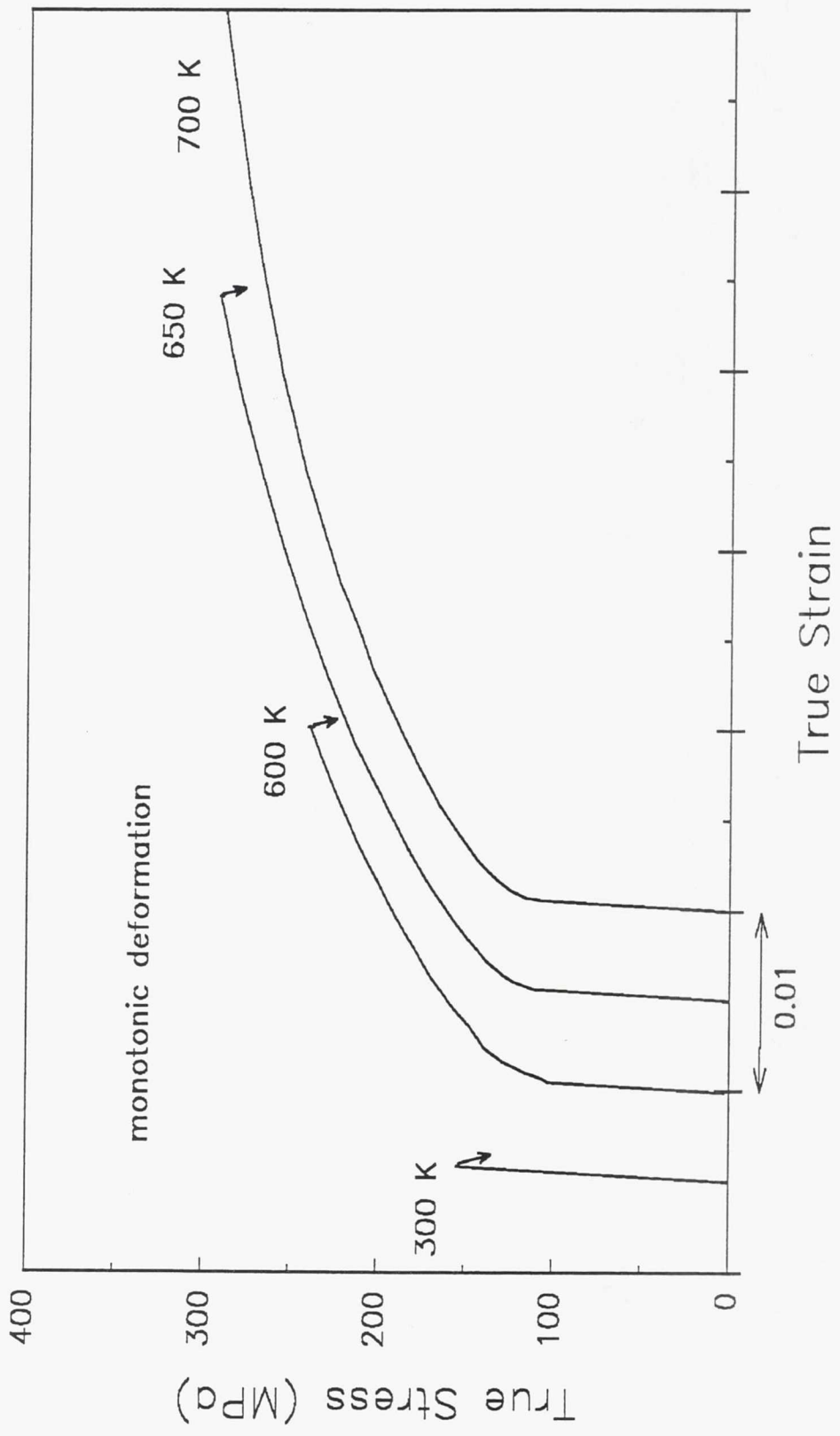


Figure 4.1 - True stress versus true strain for monotonic tensile tests conducted at $\dot{\epsilon} = 10^{-4} \text{ s}^{-1}$. Curves were shifted to the right for clarity. Test at 700 K continued to 18.2%.

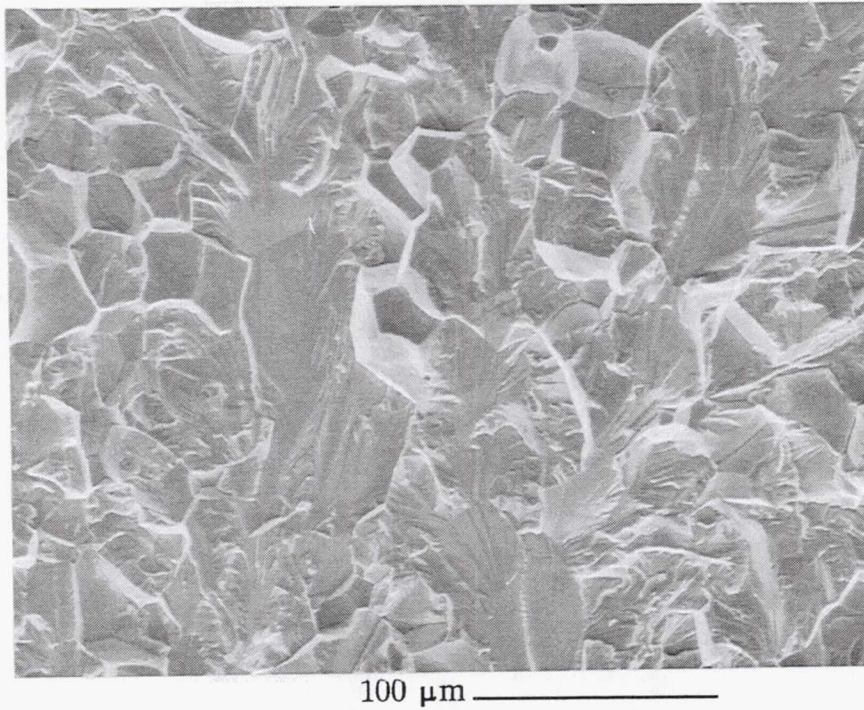


Figure 4.2 - Tensile fracture surfaces at 700 K showing 28% intergranular fracture. Initiation sites were not identified but occurred within the gage section.

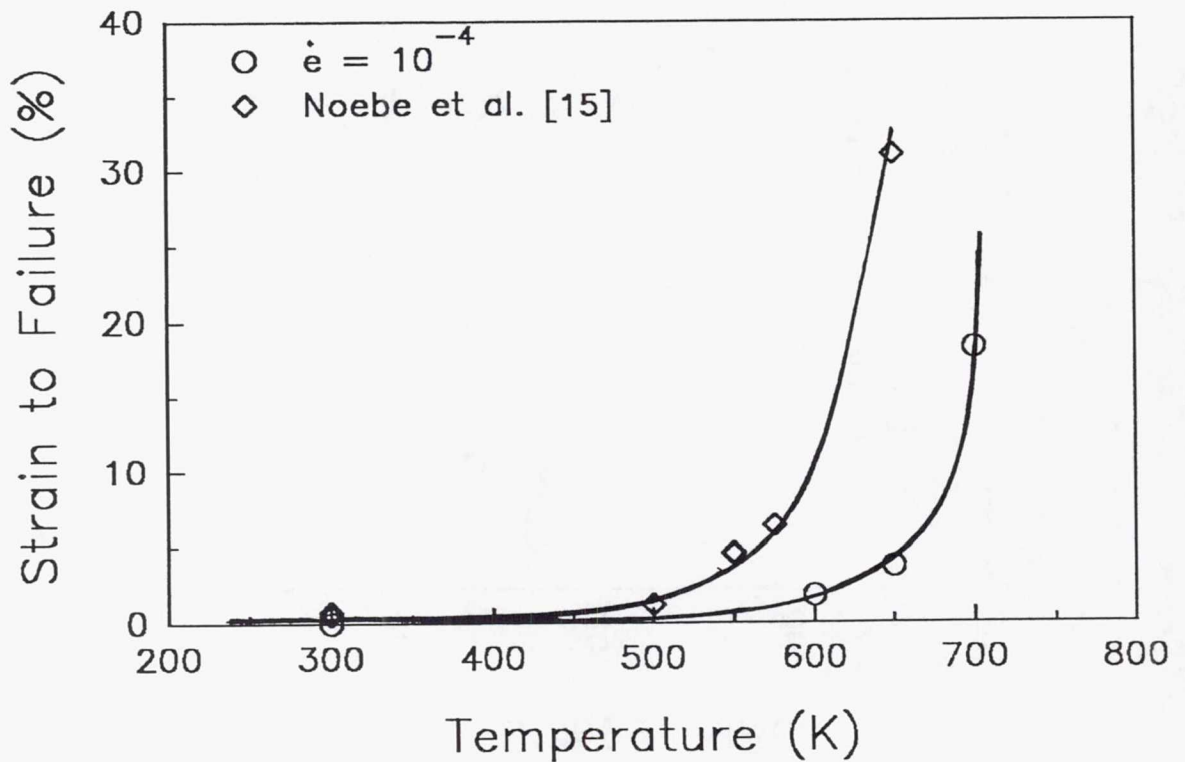


Figure 4.3 - True strain to failure as a function of temperature for tensile specimens from this study and reported by Noebe, et al. at $\dot{\epsilon} = 10^{-4}$.

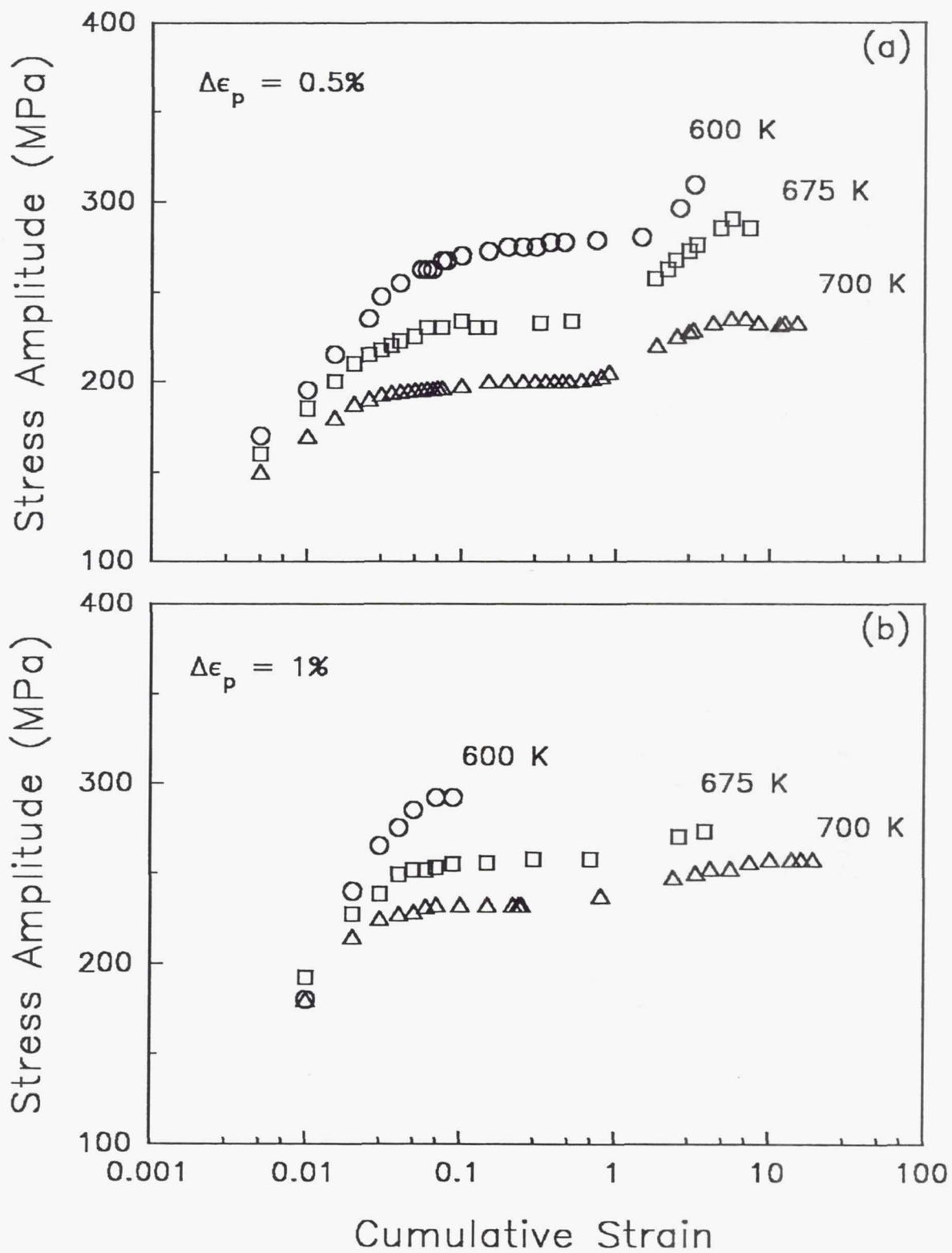


Figure 4.4 - Stress amplitude versus cumulative plastic strain for all three temperatures at $\dot{\epsilon} = 10^{-4} \text{ s}^{-1}$ (a) $\Delta\epsilon_p = 0.5\%$ and (b) $\Delta\epsilon_p = 1.0\%$.

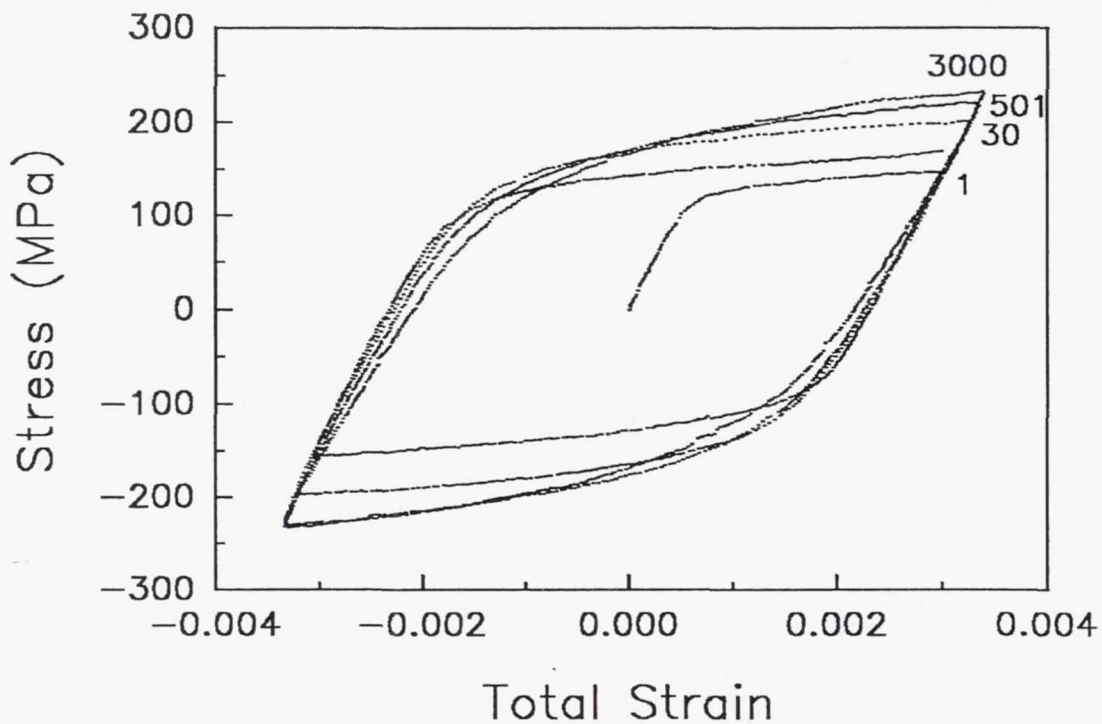


Figure 4.5 - Digitized points from hysteresis loops taken during a test at 700 K, $\Delta\epsilon_p = 0.5\%$.

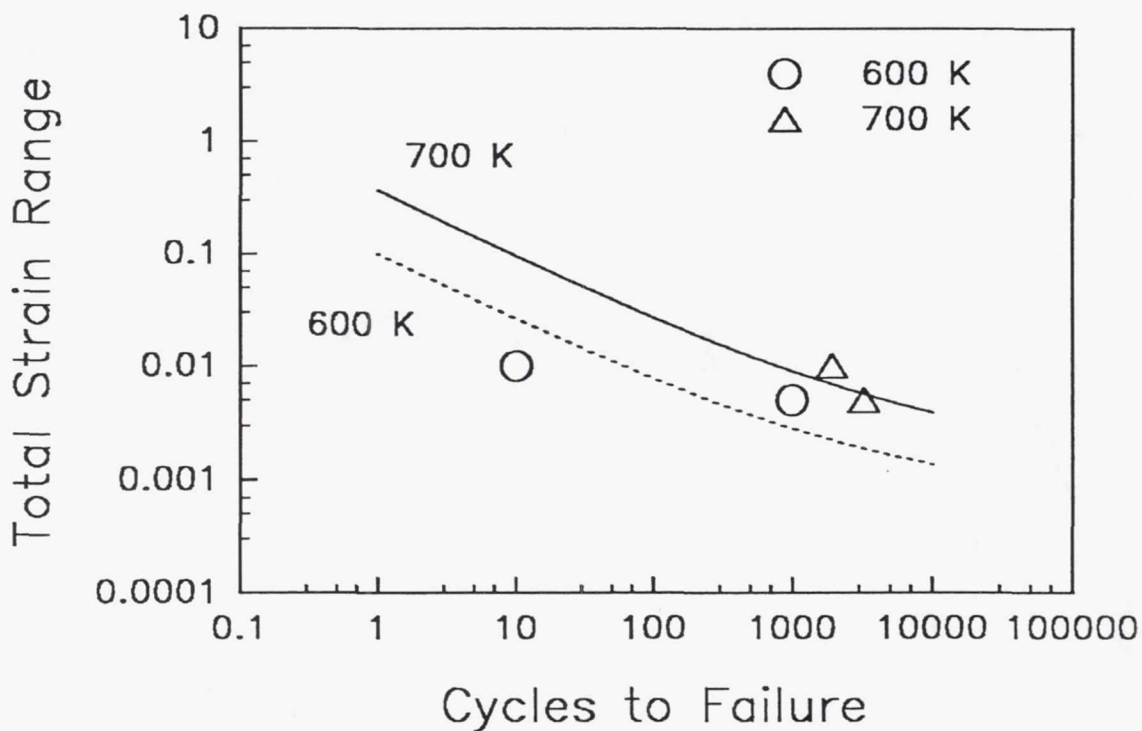


Figure 4.6 - Lines represent estimated fatigue lives using the universal slopes equation. Data points are total strain range at time of failure from this study.

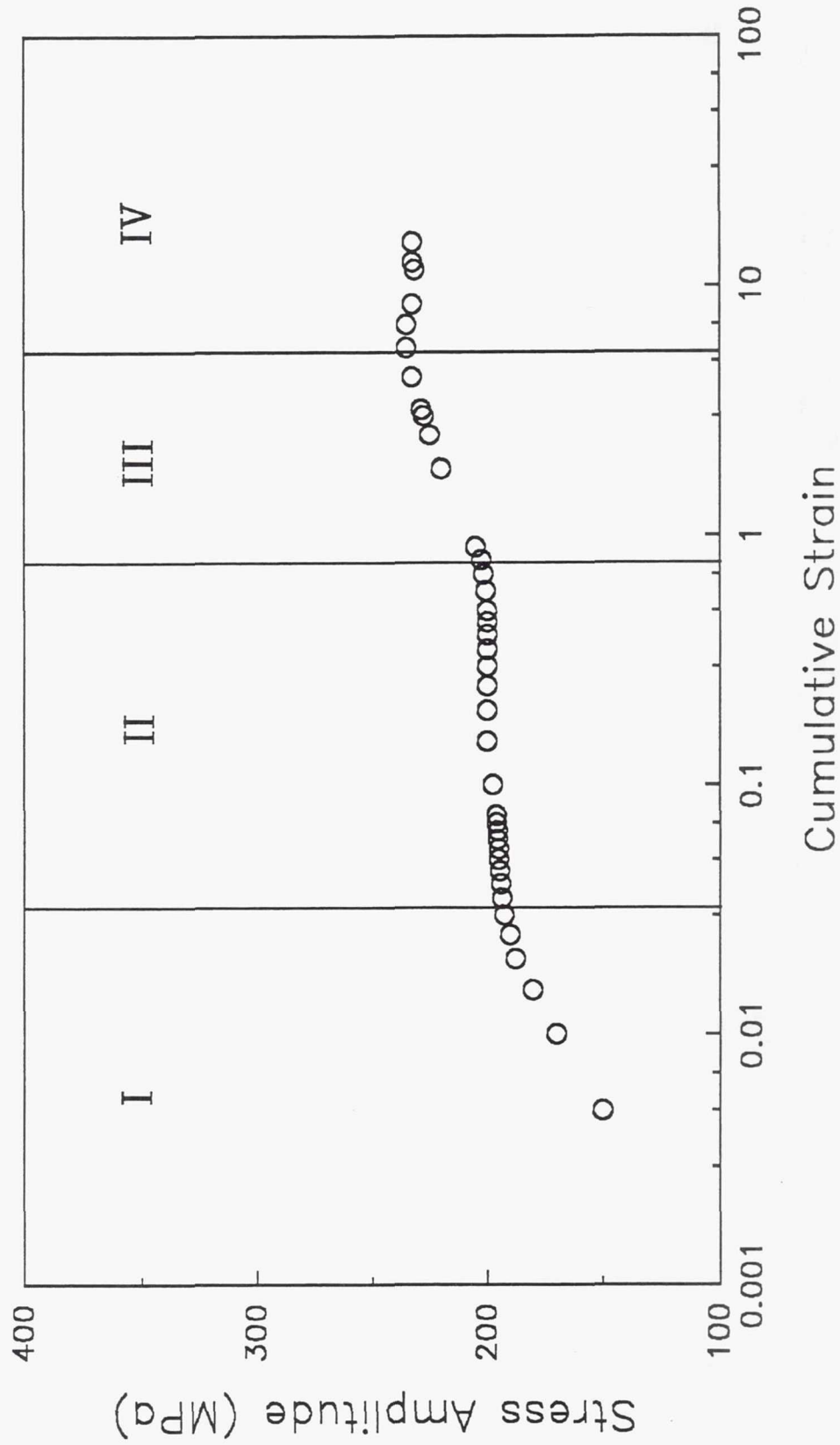


Figure 4.7 - Stress amplitude versus cumulative strain for sample tested at 700 K, $\Delta\epsilon_p = 0.5\%$. Regions I-IV indicate areas of rapid cyclic hardening, a stress plateau, additional hardening, and returning to relative stability.

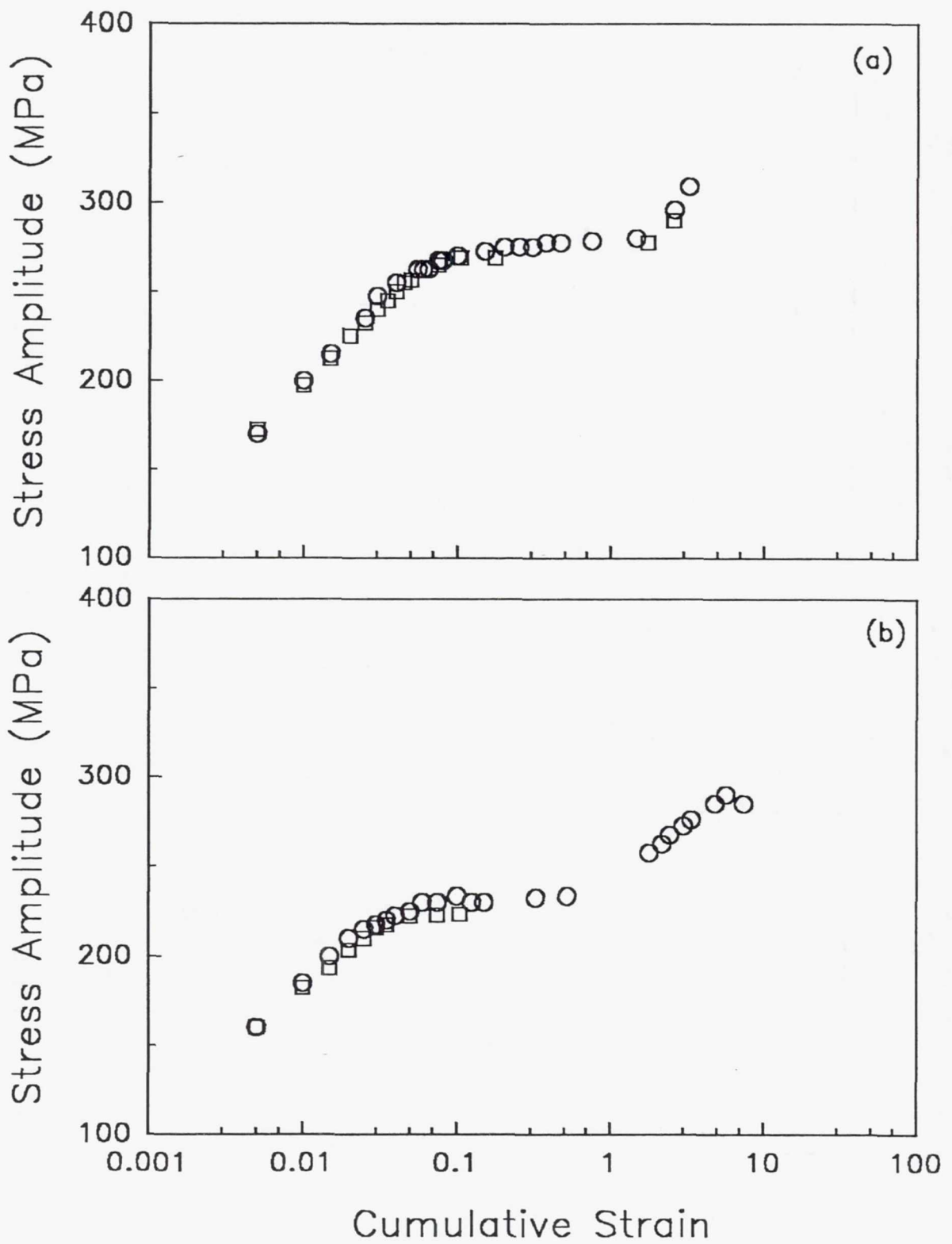


Figure 4.8 - (a) Duplicate LCF tests conducted at 600 K, $\Delta\epsilon_p = 0.5\%$.
 (b) Interrupted tests conducted at 675 K, $\Delta\epsilon_p = 1.0\%$.

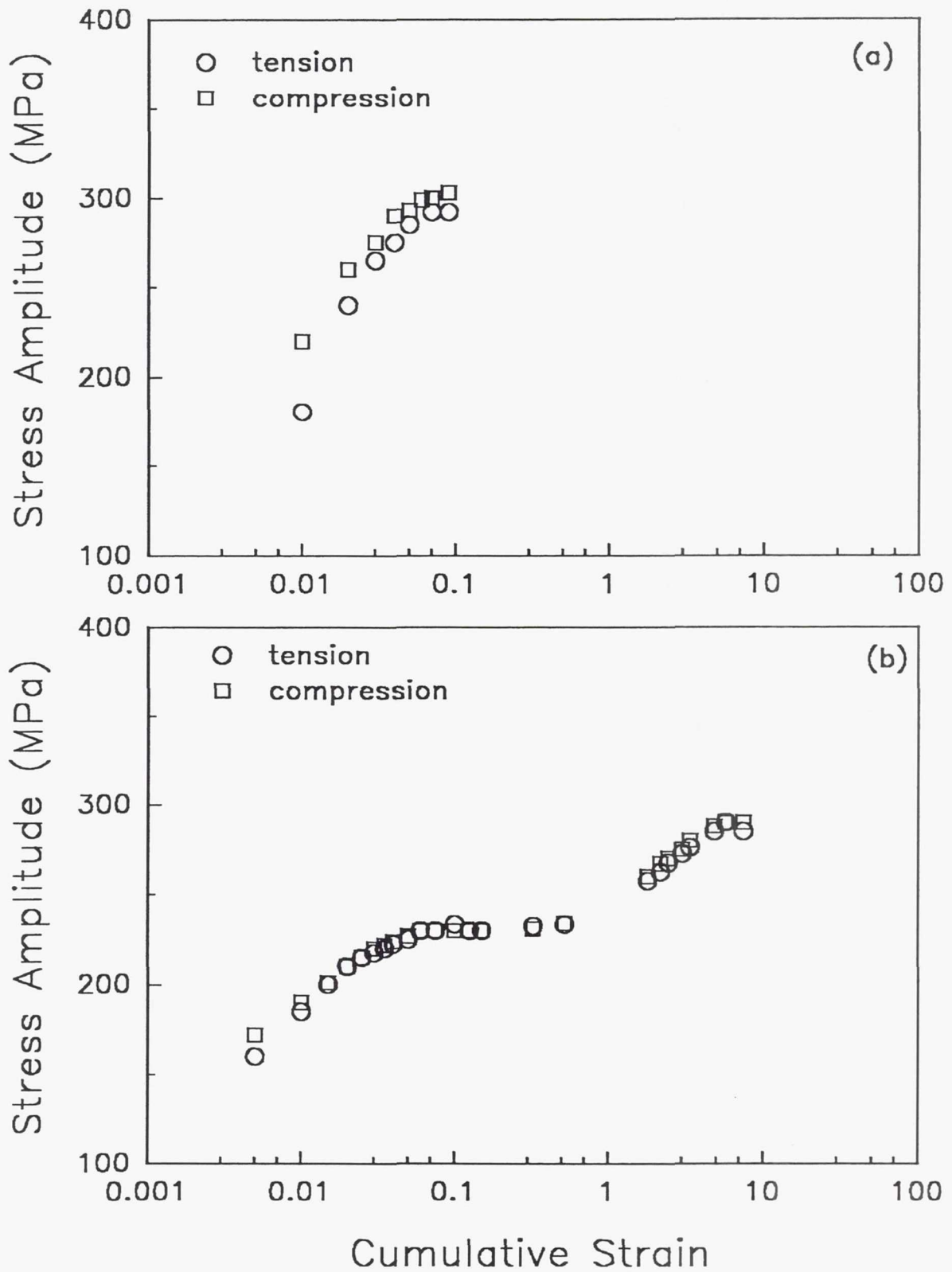
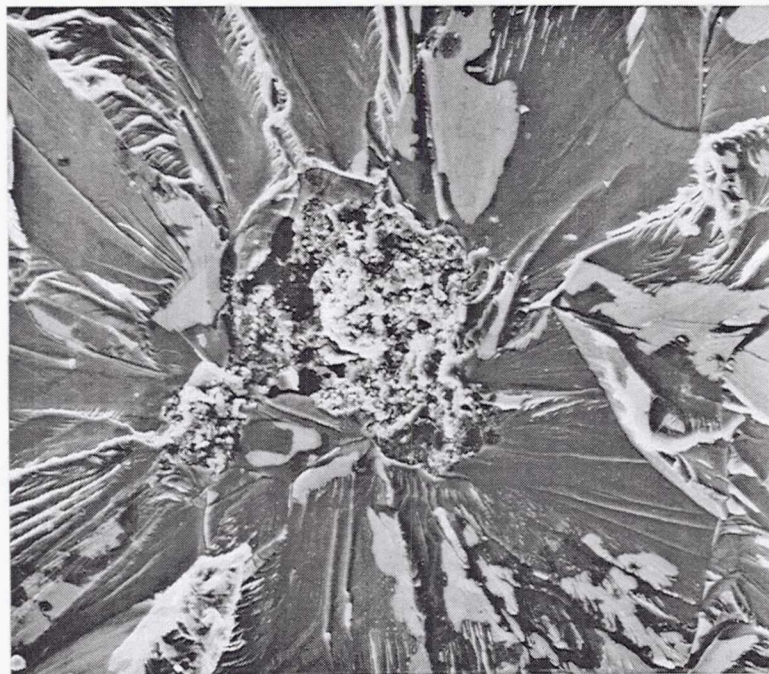


Figure 4.9 - Tensile and compressive stress amplitude versus cumulative plastic strain for $\Delta\epsilon_p = 1.0\%$, $\dot{\epsilon} = 10^{-4} \text{ s}^{-1}$, (a) 600 K and (b) 700 K.

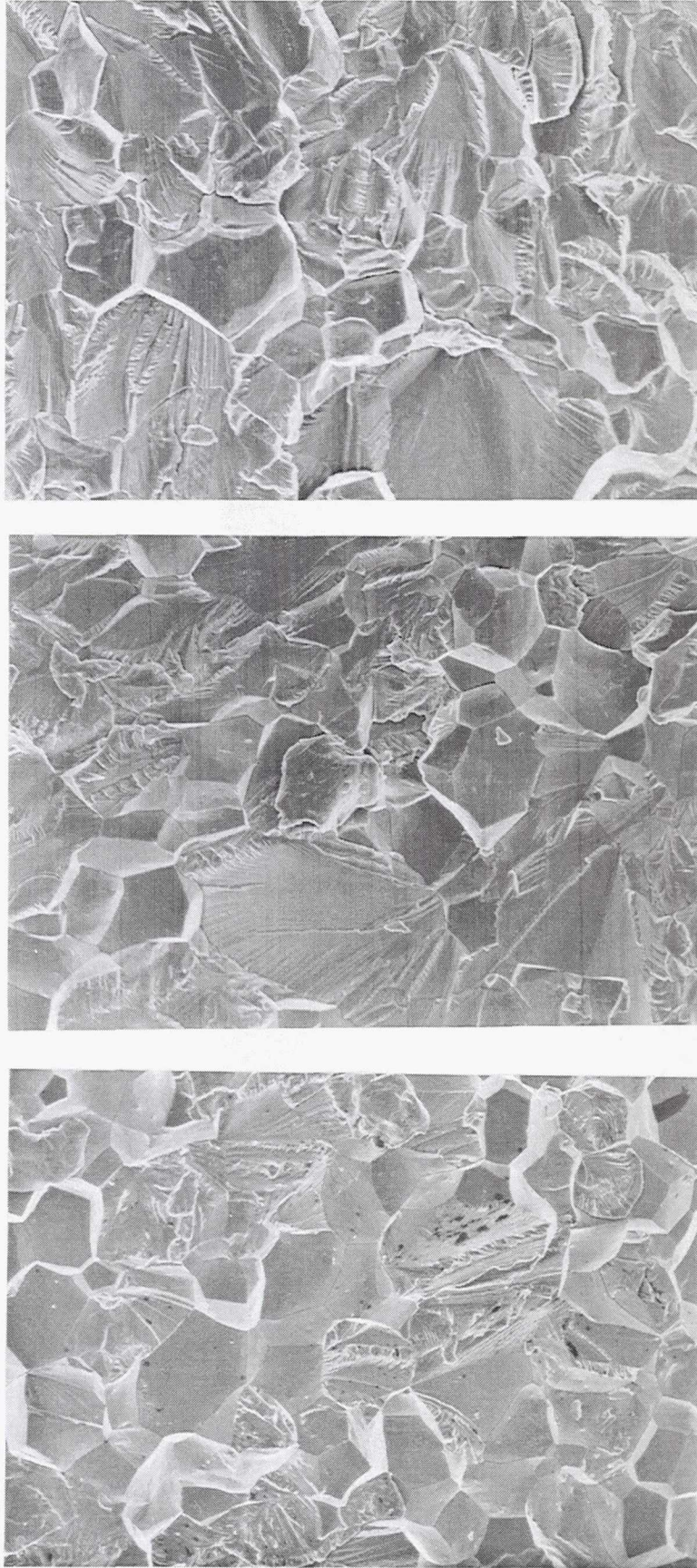


(a) 1 mm _____



(b) 10 μm _____

Figure 4.10 - Fracture surface of sample tested at 700 K, $\Delta\epsilon_p = 0.01$ (a) low magnification with inclusion at upper left (b) inclusion. EDX analysis showed high amounts of Al, measurable amounts of Si and virtually no Ni present in the inclusion.



(a)

(b)

(c)

100 μm

Figure 4.11 - Portion of the fracture surfaces at (a) 600 K (b) 675 K and (c) 700 K showing, respectively, 47%, 32%, and 33% intergranular fracture.



(a) 100 μm ———



(b) 10 μm ———

Figure 4.12 - Gage surface of sample tested to failure (region IV) at 700 K, $\Delta\epsilon_p = 0.5\%$ showing (a) extensive slip traces and (b) distinct extrusions and fine slip lines.



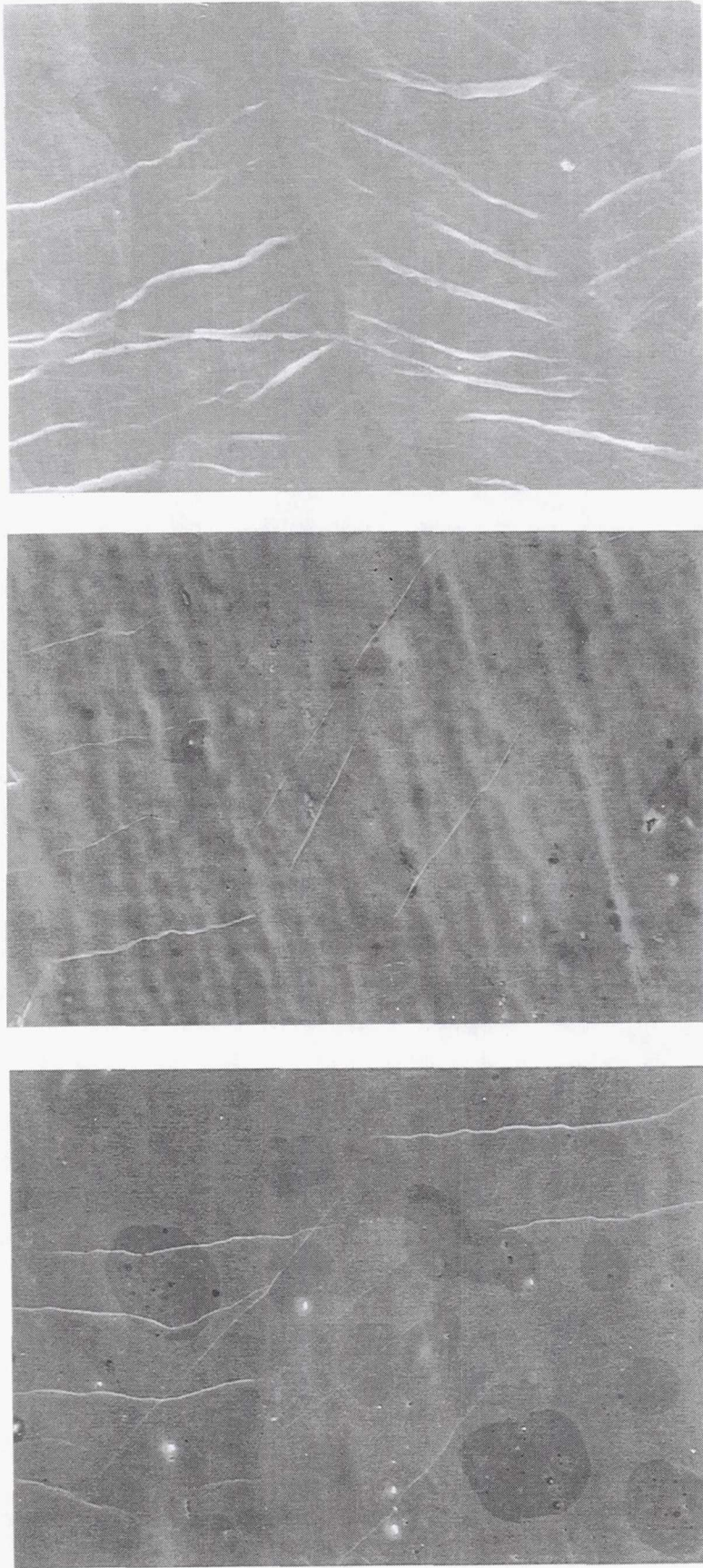
(a)

100 μm



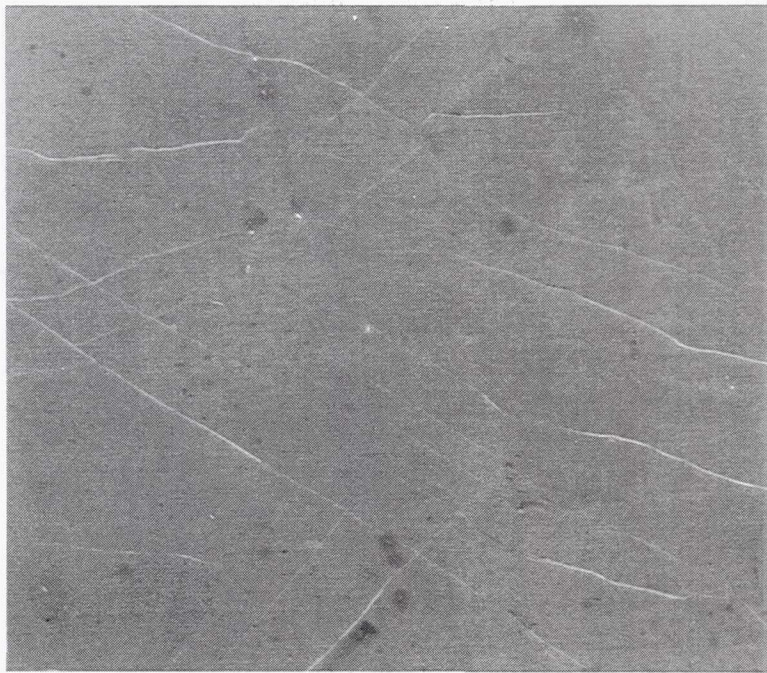
(b)

Figure 4.13 - Gage surface of sample tested to failure at 600 K, $\Delta\epsilon_p = 1.0\%$ showing regions of slip traces (a) near the fracture surface and (b) near the radius



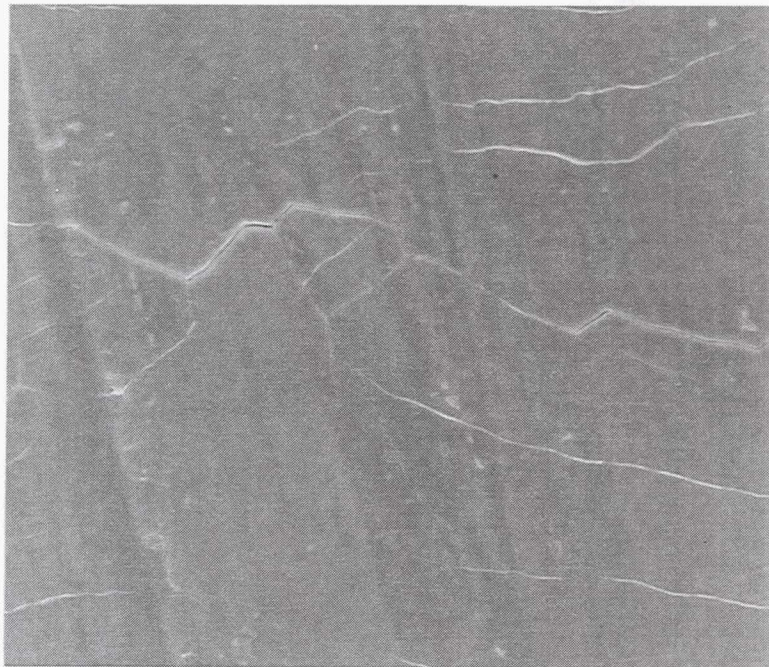
(a) (b) (c)

Figure 4.14 - Specimens deformed at 600 K and $\Delta\epsilon_p = 0.005$ (a) interrupted in region I, i.e. while cyclicly hardening, (b) interrupted in the beginning of region II, i.e. at the onset of stability, (c) failed in region III.



(a)

50 μm —————



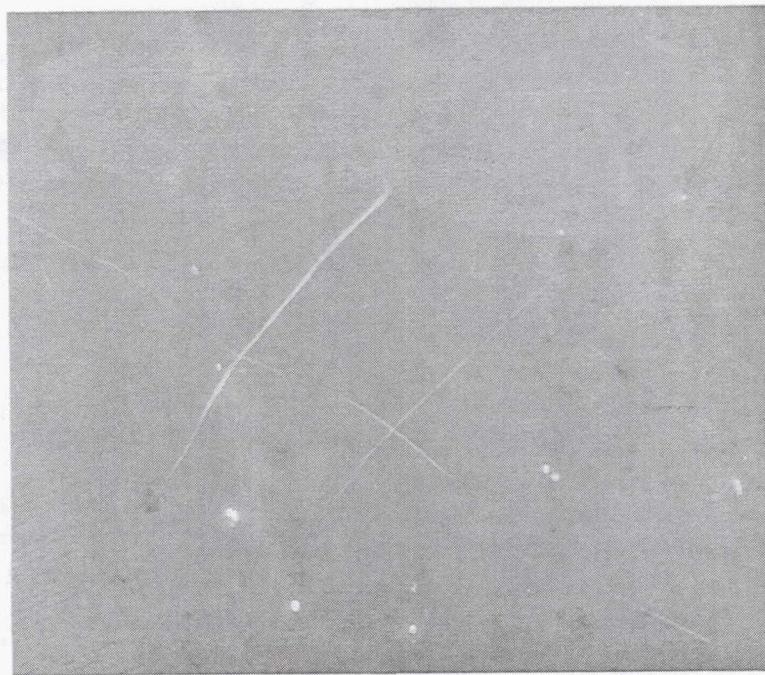
(b)

Figure 4.15 - Specimens deformed at 600 K and $\Delta\epsilon_p = 1.0\%$ both failed at the beginning of region II as the result of internal inclusions (a) $N_f = 8$ and (b) $N_f = 10$.



25 μm _____

Figure 4.16 - Specimens deformed $\Delta\epsilon_p = 0.5\%$ and interrupted at the beginning of region II, 700 K. Compare to 14(b).



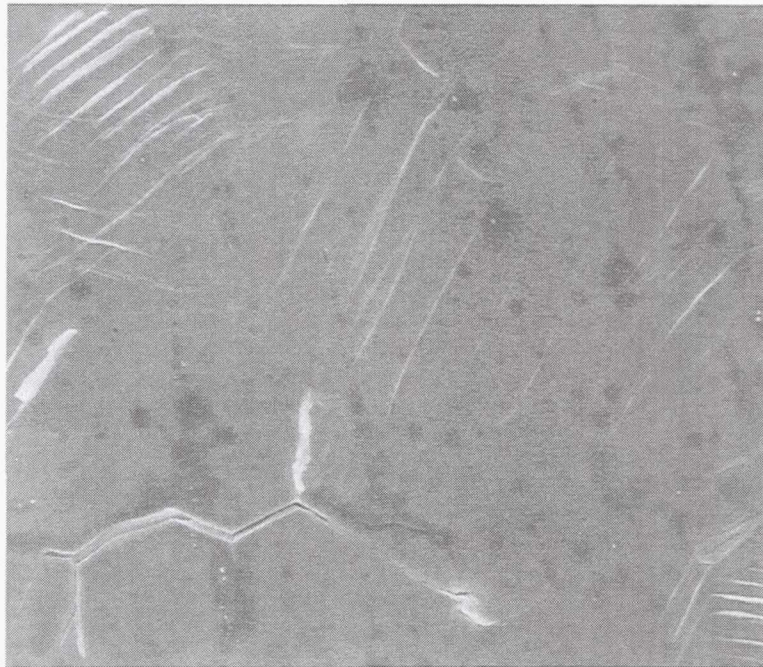
25 μm _____

Figure 4.17 - Specimen deformed at 700 K and $\Delta\epsilon_p = 1.0\%$ compare to 4.15(a,b) above.



(a)

50 μm _____



(b)

Figure 4.18 - Specimens deformed $\Delta\epsilon_p = 1.0\%$ (a) 675 K and (b) 700 K. Both failed in region III as the result of inclusions. The intrusions/extrusions were more developed in (a) as the result of the lower test temperature even though specimen (a) failed 100 cycles before specimen (b).



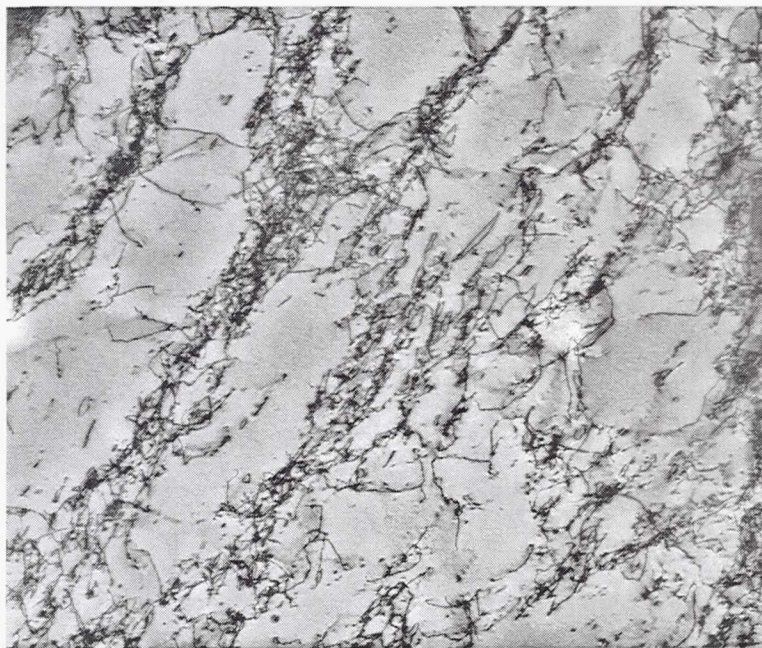
1 μm _____

Figure 4.19 - Cellular dislocation structure beginning to form after one fully reversed cycle at 600 K and $\Delta\epsilon_p = 0.5\%$.



(a)

1 μm _____



(b)

Figure 4.20 - Well developed cells with thick walls of dislocations after 5 cycles at 600 K and $\Delta\epsilon_p = 0.5\%$ with (a) equiax and (b) slightly elongated configurations.

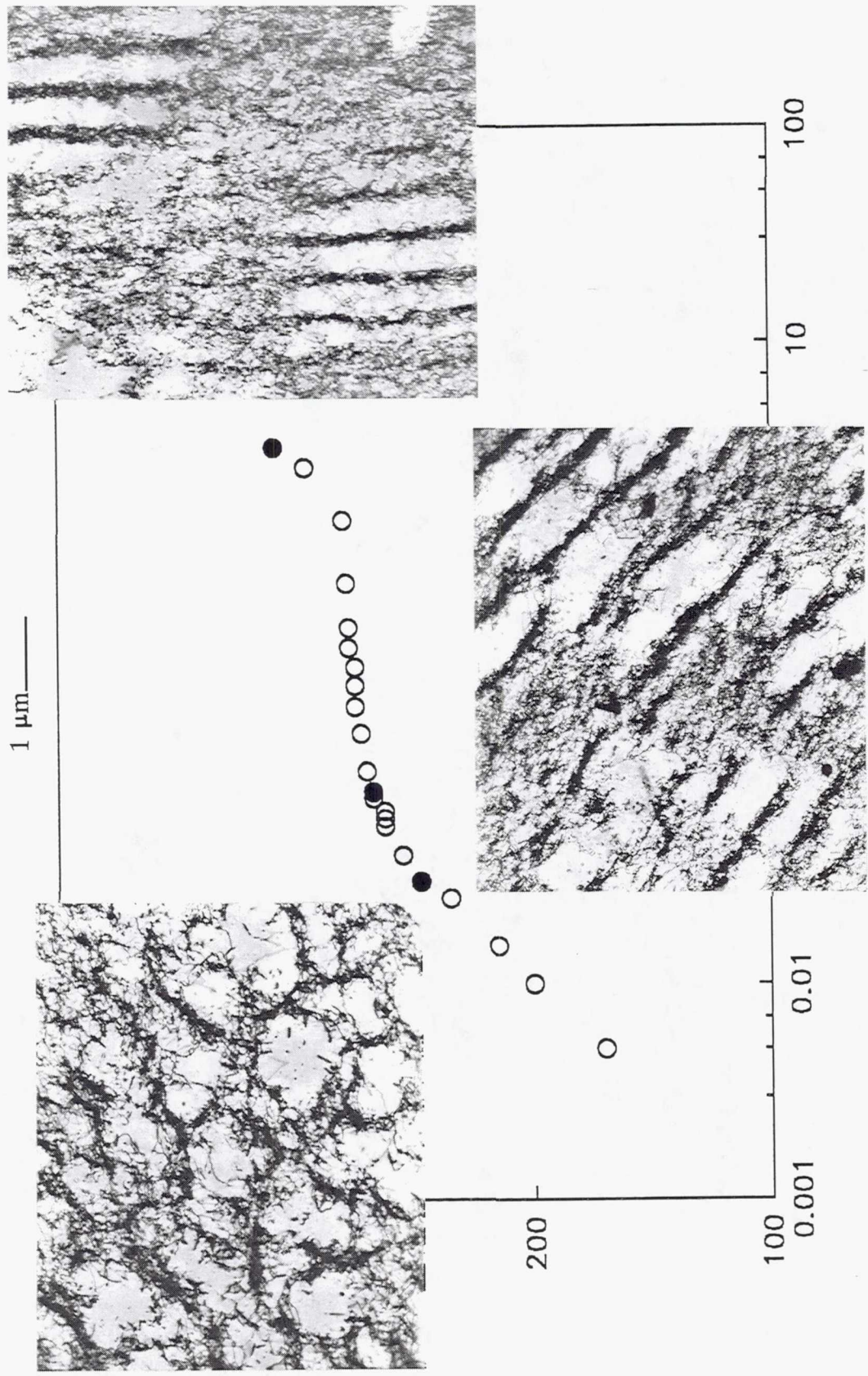


Figure 4.21 - Cyclic hardening curve of sample tested to failure at 600 K and $\Delta\epsilon_p = 0.5\%$ with micrographs of the dislocation structure after (a) 5 cycles, (b) 15 cycles, and (c) failure at 781 cycles.

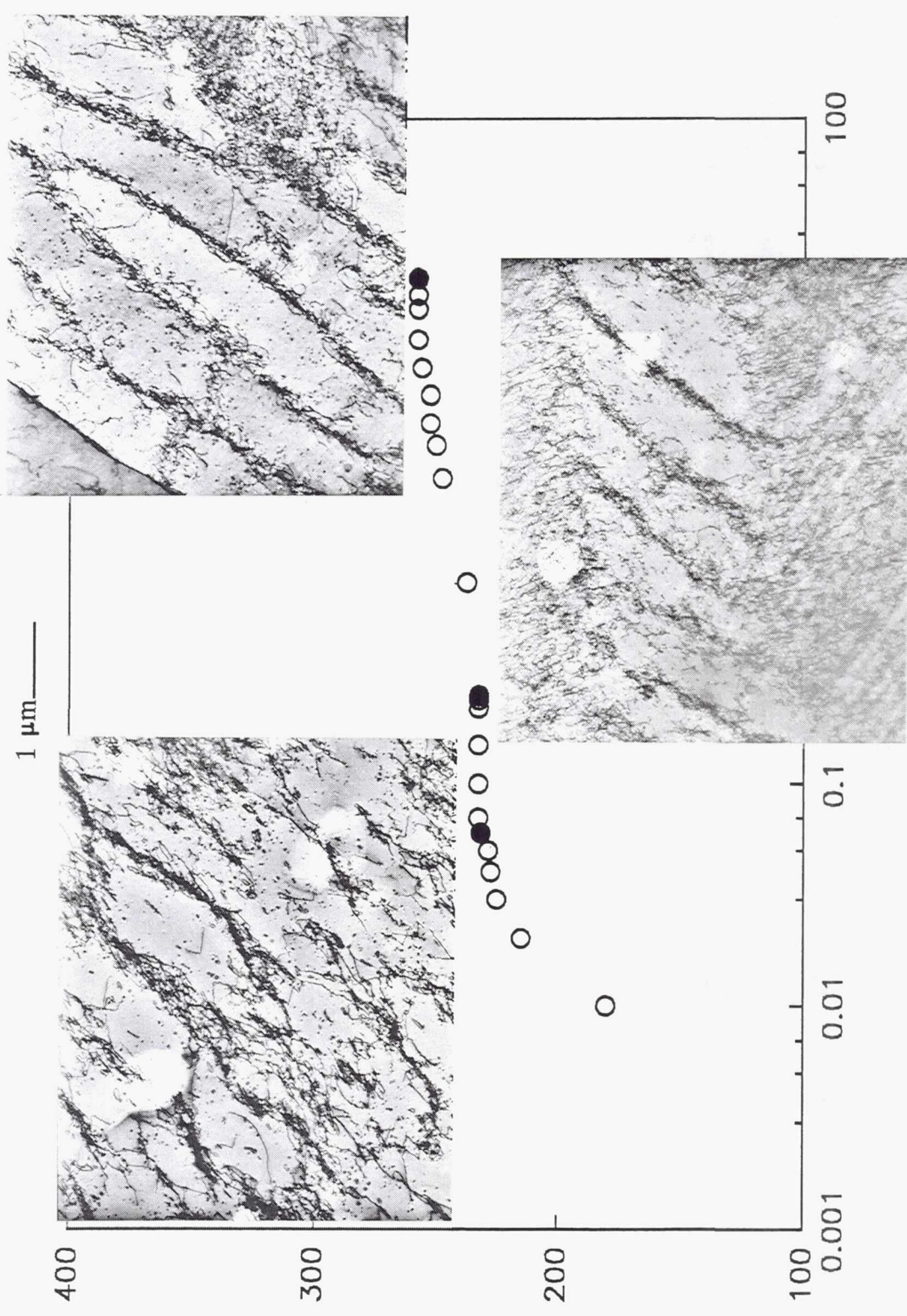


Figure 4.22 - Cyclic hardening curve of sample tested to failure at 700 K and $\Delta\epsilon_p = 1.0\%$ with micrographs of the dislocation structure after (a) 6 cycles, (b) failure at 491 cycles, and (c) failure at 1911 cycles.



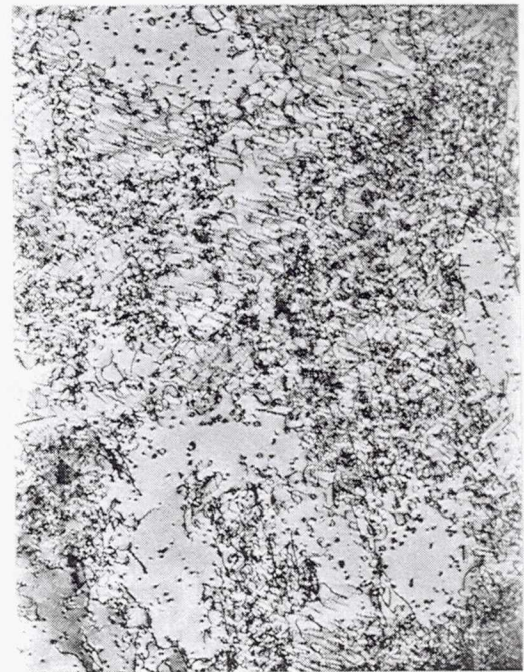
(a)



(b)



(c)



(d)

1 μm ———

Figure 4.23 - Dislocation structures of samples tested to failure at $\Delta\epsilon_p = 0.5\%$ and (a,b) 600 K, region III and (c,d) 700 K, region IV.

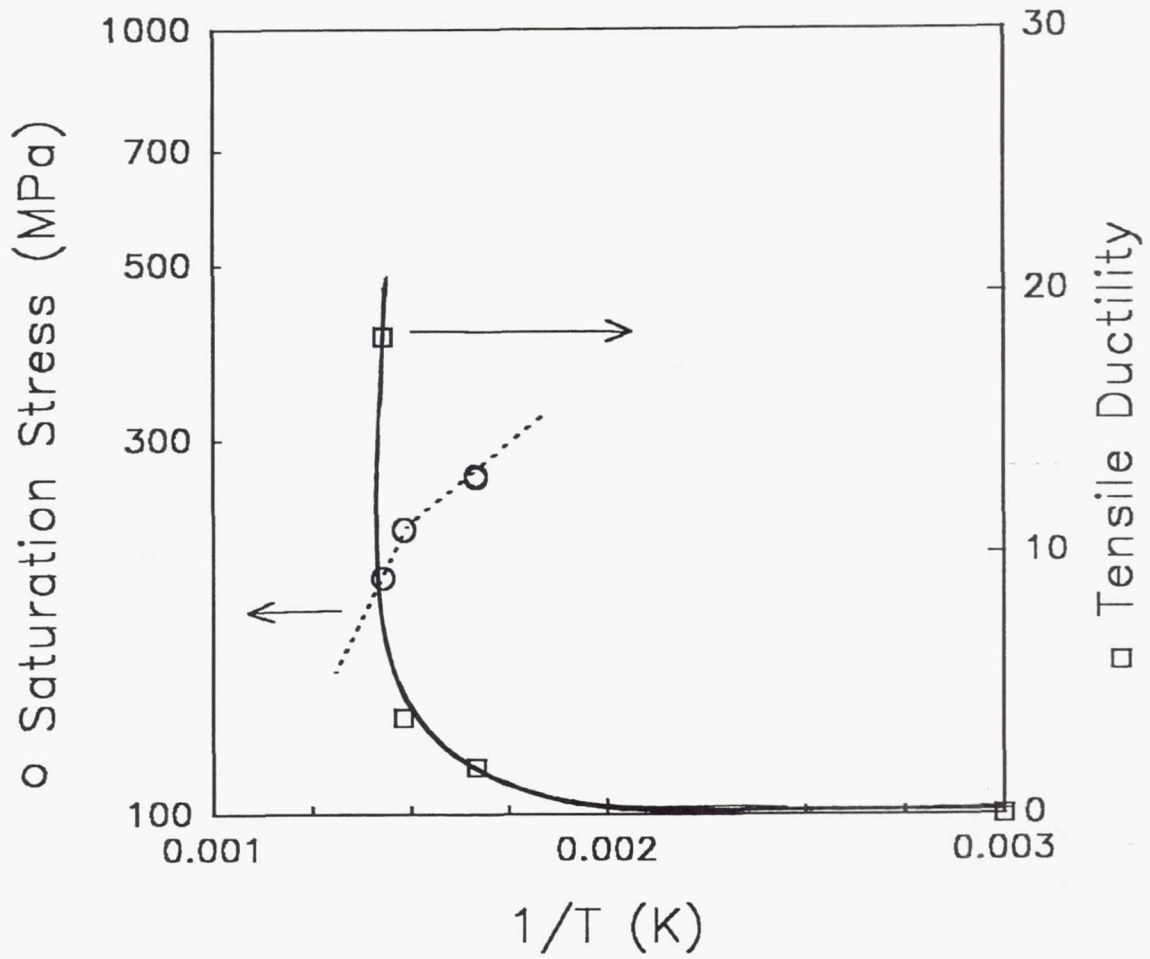
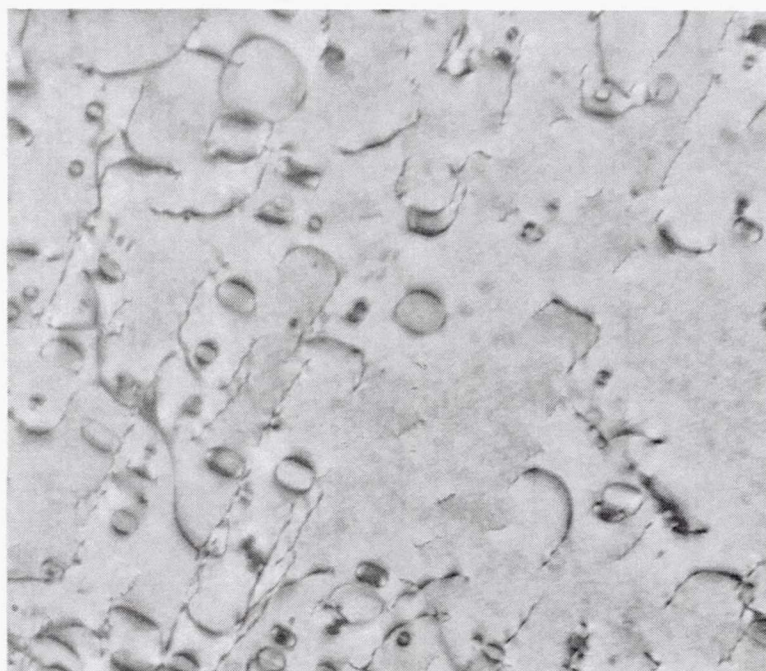


Figure 4.24 - Log saturation (region II) stress and monotonic ductility versus $1/T$ for tests conducted at $\dot{\epsilon} = 10^{-4} \text{ s}^{-1}$ and $\Delta\epsilon_p = 0.5\%$.



0.5 μm _____

Figure 4.25 - Regions of well aligned loops probably created by superjogs on moving dislocations.



1 μm _____

Figure 4.26 - Interior of specimen held at 600 K for time equivalent to testing to failure showing no evidence of dislocation loops.

APPENDIX A

TENSILE DISPLACEMENT ADJUSTMENT

Monotonic tensile tests were conducted using a sample configuration and Instron test frame which had previously given consistent results, e.g. [15]. One limitation with the use of this test frame was the necessity to conduct the tests with constant cross-head displacement. As a result of this control mode, machine stiffness became a factor in specimen measurements. The machine stiffness was subsequently removed from the measured displacements by calculations assuming constant load throughout the test train (or load train).

During the elastic portion of a tensile test, there is a linear relationship that can be expressed either as the familiar elastic modulus, E , or as the spring constant, k , given in formula A-1. The displacements, d , measured during the tensile

$$k = \frac{P}{d} \quad (\text{A-1})$$

tests were a summation of the displacements from the sample and the test frame since a strain-gage extensometer was not used. Because the load, P , is constant at any given point in time across the entire load train, the spring constants of the *total* train, the test *frame*, and the *sample* are related as shown in A-2. Only k_{total} , the spring constant of the *total* train is measured directly from the tensile test.

$$\frac{1}{k_{total}} = \frac{1}{k_{frame}} + \frac{1}{k_{sample}} \quad (A-2)$$

An approximate elastic modulus for the sample was calculated using the formula, A-3, given by Tressler et al. [47] based on the data of Rusović and

$$E = 204.9 - 0.041(T) \quad (A-3)$$

Warlimont [48]. In A-3, E is calculated in GPa and T in degrees Kelvin. This formula does not precisely describe the actual sample modulus because the data of Rusović and Warlimont [48] was generated for cast NiAl with no reported crystallographic texture. Formula A-3 did, however, appear to sufficiently describe the moduli determined on this extruded material when using the LCF test apparatus.

The spring constants, k_{sample} , for samples at each test temperature were determined from the calculated values of the elastic modulus (A-3) by employing the specimen dimensions and the appropriate conversion constant for transforming GPa to kg/mm. The machine stiffness could then be calculated using the measured k_{total} , the calculated k_{sample} and the formula A-2 written as shown in A-4. The displacement

$$k_{frame} = \frac{k_{total} k_{sample}}{k_{sample} - k_{total}} \quad (A-4)$$

due to the test frame could be calculated from k_{frame} using formula A-1 and then subtracted from the total displacement. Thus the displacement of the NiAl during tensile testing could be used in the stress and strain calculations given in Chapter 3.

APPENDIX B

LOW CYCLE FATIGUE DATA

Table BI gives the low cycle fatigue test matrix including the final number of cycles, the region of the cyclic hardening curve in which failure occurred and the type of fracture initiation site for each test specimen. The figures following this table are the cyclic hardening curves for each specimen and are given in the same order as presented in Table BI.

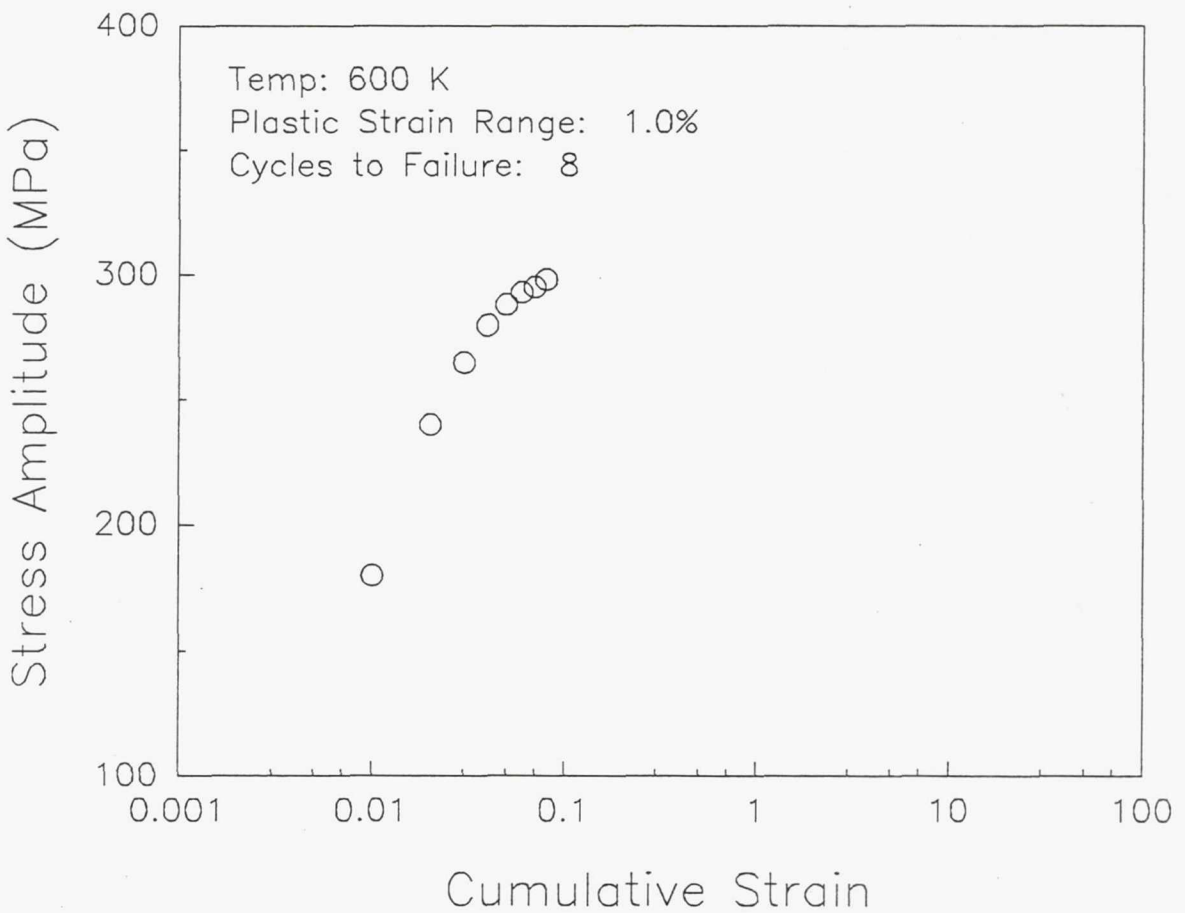
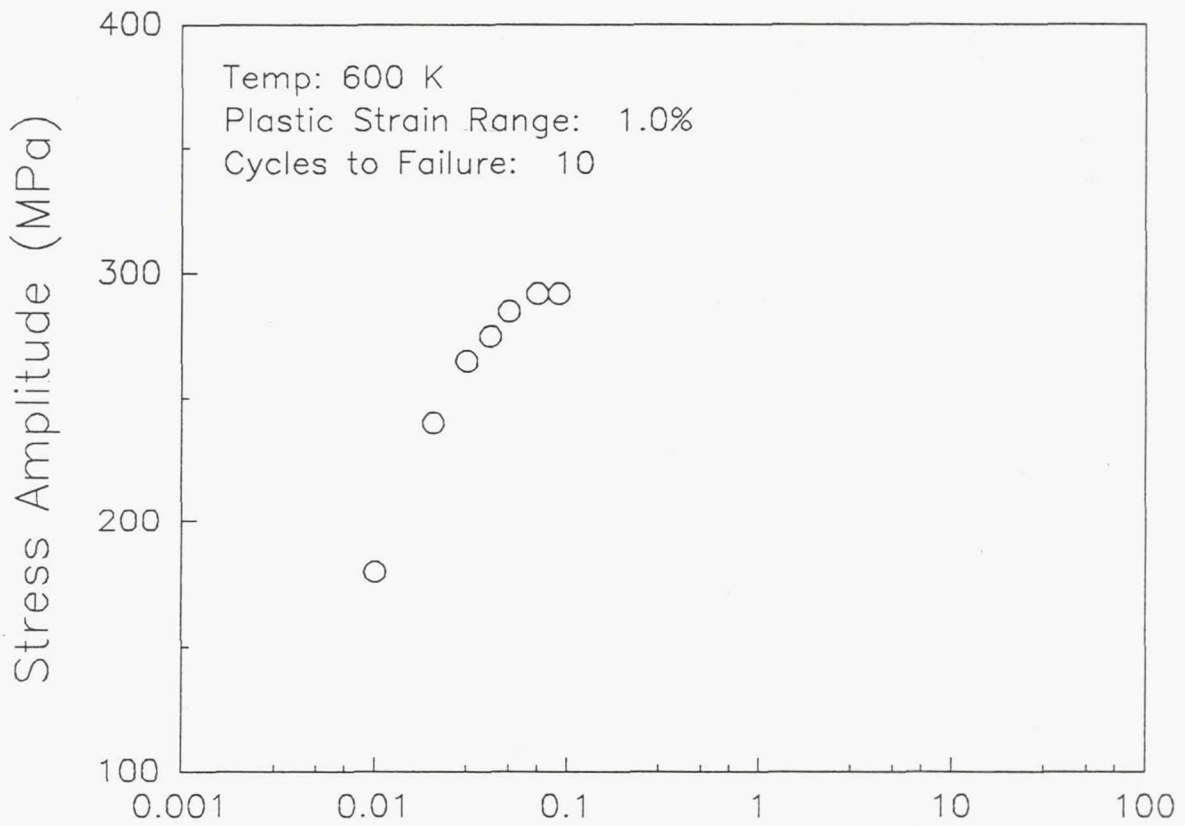
Table BI--Test Matrix

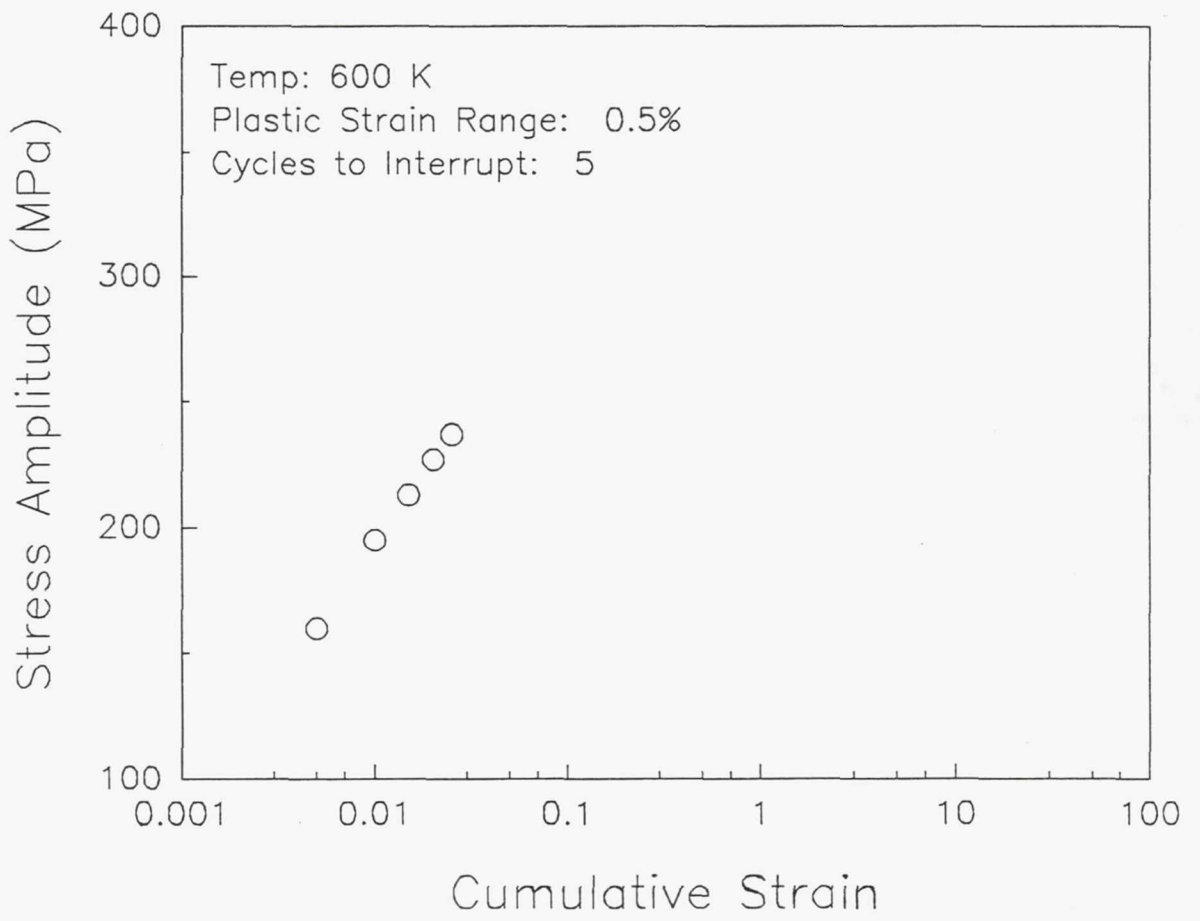
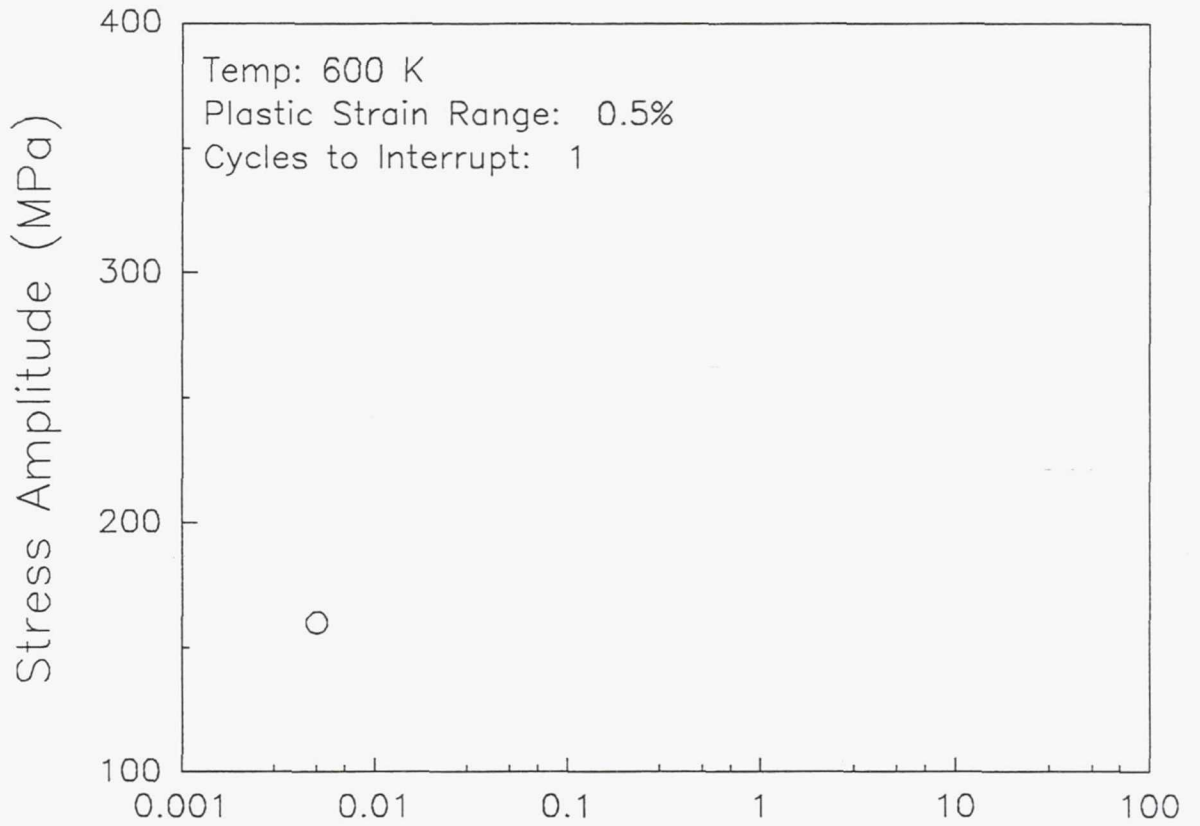
Conducted at $\dot{\epsilon} = 10^{-4} \text{ s}^{-1}$

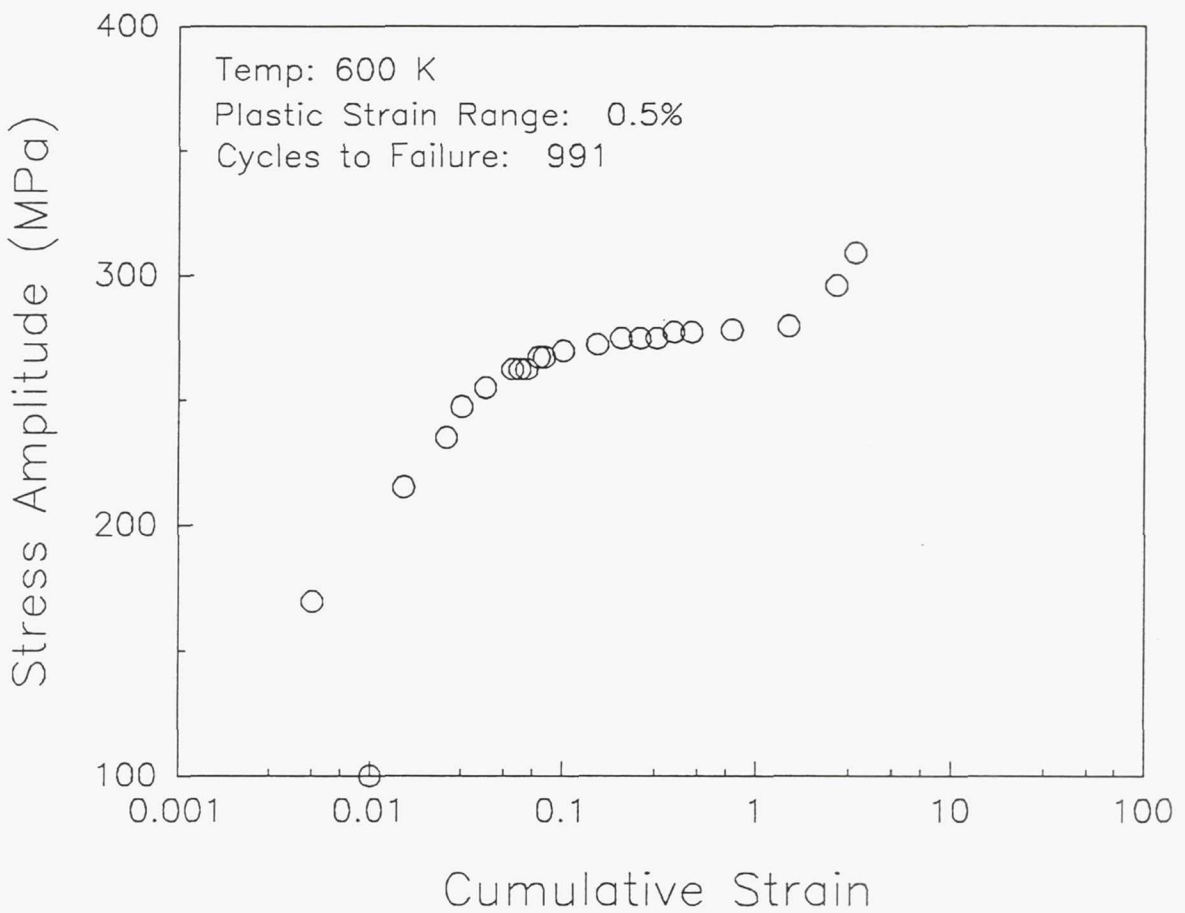
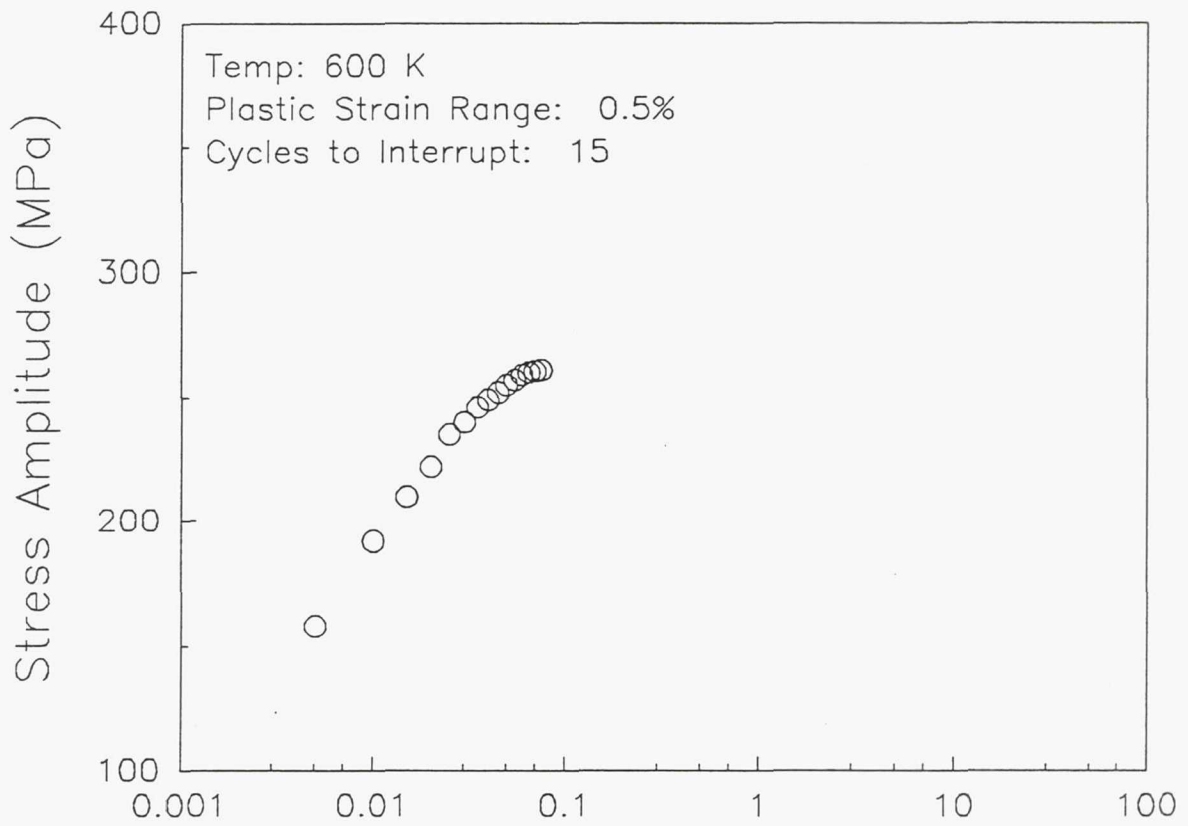
| Strain Range | Tests Stopped At | # Of Cycles | Failure Mode | Sample ID | Temp (K) |
|--------------|------------------|-------------|--------------|-----------|----------|
| 0.01 | beg II | 10 | inclusion | L31 | 600 |
| | beg II | 8 | inclusion | L17 | |
| 0.005 | 1 | 1 | interrupt | L40 | |
| | I | 5 | interrupt | L33 | |
| | beg II | 15 | interrupt | L24 | |
| | III | 991 | inclusion | L15 | |
| | III | 781 | inclusion | L23 | |
| | | | | | |
| 0.01 | III | 390 | inclusion | L25 | 675 |
| 0.005 | II | 26 | inclusion | L27 | |
| | IV | 1517 | interrupt | L28 | |
| | | | | | |
| 0.01 | beg II | 6 | interrupt | L38 | 700 |
| | III | 491 | inclusion | L19 | |
| | IV | 1911 | surface | L18 | |
| 0.005 | beg II | 11 | interrupt | L22 | |
| | IV | 3239 | surface | L9 | |

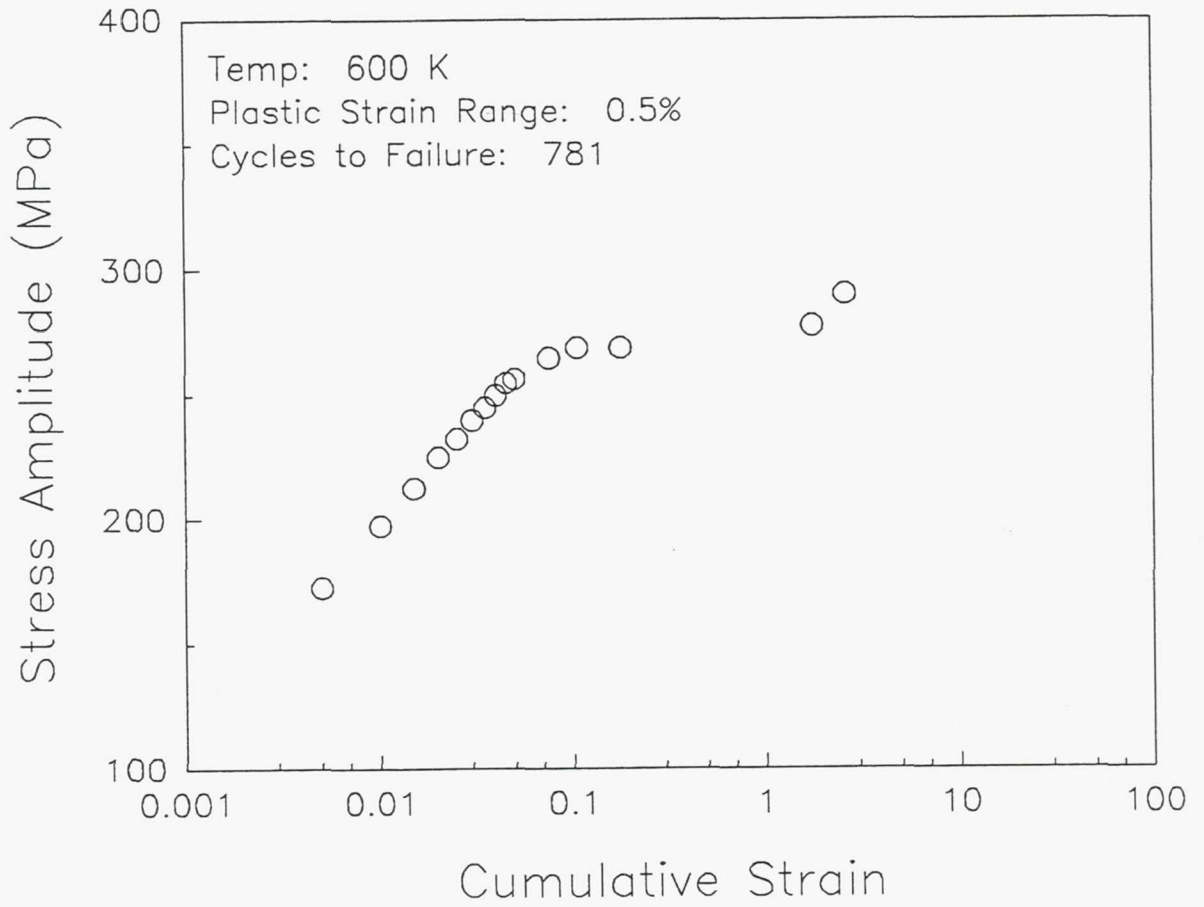
Meaning of notes under *Tests Stopped At*:

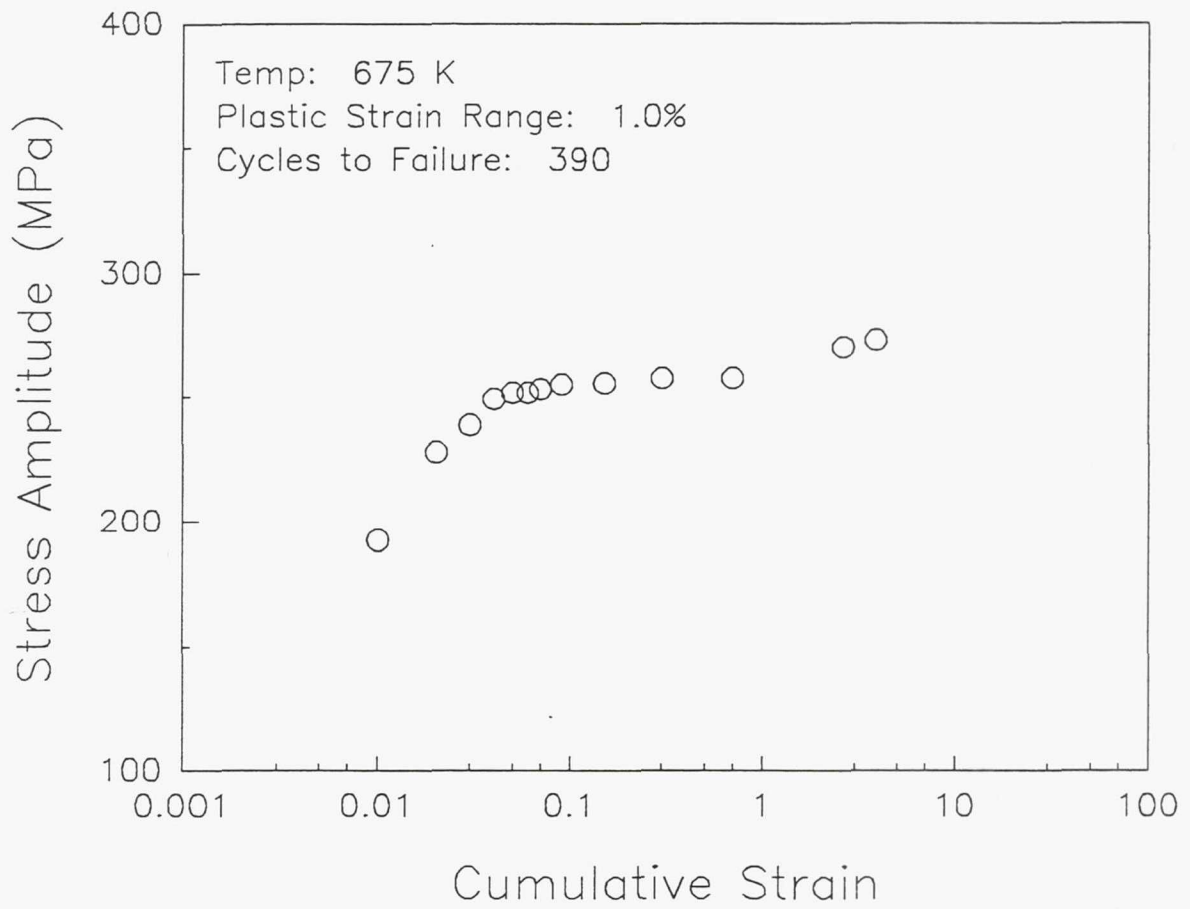
- 1--1 cycle
- I--initial hardening
- beg II--beginning of stable region
- II--region of stable stress
- III--hardening late in life
- IV--stable stress

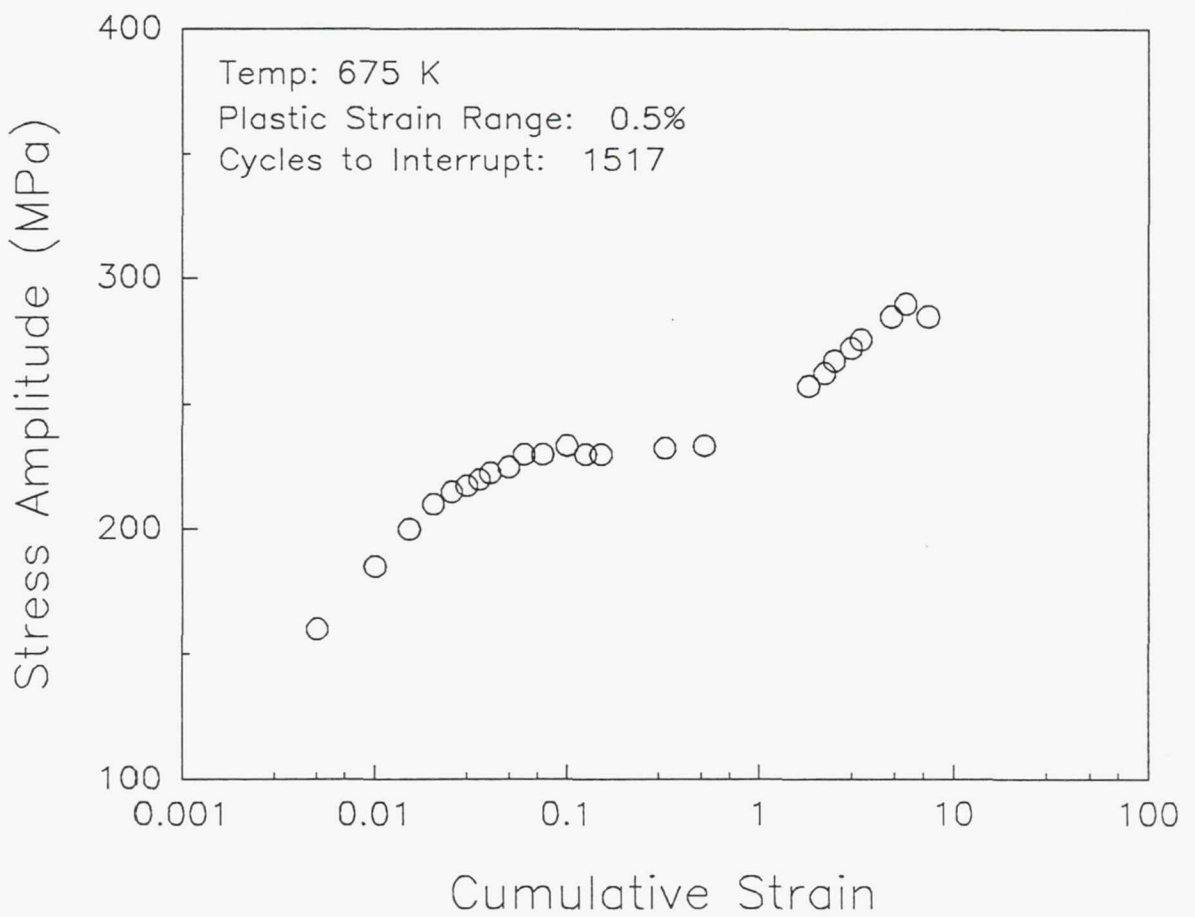
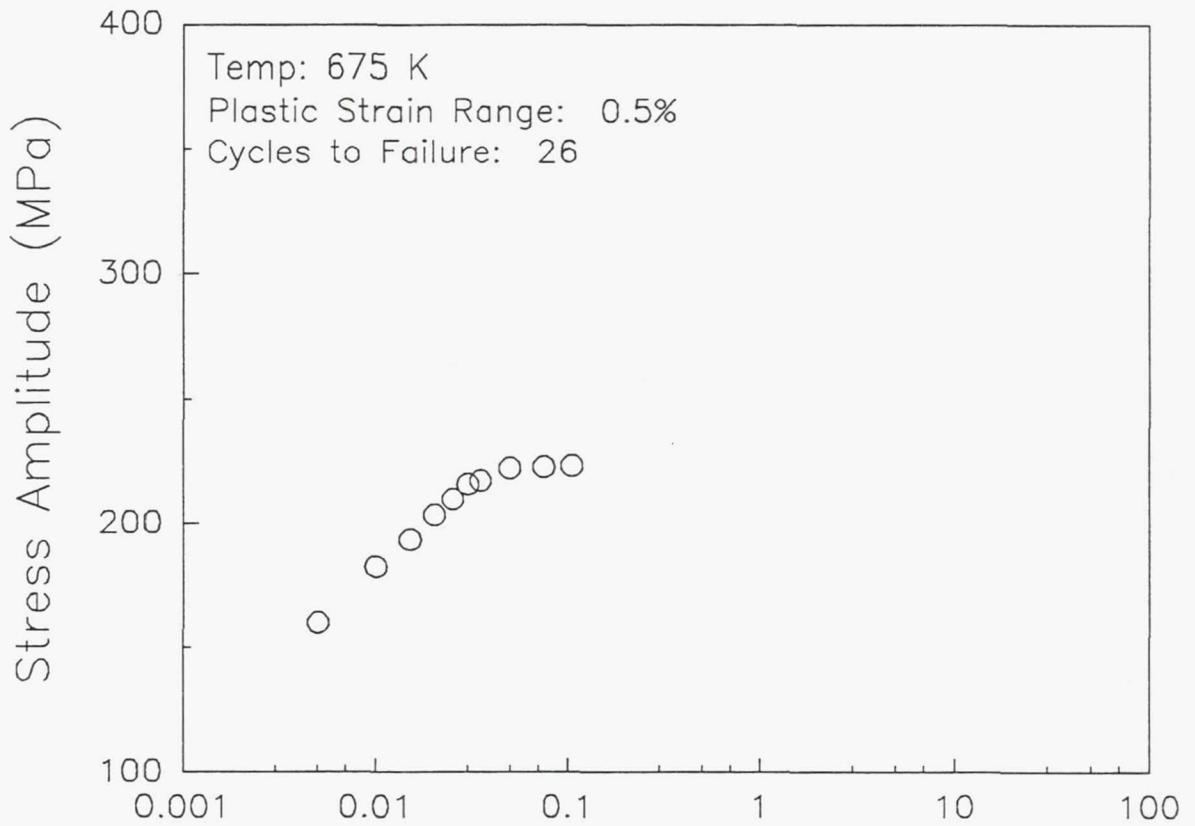


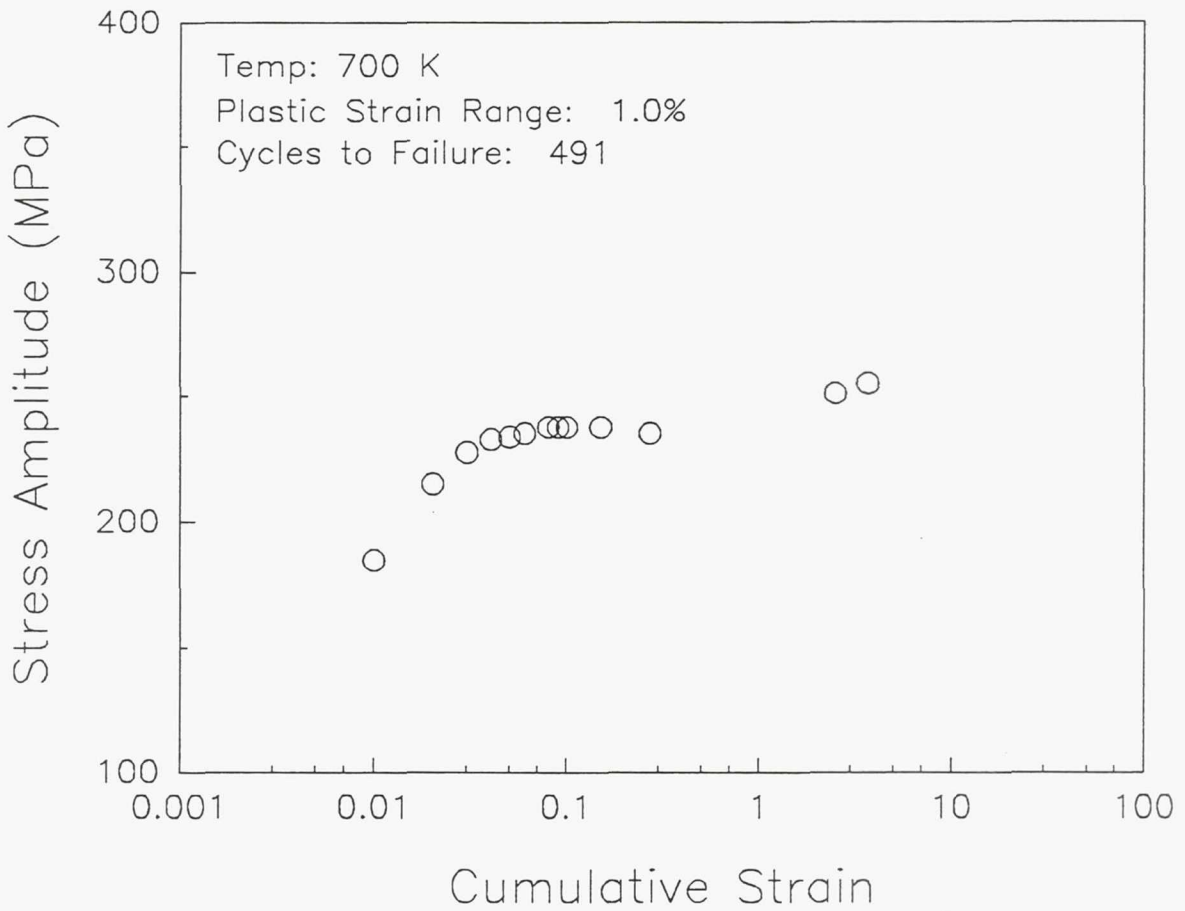
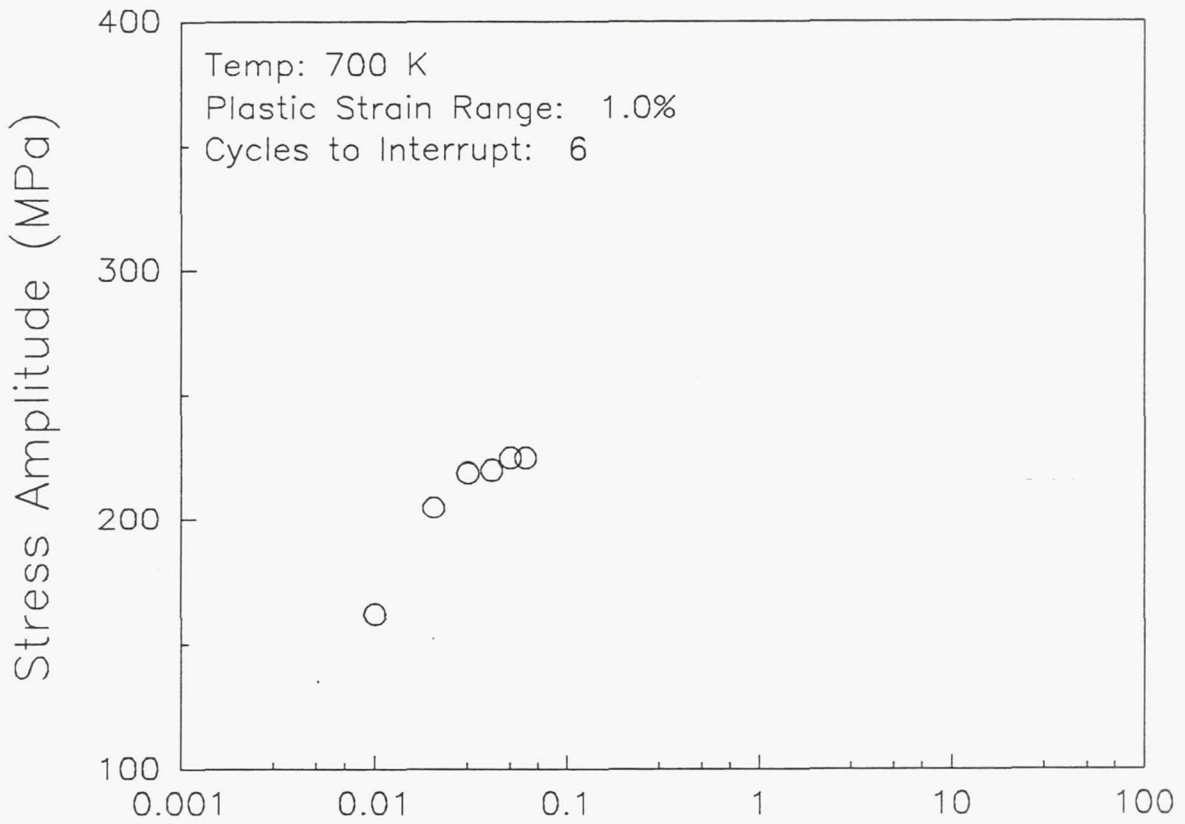


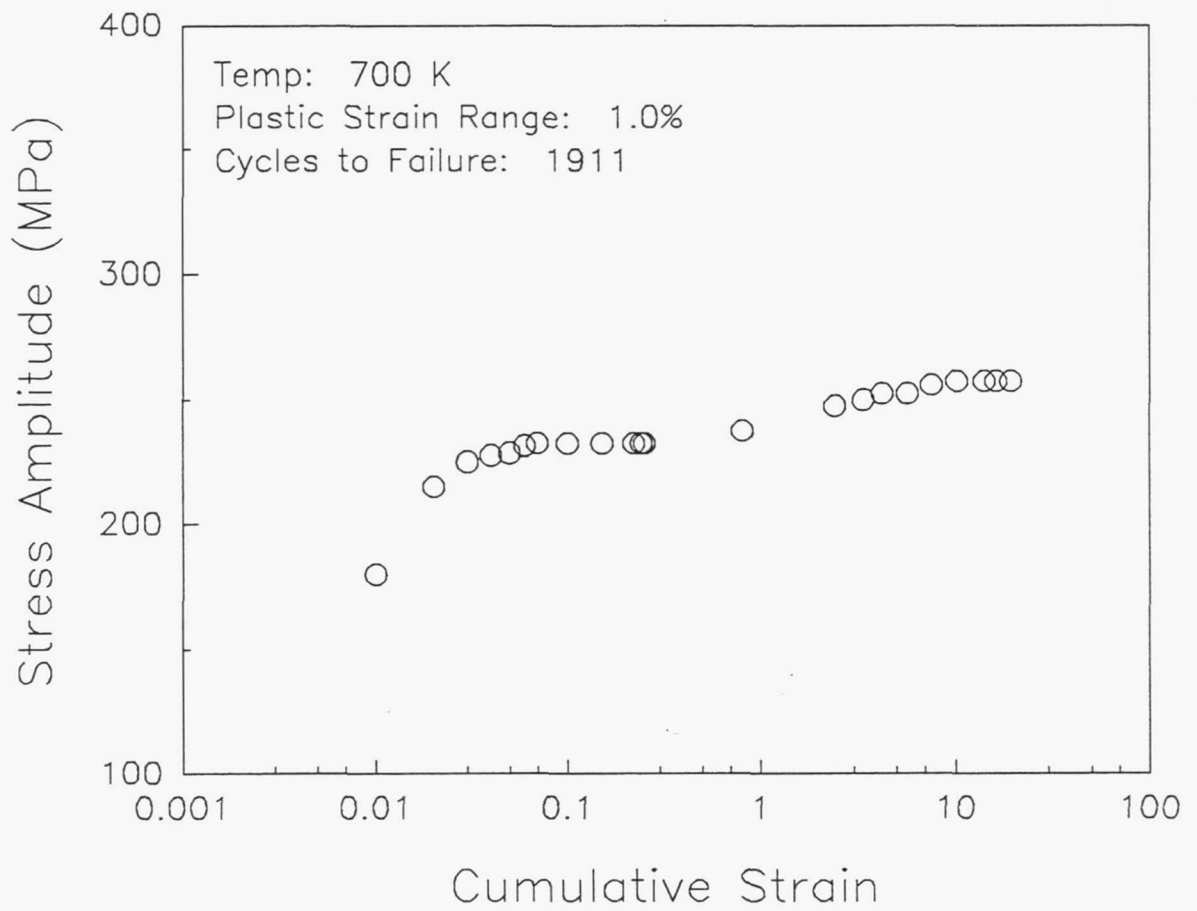


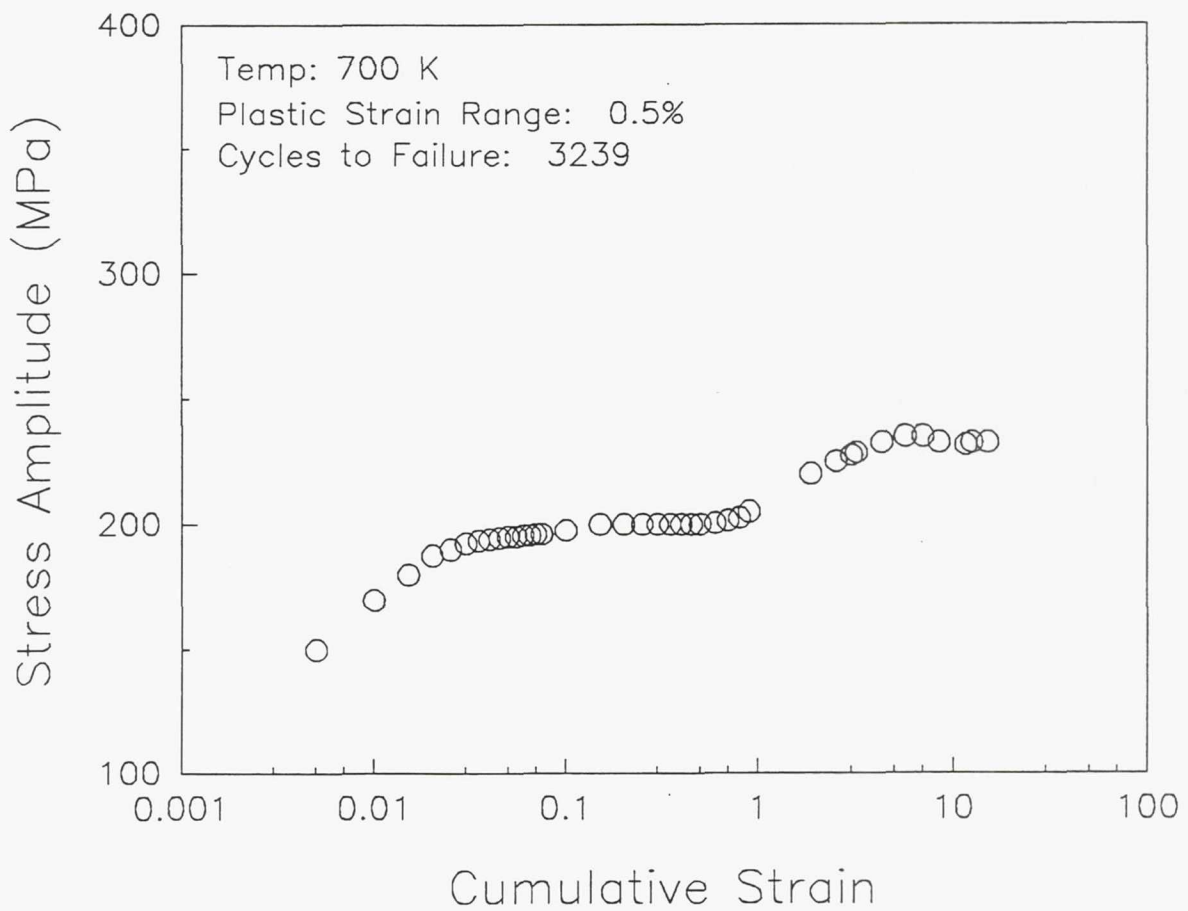
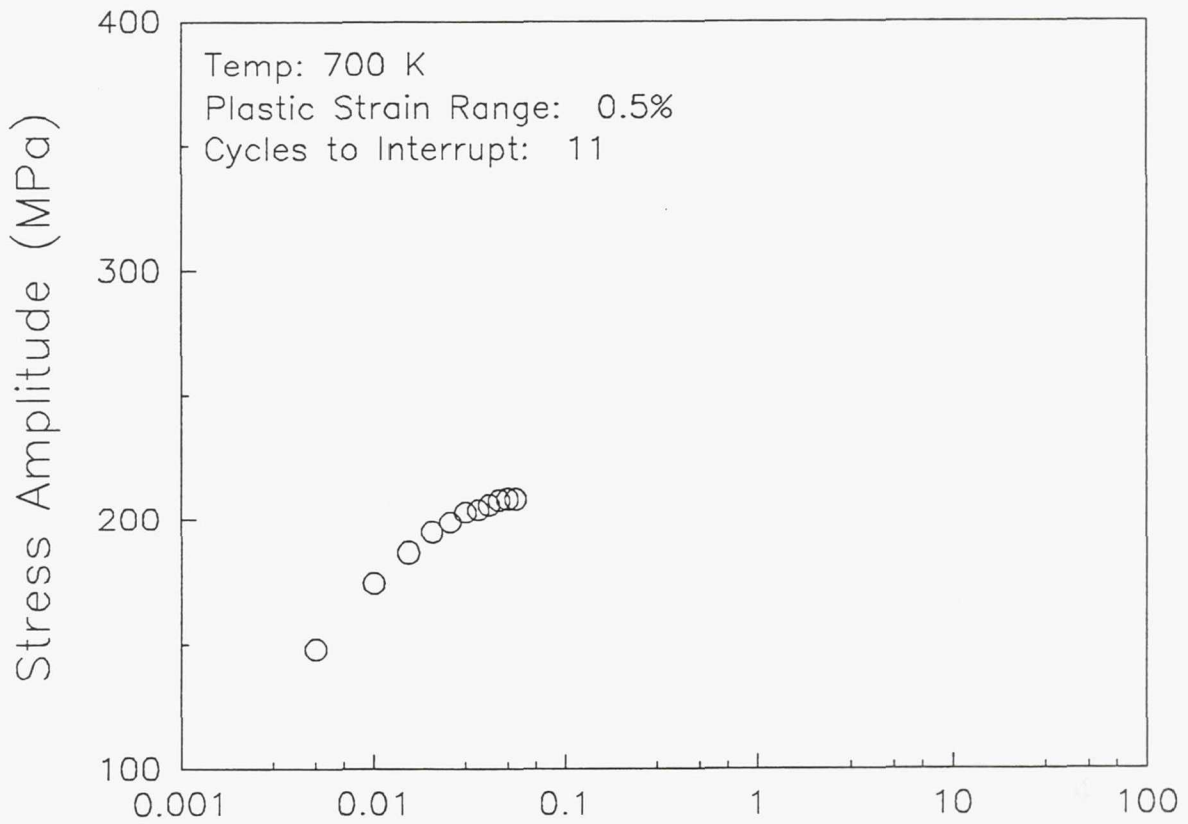












APPENDIX C

ANALYSIS OF DISLOCATION VEIN ORIENTATION

Regions of dislocation veins (or elongated cells) were analyzed to search for a characteristic plane or direction. Each TEM micrograph represents an unique two-dimensional representation of the foil for each \mathbf{g} vector used to illuminate a region. The stereographic projection was used to analyze geometrical relationships between the apparent line direction of the vein and the \mathbf{g} vector or the beam direction. Some of the basic concepts employed include the following principles. Any plane is fully described by the direction of a line normal to the plane; this line is sometimes called a direction-normal. A plane is represented on stereographic projection by a pole which is the direction-normal intersecting the surface of an imaginary globe. The trace of the plane, where it would intersect the stereographic projection, is a great circle 90° from its pole. If two or more planes contain the same line, this line will be the intersection of the planes.

A region from a sample deformed at 675 K, $\Delta\epsilon_p = 0.5\%$ and interrupted after 26 cycles is shown in Figure C-1. The generation of a stereographic projection from a grain within a foil will not be described here. However, a stereographic representation of this grain was obtained for the reference position of 0° tilt (using a single tilt holder). Figures C-2 through C-6 are micrographs taken under two-beam conditions with the \mathbf{g} vectors indicated. The \mathbf{g} vector is the direction-normal of the

planes contributing to the image. This line effectively lies within the plane of the photo-micrograph at an angle that can be determined from the stereographic projection as long as corrections are made for the tilt axis of the crystal and changes in rotation due to the magnification of the microscope. The position of the vein of dislocations is not known because the actual line direction need not be in the plane of the micrograph.

Analysis Assuming Planar Deformation

If the fatigue deformation of NiAl results from planar dislocation movement the veins seen on TEM micrographs represent one cross section of a plane of dislocations. The apparent line direction on the micrograph is a two-dimensional projection of the dislocations and its precise angular relationship with the dislocation plane is unknown. However, an angular relationship can be established between the g vector and the apparent line direction of the vein. A reference plane exists that is normal to the apparent line direction. This reference plane contains the direction-normal of the actual plane of dislocations. Different apparent line directions from various diffracting conditions each define a reference plane. The intersection line between these reference planes is the direction normal to the slip band plane.

Table C-I gives the angular relation between the g vector and the apparent (or projected) line direction for the micrographs in Figures C-2 through C-6. For example in Figure C-2, rotating $g(01\bar{1})$ 88° clockwise (CW) gives the apparent line direction. The apparent line direction for a given micrograph can then be represented as a pole on the stereographic projection. On the stereographic projection, the pole of the vein from Figure C-2 lies on a great circle 88° CW of the

pole $01\bar{1}$. The reference plane mentioned previously is represented by a great circle 90° from the pole. Figure C-7 shows the stereographic projection for the grain in question with dotted traces indicating the reference planes determined from Figures C-2 through C-6. Except for the trace from Figure C-6, there is indication a possible characteristic plane that is not a low index plane.

Analysis Assuming Non-Planar Deformation

If the veins on the TEM micrographs are not the result of dislocations moving a single crystallographic plane, the resulting three-dimensional structure could have a characteristic line direction. The characteristic direction of the veins for any given micrograph must lie in a plane defined by the apparent line direction and the beam direction. Different vein-containing planes may be determined by using various diffraction conditions. The intersection of these planes is the characteristic line direction of the vein.

To determine the actual or characteristic direction associated with the veins in Figure C-1, the data from Table CI is again employed. Because the g and the apparent line direction are in the same plane, a pole representing the apparent line direction is located on a great circle the same number of degrees and in the same sense (clockwise or counter-clockwise) as the angular relation on the micrograph. A pole is also needed which represents the beam direction for the respective two beam conditions. The foil tilt needed to obtain Figure C-3 was $+21^\circ$ (positive tilt was defined as left-to-right rotation about the North-South axis on the stereographic projection). The beam direction used to take the micrograph in Figure C-3, for

example, can be represented by a pole 21° due west of the center. Figure C-8 shows the stereographic projection with traces drawn between the beam directions and the respective apparent-line-direction poles for Figures C-2 through C-6. Ideally the planes would intersect on a line represented by a single point on the stereographic projection. The traces (dotted lines) drawn on Figure C-8 do not intersect at a single point. The area of intersection is, however, fairly small considering the angles can be measured, at best, to $\pm 2^\circ$. The actual direction of the veins appears to be [100].

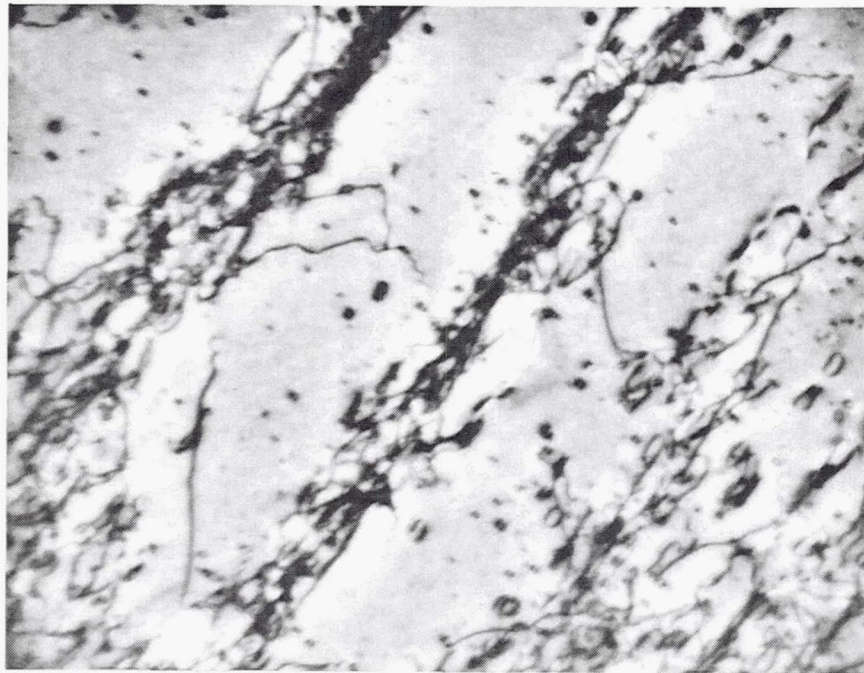
Table CI -- Data From 2-Beam Micrographs

| diffracting condition | angle of g to vein | foil tilt |
|-----------------------|----------------------|-----------|
| $01\bar{1}$ | 88° CW | +2 |
| $\bar{1}10$ | 37° CCW | +21 |
| $10\bar{1}$ | 16° CW | -46 |
| $\bar{1}00$ | 4° CCW | +14 |
| 101 | 50° CCW | -38 |



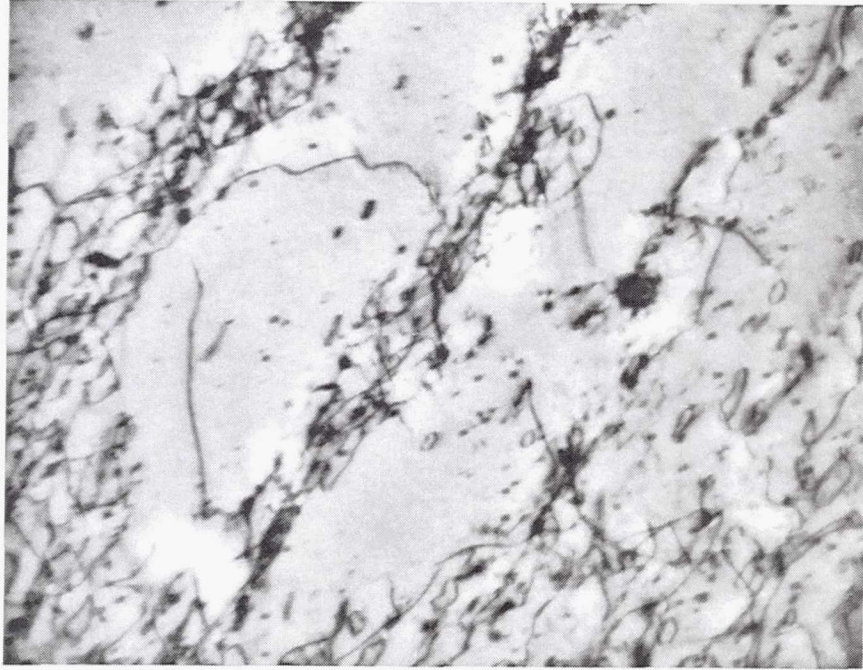
1 μm _____

Figure C-1 Developing veins in sample tested at 675 K $\Delta\epsilon_p = 0.5\%$.

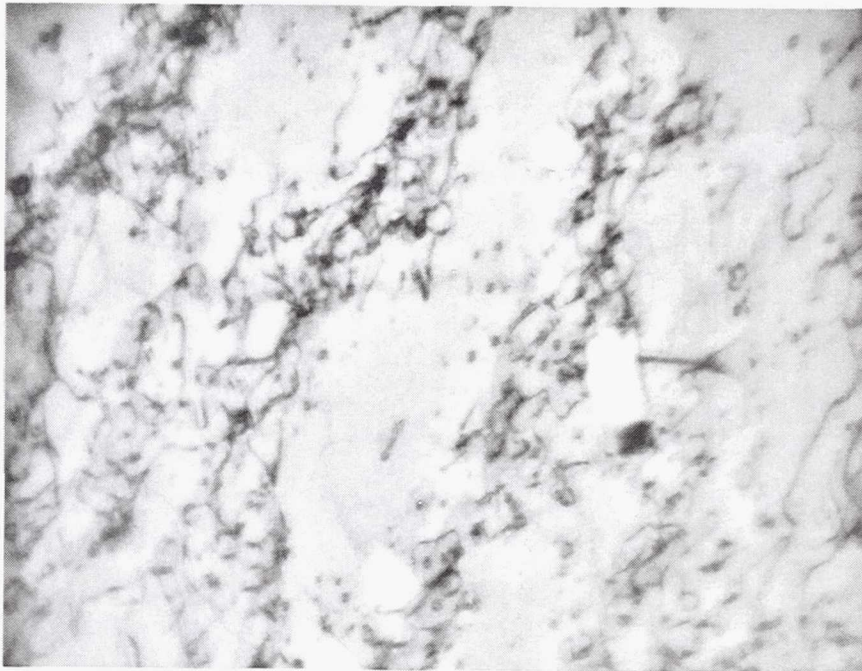


1 μm _____

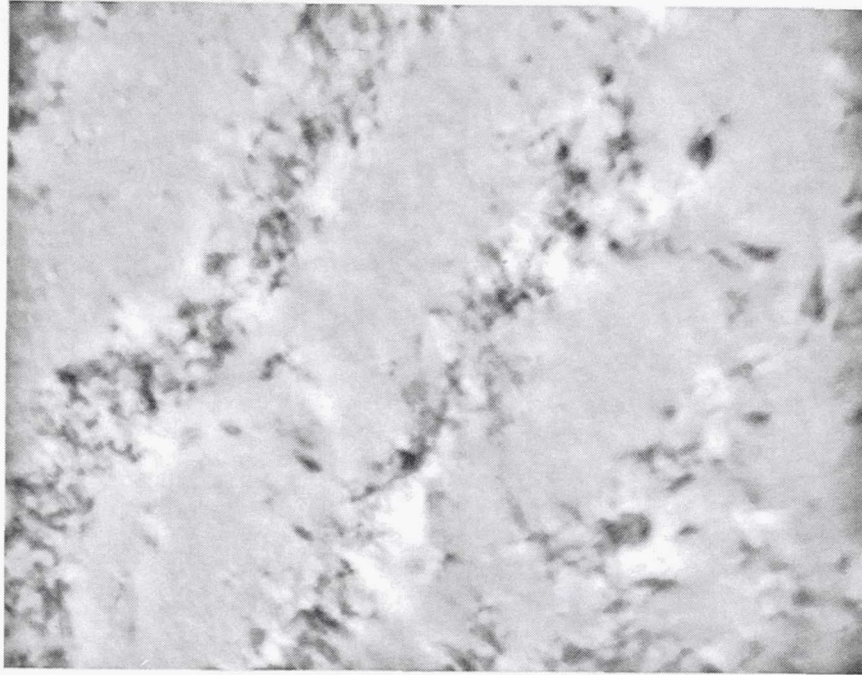
Figure C-2 Same grain micrograph taken with $g = 01\bar{1}$.



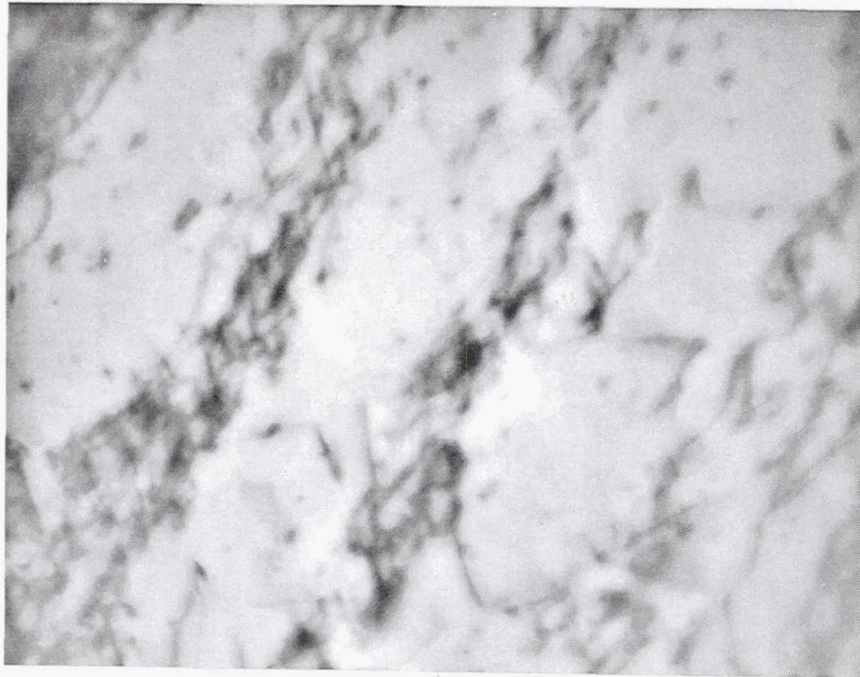
1 μm _____
Figure C-3 Same grain micrograph taken with $\mathbf{g} = \bar{1}10$.



1 μm _____
Figure C-4 Same grain micrograph taken with $\mathbf{g} = 10\bar{1}$.



1 μm _____
Figure C-5 Same grain micrograph taken with $g = \bar{1}00$.



1 μm _____
Figure C-6 Same grain micrograph taken with $g = 101$.

REPORT DOCUMENTATION PAGE

Form Approved
OMB No. 0704-0188

Public reporting burden for this collection of information is estimated to average 1 hour per response, including the time for reviewing instructions, searching existing data sources, gathering and maintaining the data needed, and completing and reviewing the collection of information. Send comments regarding this burden estimate or any other aspect of this collection of information, including suggestions for reducing this burden, to Washington Headquarters Services, Directorate for Information Operations and Reports, 1215 Jefferson Davis Highway, Suite 1204, Arlington, VA 22202-4302, and to the Office of Management and Budget, Paperwork Reduction Project (0704-0188), Washington, DC 20503.

| | | | |
|--|---|---|-----------------------------------|
| 1. AGENCY USE ONLY (Leave blank) | 2. REPORT DATE April 1993 | 3. REPORT TYPE AND DATES COVERED Final Contractor Report | |
| 4. TITLE AND SUBTITLE Deformation Mechanisms of NiAl Cyclicly Deformed Near the Brittle-to-Ductile Transition Temperature | | 5. FUNDING NUMBERS WU-505-63-5A NCC3-295 | |
| 6. AUTHOR(S) Cheryl L. Cullers and Stephen D. Antolovich | | | |
| 7. PERFORMING ORGANIZATION NAME(S) AND ADDRESS(ES) Georgia Institute of Technology Atlanta, Georgia 30332-0245 | | 8. PERFORMING ORGANIZATION REPORT NUMBER E-7745 | |
| 9. SPONSORING/MONITORING AGENCY NAME(S) AND ADDRESS(ES) National Aeronautics and Space Administration Lewis Research Center Cleveland, Ohio 44135-3191 | | 10. SPONSORING/MONITORING AGENCY REPORT NUMBER NASA CR-191121 | |
| 11. SUPPLEMENTARY NOTES Cheryl L. Cullers and Stephen D. Antolovich, Georgia Institute of Technology, Atlanta, Georgia 30332. Project Manager, Michael V. Nathal, Materials Division, NASA Lewis Research Center, (216) 433-9516. | | | |
| 12a. DISTRIBUTION/AVAILABILITY STATEMENT Unclassified - Unlimited Subject Category 26 | | 12b. DISTRIBUTION CODE | |
| 13. ABSTRACT (Maximum 200 words) The intermetallic compound NiAl is one of many advanced materials which is being scrutinized for possible use in high temperature, structural applications. Stoichiometric NiAl has a high melting temperature, excellent oxidation resistance and good thermal conductivity. Past research has concentrated on improving monotonic properties. The encouraging results obtained on binary and microalloyed NiAl over the past ten years have led to the broadening of NiAl experimental programs. The purpose of this research project was to determine the low cycle fatigue properties and dislocation mechanisms of stoichiometric NiAl at temperatures near the monotonic brittle-to-ductile transition. The fatigue properties were found to change only slightly in the temperature range of 600 to 700K; a temperature range over which monotonic ductility and fracture strength increase markedly. The shape of the cyclic hardening curves coincided with the changes observed in the dislocation structures. The evolution of dislocation structures did not appear to change with temperature. | | | |
| 14. SUBJECT TERMS Low cycle fatigue; NiAl; Intermetallic; Dislocation structures; Ductile-to-brittle transition | | 15. NUMBER OF PAGES 98 | 16. PRICE CODE A05 |
| 17. SECURITY CLASSIFICATION OF REPORT Unclassified | 18. SECURITY CLASSIFICATION OF THIS PAGE Unclassified | 19. SECURITY CLASSIFICATION OF ABSTRACT Unclassified | 20. LIMITATION OF ABSTRACT |